5-17-2016 12:00 AM

Particle Entrainment Studies From Dry and Wet Bed

Saber Ayatollahi
The University of Western Ontario

Supervisor
Dr. Cedric Briens
The University of Western Ontario Joint Supervisor
Dr. Franco Berruti
The University of Western Ontario

Graduate Program in Chemical and Biochemical Engineering
A thesis submitted in partial fulfillment of the requirements for the degree in Master of Engineering Science

Recommended Citation

Ayatollahi, Saber, "Particle Entrainment Studies From Dry and Wet Bed" (2016). *Electronic Thesis and Dissertation Repository*. 3771.
https://ir.lib.uwo.ca/etd/3771

Abstract

During the Fluid Coking Process™ bitumen is sprayed into a fluidized bed of hot coke particles. The bitumen undergoes thermal cracking and is converted into gasses, condensable vapors, and solid coke, which deposits on the coke particles. These vapors rise through the vessel and result in entrainment of coke particles. Wet fine coke particles from the freeboard region enter the cyclone and contribute to the fouling of the Coker cyclones which can lead to the premature shut-down of Fluid Cokers.

The primary objective of this research is to determine how bed wetness affects entrainment.

First, a new fluidized bed was constructed, and a novel pseudo-isokinetic sampling was developed and tested to collect entrained solids. Then the entrainment from the dry bed in the bubbling and the turbulent regime was investigated. The cluster analysis was performed and showed an improvement in predicting the flux of solids ejected from bed surface, above the TDH, and across the freeboard.

In the next chapter, the effect of the different levels of bed wetness on flux and size distribution of the entrained particles was studied, and the results were compared to the ones obtained for the dry bed. It was observed that in the bubbling regime, the presence of liquid can change the bubble properties in the bed which will affect the entrainment. However, the effect of low liquid loading on entrainment in turbulent regime was found to be negligible.

In the final chapter, RPT was employed and it was found that the motion of ejected clusters in the freeboard could not be tracked as the clusters move too fast for the strength of radioactive that was used. Moreover, a new model to measure the entrainment of clusters in the freeboard using a modified radioactive tracer technique in which the detectors are collimated was proposed. It was found that this method only provides the decay coefficient of the clusters flux decay.

Keywords

Fluid Coking Process™, Fluidized bed, Fluidization regime, Entrainment, Dry bed, Wet bed, Clusters, Radioactive Particle Tracking, Radioactive tracer technique, Collimation

Co-Authorship Statement

Chapter 3

Article Title: Study of entrainment from a fluidized bed containing dry coke particles
Authors: Saber Ayatollahi, Cedric Briens, Franco Berruti
Status: Unpublished
Contributions: Saber Ayatollahi conducted all experimental work, analyzed the data, and wrote the manuscripts. The work was jointly supervised by Cedric Briens and Franco Berruti, who provided guidance, supervision and reviewed various drafts of the presented work. Jennifer McMillan provided technical advice throughout the project, ensured the work was relevant to Fluid Coking.

Chapter 4

Article Title: Study of entrainment from a fluidized bed containing coke particles in the presence of free moisture
Authors: Saber Ayatollahi, Cedric Briens, Franco Berruti
Status: Unpublished
Contributions: Saber Ayatollahi conducted all experimental work, analyzed the data, and wrote the manuscripts. The work was jointly supervised by Cedric Briens and Franco Berruti, who provided guidance, supervision and reviewed various drafts of the presented work. Jennifer McMillan provided technical advice throughout the project, ensured the work was relevant to Fluid Coking.

Chapter 5

Article Title: Model development for RPT application to entrainment measurements
Authors: Saber Ayatollahi, Cedric Briens, Franco Berruti, Francisco Javier Sanchez Careaga
Status: Unpublished
Contributions: Saber Ayatollahi conducted all experimental work, analyzed the data, and wrote the manuscripts. The work was jointly supervised by Cedric Briens and Franco Berruti, who provided guidance, supervision and reviewed various drafts of the presented work. Jennifer McMillan provided technical advice throughout the project, ensured the work was relevant to Fluid Coking.

Acknowledgments

This is probably the hardest part of the writing a thesis as many people, directly or indirectly, supported me during my journey to the Master's degree.

First and above all, I would like to express my sincere thanks to my both supervisors, Dr. Cedric Louis Briens and Dr. Franco Berruti for giving me the opportunity to do my research at ICFAR. I truly appreciate all the criticisms, constructive feedbacks and guidance, endless support and sharing with me all your invaluable knowledge and expertise with me.

I am grateful and indebted to Dr. Francisco Sanchez, for helping me during my research in several areas through sharing his expertise and knowledge with me, particularly with the "radioactive particle tracking experiments". Also, his technical assistance in the lab is highly appreciated.

I would like to thank to University Machine Service as well as Tom Johnston for helping me in the construction of the experimental unit and his technical assistant.

Also thanks to ICFAR crew and my friends: Mohsen, Uncle Hooman, Ehsan, Majid, Sadra, Stefano Tacchino and Charles Greenhalf who each supported me in a particular way.

Last but not least, I would like to thank my parents as well as my little sister for their patience and encouragement when it was most needed and for allowing me to pursue my dreams far away from them.

Table of Contents

List of Tables

List of Figures

List of Appendices

Chapter 1

1 Introduction and literature review

The research work presented in this thesis investigates the entrainment from a cold model gas-solid fluidized bed. Although this work can be applied to other processes, it focuses on the Fluid Coking™ process specifically. The format used in this thesis is the “integrated article” format.

This chapter provides some information about commercial technologies for upgrading bitumen followed by more details about the Fluid Coking™ process as the emphasis of the present work is placed on entrainment from the Fluid Coker. It will be followed by a section concentrating on the isokinetic and pseudo-isokinetic apparatus as the main technique used in this study to assess the entrainment rate and size distribution of the entrained solids. The next section of this chapter reviews previous studies on entrainment from gas-solid fluidized beds in general as well as the impact of bed wetness on entrainment. Afterwards, a quick introduction to Radioactive Particle Tracking will be presented. Finally, the objectives of this thesis are discussed.

1.1 Introduction

Canada has extensive reserves of heavy oils, including bitumen extracted from oil sands. Worldwide, technically recoverable heavy oil reserves are now larger than conventional oil reserves. In addition, heavy oils constitute a significant component of many conventional types of crude. Heavy oils must be upgraded to more valuable products such as transportation fuels and petrochemical feedstocks (Nikiforuk, 2008; Percy, 2012).

Synthetic crude produced by Fluid Cokers represents about 15 to 20 % of Canada’s combined oil production from conventional sources and oil sands. Fluid Coking™ is also used, around the world, to upgrade heavy oils from various sources. In Fluid Cokers, bitumen or heavy oil is sprayed with atomization steam into a fluidized bed of hot coke particles. The bitumen undergoes thermal cracking, and is converted into gases, condensable vapors and solid coke, which deposits on the coke particles. Since thermal cracking is endothermic, the temperature of the bed particles drops as reaction proceeds and the particles must be circulated to a fluidized bed burner, where part of the coke is burned to reheat the particles that are then conveyed back to the coking reactor. Because the amount of produced coke is much larger than the coke that must be combusted to provide heat for the process, excess coke is removed from the burner.

Although the Fluid Coking™ process produces a large portion of Canada's oil, the operation of a Fluid Coker is not fully understood by the industry as well as several unresolved problems. One of the major problems in Fluid Cokers is the fouling of the Coker cyclones. The entrainment of fine particles in the Coker freeboard can be affected by changes in Coker hydrodynamics such as using baffles or relocating attrition nozzles. The changes in hydrodynamics inside the vessel affect the distribution of gas bubbles across the bed cross-section and, therefore, the flux of the particles ejected from the bed surface (Baron et al., 1988a). The flux of particles ejected from the bed surface can, in turn, affect the flux of fines entrained above the Transport Disengaging Height (TDH) (Briens et al., 1988). Because the coke particles belong to Geldart's group B (they are near the A-B boundary), the change in bed hydrodynamics will change the size of the bubbles exploding at the bed surface and, hence, the TDH and the ejection of wet agglomerates into the freeboard (Baron et al., 1988b). Entrained particles contribute to the fouling of the Coker cyclones, which can lead to the premature shut-down of Fluid Cokers. However, the entrainment from the Fluid Cokers has not been studied extensively and it is, thus, essential to perform more studies in this area.

1.2 The Fluid Coking™ Process

With the quality of crude oil diminishing all around the world, the lowest quality crude oils rich in sulfur, metals and fractions that boil above 560°C are becoming more important to the petrochemical industry (Chastko, 2004; Huc, 2010). Generally speaking, these types of oils are considered as heavy oils and characterized by high carbon to hydrogen ratios and have API lower than 20 down to 10 for extra heavy oils and bitumen (Speight, 2014). Therefore it is necessary to upgrade this kind of heavy oil to produce distillates that can be processed in conventional refineries. As a result of this, a variety of processes have been designed to upgrade these heavy oil feedstocks to more valuable products. These processes can be divided into two main categories. Cracking the heavy oil using catalysts, which is known as Fluid Catalytic Cracking (FCC) process, and incorporates the use of a fluidized bed. This process is mainly used to upgrade gas oil, which includes fractions of high boiling petroleum, into lighter and more valuable produces such as gasoline and diesel (Patel et al., 2013; Sadeghbeigi, 2012). The cracking is achieved through zeolite catalysts which the surface area is maximized to allow more active sites. The endothermic reaction takes place by vaporizing the oil on the active sites of the hot zeolite. More details of this process can be found elsewhere (Sadeghbeigi, 2012; Speight, 2014).

The other process category to convert heavy oil to lighter oil is achieved by thermal cracking which is known as Coking. Coking process itself is divided into four main sub-categories (Speight, 2014): Visbreaking, Delayed Coking, Fluid Coking™ and Flexicoking™.

One of the most advanced upgrading processes is Fluid Coking™. Heavy oil is sprayed into a fluidized bed of hot coke particles where long hydrocarbon chains are thermally cracked into more valuable fragments, which form a synthetic crude oil that can then be processed in regular refineries. ExxonMobil uses Fluid Coking™ in many of its refineries. Fluid Cokers are used by Imperial Oil in its Sarnia refinery and by Syncrude Canada in its Fort McMurray upgrading plant. Between 15 and 20% of Canada’s crude oil production is processed in Fluid Cokers (Natural Resources Canada, 2015).

A Fluid Coker is a circulating fluidized bed of coke particles acting as the heat carrier for thermal cracking of heavy hydrocarbon compounds. By looking at the simplified diagram of a Fluid Coker sketched in Figure 1-1, it can be seen that the Coker consist of two main vessels which are interconnected to each other: The main vessel in which the reaction and recovery of the products occurs in the right unit and the burner (furnace) which provides heat for the endothermic thermal cracking reaction in the left unit. The reactor vessel can be divided into three main sections: reaction, stripper and scrubber.

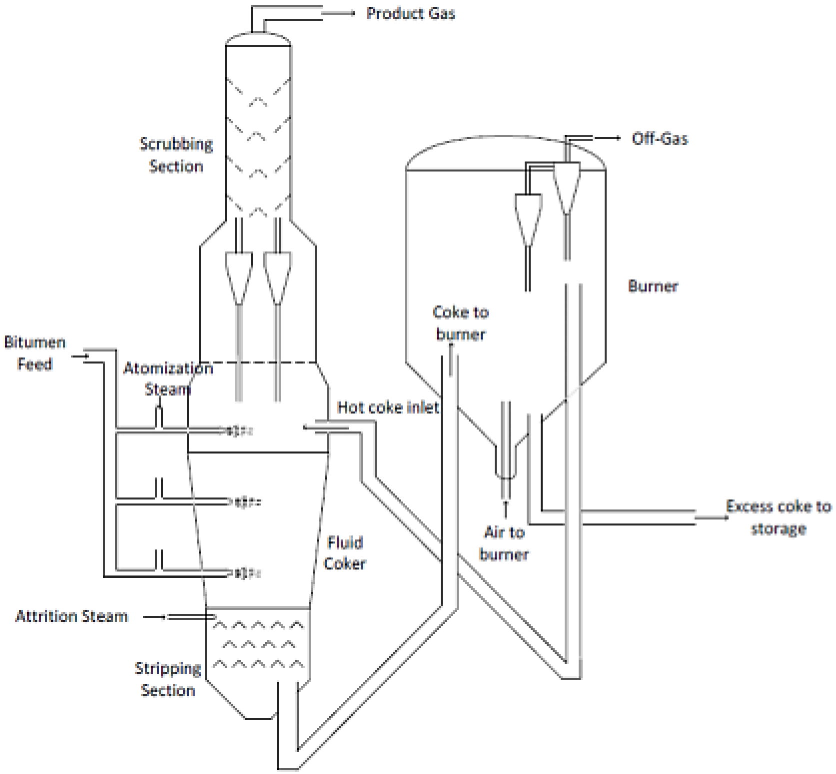

Figure 1-1. Simplified process flow diagram of a Fluid Coker™ reactor (adapted from Prociw, 2014)

Reactor

The reactor is a fluidized bed of coke particles located in the middle of the main vessel and operates at temperatures of 500 to 550 °C and pressures of 34.5 to 103.4 kPa. It is necessary to maintain the bed temperature in this range to achieve thermal cracking. If the temperature exceeds this range, over-cracking to low-value gasses occurs.

The heavy feed is preheated to 350 °C and is injected to this section through the steam atomization spray nozzles. These nozzles inject bitumen and steam into the bed and are arranged along the circumference of the vessel and staggered vertically. Also, fresh hot coke from the burner enters in the top of this section (House et al., 2004; Pfeiffer et al., 1959).

When bitumen contacts the coke particles it is thermally cracked into smaller more volatile compounds, which are further refined downstream, and heavier compounds which form solid coke.

Stripper

The stripper is located at the bottom of the main vessel and is the zone to displace the hydrocarbons in the interstitial voids between the coke particles through countercurrent contact with steam, which improves the removal rate of hydrocarbons vapors from the fluidized coke particles. Also in this region, heavier coke particles will accumulate and their size will be reduced by injecting attrition steam at high velocities. In this way, the size of the coke particles in the bed and consequently the rate of thermal cracking reaction is controlled. The stripper section of the Coker is equipped with an array of baffles or "shed decks" that enhance the interaction between the steam and the coke by adding more turbulence in this region (Bi et al., 2008; Blaser et al., 1986; Graf and Janssen, 1985; Luckenbach, 1969; Pfeiffer et al., 1959).

Scrubber

The scrubber is located at the top of the Coker vessel. The purpose of the scrubber is to remove ("scrub") heavy components from the hot rising vapor from the Coker cyclones, by contacting with low temperature falling hydrocarbon liquids. The scrubber section itself consist of three main parts, scrubber pool, sets of sheds in the middle part and the Koch grid at the top (Jankovic, 2005).

Burner (Furnace)

In the furnace, relatively cold coke enters from the bottom of the stripper to this section. One should note that Coking is an endothermic process and the coke particles leave the Fluid Coker at a lower temperature relative to the temperature when they enter the reactor.

In the furnace, partial combustion with air of some of the coke reheats the coke particles before they are re-circulated to the Fluid Coker to provide the heat required for the thermal cracking process. This limits natural gas consumption in the furnace and produces steam and flue gas that can be used in other parts of the plant, making the process sustainable. Excess coke particles are removed, quenched and stockpiled (Pfeiffer et al., 1959).

Process:

Coking is a continuous process and the following sub-processes happen simultaneously in the Coker:

Once the feedstock comes in contact with the downward-flowing bed of hot coke particles, the thermal cracking reaction occurs in the liquid film formed on the surfaces of the hot coke particles to yield smaller and more volatile compounds in the form of oil vapor and gases, and heavier compounds in the form of solid coke are produced. Due to the high viscosity of the bitumen, large agglomerates made of coke and bitumen will appear in the vessel limiting the heat and mass transfer due to lower surface to volume ratio (Darabi et al., 2010; Gray, 2002). The presence of agglomerates results in more coke being produced and less bitumen being cracked making the process less efficient (Darabi et al., 2010; House et al., 2004).

As mentioned earlier, the vapours produced are separated from the coke in the stripper section at the bottom of the vessel through steam injection. These vapours rising through the vessel result in entrainment of coke particles. As a result, a reasonable space between the bed surface and the top of the column has been allocated. This space is known as the disengaging zone, which allows most of the coarser and heavier solids to fall back to the bed. However, the presence of some hot coke particles in this region is beneficial as they would prevent condensation of vapors by maintaining the high temperature in this region. In this zone, the vessel diameter is decreased to satisfy two objectives: i) to increase the velocity of the vapours and the entrained particles, and ii) to decrease the residence time and scour the vessel walls of any adhered coke (Gray, 1994). These finer solids in the disengaging zone do not fall back to the bed. They are collected in the cyclones and are separated from the vapour phase by means of centrifugal forces. These solids are returned to the bed through the diplegs to maintain the particle size distribution in the Fluid Cokers for good fluidization. The solids collected in the cyclones are wet, and they can plug the flow in the dipleg or the cyclone itself.

The vapors that are separated in the cyclones rise through the chimneys and feed to the scrubber at a temperature around 540 °C and a velocity of about 80 m/s. The cyclone products are mainly vapour, but they may contain some liquid and even solid particles of heavy hydrocarbons with boiling temperature of 1000 °C. In this section, the vapour exchanges heat and mass with the down flowing liquid. As a result of this, the main product of the Fluid Coker is collected from the scrubber overhead at 390-400°C, which are mainly vapour products with a boiling range between -250 and 690 °C. This product enters the fractionator to be separated into four fractions: Sour gas, Butane, Naphtha and combined Gas Oil (CGO) (Heavy Gas Oil and Light Gas Oil). These products will be sent for further treatment and blending, and a portion of HGO is recycled to the scrubber section (Gray, 2002; Jankovic, 2005; Pfeiffer et al., 1959). The liquid containing heavy fractions of the vapors, heavy metals and other impurities are collected in the scrubber pool. There, it is mixed with high pressure saturated steam known as “agitating steam” which keeps all the particulates in the liquid suspended. This liquid is pumped out from the pool and is split in two streams, one joins main feed stream and is injected to the Fluid Coker and the other stream is cooled down and will be recycled to the scrubber pool to maintain the temperature below 400°C (Pfeiffer et al., 1959).

1.3 Sampling system

Based upon the working principles, instrumentation for monitoring solid transport can be categorized into mechanical, optical, electrical, acoustical, and nuclear methods (Nguyen et al., 1989; Soo, 1999). Different techniques provide different insight of the variables in the fluidized bed. A measurement of local solids fluxes at least in the upper dilute region of a circulating fluidized bed is possible with a very simple technique namely the suction probe.

In the applications of gas-solids flows, measurement of particle mass and fluxes, particle concentration, gas and particles velocities, and particle size distribution are of high interest.

The local particle mass flux is typically determined using the isokinetic method as the first principle. This method as a means of gathering information on the particulate content of flowing dusty gasses is well known and widely used.

With the particle velocity determined, the isokinetic sampling can also be used to directly measure the concentration of airborne particles. For flows with extremely tiny particles, such as aerosols, the particle velocity can be approximated to be the same as the local flow velocity. Otherwise, the particle velocity needs to be measured independently due to the slip effect between the two phases. The isokinetic sampling principles require that the sampling probe, which is aligned with the flow (isoaxial) extracts airborne particles at the sampling velocity matching the original undisturbed local flow velocity (i.e. before the probe's insertion). When the particles are collected by a filter or an equivalent particle collector, the stabilized particle accumulation rate represents the actual particle mass flowrate (or particle mass flux) (Soo, 1999).

This technique is readily applied to the steady flow of very dilute, homogeneous suspensions of fine particles in ducts where significant gas velocity gradients are absent. Under these conditions, the simple principle of isokinetic sampling can be applied by applying suction to sampling tubes inserted into the gas stream such that the velocity inside the tube matches the local gas stream velocity (Rhodes and Laussmann, 1992). Too high suction velocity would cause the solids flux to be overestimated, and too low a velocity would give an underestimate. In particular, very fine particles which tend to follow the gas flow lines are 'oversampled' when suction velocity is too high and 'undersampled' when the suction velocity is too low (Herb et al., 1992). The design of such a probe and the corresponding experimental set-up are shown in Figure 1-2. The gas-solid suspension is sucked into the 4 mm diameter tube at a velocity which is adjustable.

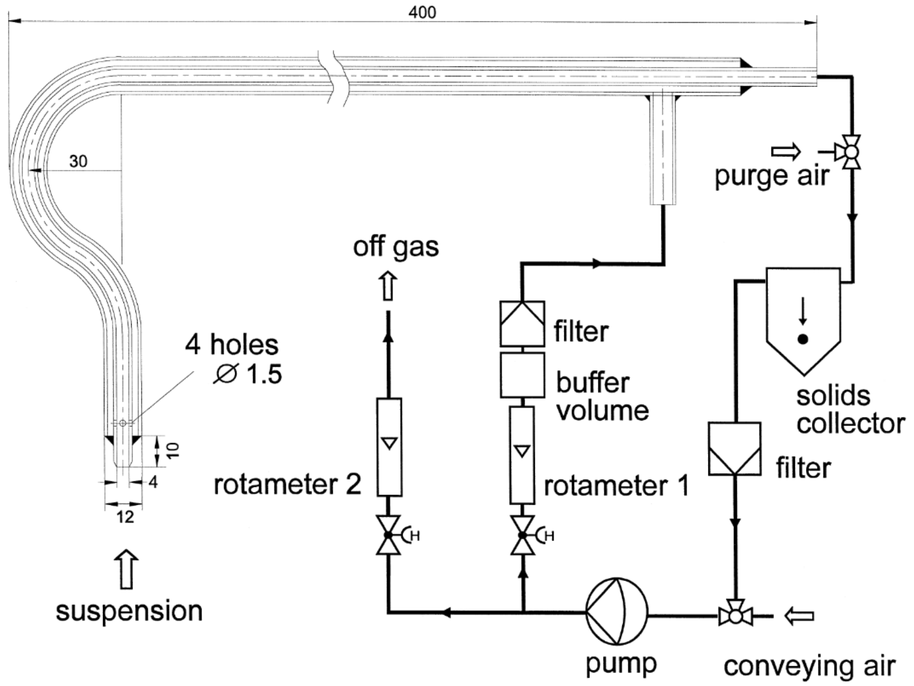

Figure 1-2. Suction probe for measurements under ambient conditions (Adopted from Schoenfelder et al., 1996)

The solids mass which is collected during a predetermined sampling time T_s is simply divided by T_s and by the cross-sectional area of the tube to obtain the local solids flux per unit area. The probe may be rotated to measure either the upward or the downward fluxes.

Even though the true isokinetic sampling occurs when streamlines of both of the gas and the solid particles are not disturbed by the sampling system, this is never achievable in practice, a close approximation occurs when one samples at the local gas velocity using a small sharp edged probe and/or with a thin-wall structure (Davies, 1954; Fuchs, 1975). The difficulties associated with measuring low gas velocities in a particle laden environment led subsequent investigators to simply match the probe superficial velocity with the superficial velocity above the bed. This technique is referred to as pseudo isokinetic sampling. While this technique is appropriate at freeboard positions far from the bed surface, the intermittent nature of bubble eruption leads to greater errors at freeboard positions near the bed surface. It would be virtually impossible to develop a sampling system that measures the rapidly changing local velocity and adjust sampling rate to ensure isokinetic conditions (Hazlett, 1990). In particular, one should note that this condition cannot be fulfilled in the circulating fluidized bed where only the superficial average gas velocity is known. At a given location inside the bed, both the quantity and the direction of gas and solids flows may fluctuate (Werther, 1999). However, studies by a number of authors (Kruse and Werther, 1995; Rhodes and Laussmann, 1992; Zhang et al., 1995) have shown that the influence of the suction velocity on the solids collection rate is fairly small.

As mentioned before, pseudo isokinetic sampling is easier to implement and has been widely in use for measurement of entrainment phenomena above the surface of a fluidized bed (Fournol et al., 1973; Horio et al., 1980; Kim et al., 1997; Pemberton and Davidson, 1986; Yoon et al., 1986). This has been shown to provide accurate results for the measurement of particles entrained from fluidized beds (Hazlett, 1990). Looking at the work by the authors mentioned above, in all of them, the probe is inserted horizontally into the bed, with the probe tip facing down to the bed surface.

Here in this work, pseudo-isokinetic sampling, with a novel design, has been selected for taking samples from the freeboard of the fluidized bed. The details of the design and sampling procedure will be discussed in Chapter 2.

1.4 Entrainment from fluidized beds

In a fluidized bed, entrainment is caused by gas bubbles, which burst at the bed surface and eject solids into the freeboard. The flux of entrained solids decreases exponentially with freeboard height (Baron et al., 1988a; Large et al., 1976; Wen and Chen, 1982). The transport disengaging height (TDH) is the freeboard height above which the entrainment rate does not change appreciably (Baron et al., 1988a). In the freeboard zone, the larger particles tend to fall back to the bed while the smaller ones tend to be carried over with the flowing gas. Thus the average size of the entrained particles decreases with freeboard height up to the TDH point above which the average size remains roughly constant (Chew et al., 2015; Yoon et al., 1986). The entrained solids, especially the fines, are collected and returned to the bed as the lack of fines in the bed can have detrimental effects on the quality of fluidization. For example, it may result in defluidized zones or result in low reaction conversions due to a degradation of particle-gas mass transfer in the bed (Kunii and

Levenspiel, 1991). Cyclones, which are used to recover entrained particles, are typically installed above the TDH, but in some cases, the cyclones may be located below the TDH. To design cyclones and find their best location requires accurate prediction of the flux and size distribution of entrained particles at different heights. The flux of entrained particles and their size distribution depends on flux and size of the particles ejected from the bed surface to the freeboard zone. It should be noted that cyclones may need to be installed below the TDH for economic reasons.

Numerous researchers have tried to predict and model the Transport Disengaging Height (TDH), and more than 25 correlations have been developed since 1958. A recent comprehensive study in this area by Cahyadi et al. (2015) compared the results from all these correlations and found that a poor agreement between the predictions from various correlations. The lack of predictive capability of the available TDH correlations appears to stem from a deficiency in an understanding of the impact of interparticle (e.g., cohesion or clustering effects) and inter-species interactions (e.g., collisional momentum transfer effects). However, the model from Baron et al. (1988) seems to have a stronger fundamental theoretical background as they derived their correlations by performing a force balance on clusters ejected into the freeboard, neglecting the drag force and other inter particle forces for the largest clusters.

In predicting the flux and size distribution of entrained particles above the TDH, several models were developed (Zenz and Weil, 1958; Gugnoni and Zenz, 1980; Briens et al., 1988; Benoni et al., 1994). The common assumption among all of these models is that above the TDH, the column operates as a vertical pneumatic line. These models will be discussed in detail in Chapter 3.

Solids concentration/flux below the TDH was also an important subject in the entrainment area. Several researchers have developed correlations and models to predict and measure the solids concentration as a function of freeboard height as well as measuring the flux of solids ejected at the bed surface to the freeboard. Large et al. (1976), Kunii and Levenspiel (1977) and Wen and Chen (1982) proposed a relatively similar equation which suggests that the flux of entrained solids decreases exponentially with freeboard height:

$$F = F_{\infty} + F_0 \exp(-Az) \qquad \textbf{1-1}$$

Where, F is the entrainment rate of particles in the freeboard at a height, z, above the bed surface, and F_{∞}, is the entrainment rate above the TDH.

Baron et al. (1988b) modified the model by Large et al. (1976) through some assumptions. They confirmed the presence of clusters and the exponential decay of the clusters flux with height up to the TDH where the clusters flux become nil. Based on their observation, they assumed that most of the ejected particles to the freeboard are clusters, not individual particles, and they could predict the total flux at different heights more accurately.

Although it is known that particles ejected into the freeboard are due to bubbles erupting at the surface, the origin of ejected particles remains unclarified and different schools of thought exist on whether particle ejection stems from the bubble nose or bubble wake (Chew et al., 2015). It was observed in the slugging bed that the particles are lifted up by the slug and splashed into the freeboard when it breaks the surface. However, the particles in the bubbling bed are lifted up by the bubbles. When the bubbles burst at the surface, the upward-moving momentum of the particles will carry them into the freeboard (Wen and Chen, 1982).

Some correlations have been proposed for predicting the flux of solids from the bed surface, for example, the correlations by Wen and Chen (1982), Pemberton and Davidson (1986), Chen and Saxena (1978), Saxena and Mathur (1984), Briens et al. (1988). Most of these correlations include assumptions, and their application may not be applicable to all ranges.

Measuring the flux of solids ejected to the freeboard has been extensively investigated. However, entrainment rate at the bed surface is not easy to measure and fluctuates significantly even under a specific operating condition. An indirect solution to obtain the ejected solids flux at the bed surafce is to extrapolate the measured values of F(z) to the bed surface level. For example, Equation 1-1 can be used to smooth the experimental data and obtain F_0 by extrapolation to the bed surface level. The best technique in this area comes from Baron et al. (1988b) which uses both total and cluster fluxes. They used the fact that practically all particles ejected from the bed surface belong to the clusters. This technique uses both the measured vertical profile of the flux of ejected particles and the size distribution of these particles.

As mentioned earlier, during the coking process, the wet agglomerates are ejected to the freeboard. The flux of these particles can affect the flux of fines entrained above the Transport Disengaging Height (TDH). The entrainment of fine particles in the Coker freeboard contributes to the fouling of the Coker cyclones which can lead to the premature shut-down of Fluid Cokers. It is believed that fouling is greatly accelerated when wet particles enter the cyclones. However, the entrainment from a fluidized bed containing relatively low to high liquid loading has not been well studied. McDougall et al. (2004) measured the entrainment from a bed of coke particles in a bubbling regime for various liquid (1-propanol) loadings. They observed that the total flux of entrained particles decreased with increasing liquid content up to a point. They attributed this reduction to the decrease in the amount of free fine particles resulting from the adhesion of fine particles to other fine particles and larger particles in wet beds. This was observed for bed wetnesses below about 1 wt %. When the wetness was increased beyond the 1 wt %., McDougall et al. (2004) observed an increase in the total flux. They related this to the appearance of larger bubbles as the bed fluidization changed. As bubbles become larger, clusters are projected higher.

The introduction of liquid in a fluidized bed results in the formation of wet agglomerates. A high local concentration of liquid in the fluidized bed may result in particles coated with liquid that stick together, which in turn causes poor fluidization, a condition called "bogging", and, eventually defluidization (Hamidi, 2015; McDougall et al., 2004). Degradation of fluidization quality has been attributed to a variety of fluidized bed phenomena such as particle cohesivity, particle agglomeration, reduced bubbling, an increase in minimum fluidization velocity and channeling (Hamidi, 2015; McLaughlin and Rhodes, 2001).

According to Hamidi (2015), changes in fluidization behavior caused by liquids can be classified into two categories:

1- Adding liquid to Geldart group B particles may result in the ratio of interparticle forces to drag force to increase and may cause a transition to group A and group C behavior that finally can result in bogging or defluidization (Hamidi, 2015; McLaughlin and Rhodes, 2001; Seville and Clift, 1984).

2- The agglomeration of fluidized particles has been proposed as another mechanism that can lead to bogging and defluidization (Bartels et al., 2010; van Ommen, n.d.) In an agglomerating fluidized bed, the increase in effective particle size results in a higher minimum fluidization velocity that in turn degrades the fluidization.

Regarding the change in minimum fluidization velocity, Seville and Clift (1984) noted that very 1ight liquid loading causes a slight reduction in the minimum fluidization velocity, U_{mf}. This was observed for Group A materials by D’Amore et al. (1979) as well. However, they found that at higher liquid loading, the minimum fluidization velocity increases markedly but also show that other phenomena occur. At comparatively light loadings, the bed greatly expands beyond minimum fluidization and bubbling commences at higher velocity; this is the behavior characteristic of Group A. At higher loadings, where the bed lifts as a plug or channeling occurs, the behavior is clearly Group C.

1.5 Computer Aided Radioactive Particle Tracking

Radioactive Particle Tracking known as RPT is a non-intrusive method for tracking a single particle in a vessel or column without disrupting the flow inside the vessel (Shehata et al., 2007). The concept of this technique is not new by its nature, but it has gone through several refinements and improvements. Lin et al. (1985) developed a novel computer aided radioactive particle tracking facility to study solids motion in fluidized beds. They were relatively successful in their objectives and were able to observe a change in the direction of solids motion with an increase in gas velocity. Moslemian et al. (1992) then introduced digital pulse counters, which resulted in faster data sampling. Afterward various scientists contributed to improving different aspects of the RPT method. Also, several applications have been found for this technique.

CARPT is a technique for tracking single radioactive tracer by detecting the intensity distribution of emitted γ-rays. The γ-rays are detected using an array of NaI scintillation detectors strategically placed externally around the controlled volume. (Rados, 2003)

During the CARPT experiment, a single radioactive tracer with physical characteristics that match the material in the bed or vessel is introduced into the controlled volume. The tracer particle represents the solids or liquid in the bed and to ensure proper tracking of the solids it is of high importance to have very similar physical attributes as the materials, in the controlled volume. This tracer particle moves along with the bed materials, and its position is determined by a set of scintillation detectors that monitor the γ-ray emissions from the tracer. The radiation intensity recorded by each detector is a function of the distance of the tracer to the detector. To obtain the position of the tracer from the recorded radiation intensities, an in situ calibration should first be performed, by placing the tracer at various known locations and registering the radiation intensity recorded by each detector. Using the information acquired, a calibration curve is developed for each detector to relate the intensity registered by the detector to the distance between the tracer and the virtual center of the detector surface. The calibration curve is established by curve fitting of the raw data, and the fitted curve can have different shape and order. For example, Degaleesan (1997) fitted the calibration data to a cubic spline while Larachi et al. (1997) fitted the data to a polynomial equation of various orders.

Once the distance of the particle from each detector is evaluated, a weighted regression scheme is used to estimate the particle position at each time. Thereby, in a dynamic experiment, a set of instantaneous positions is obtained that gives the position of the tracer at each sampling time.

1.6 Research objectives

The main objectives of this thesis are:

- Design and construction of a new fluidized bed to study the entrainment of solids specifically.

- Development, construction, and testing the new pseudo-isokinetic sampling systems to collect the entrained solids at different axial and radial positions.

- Investigation of entrainment above and below the TDH from a fluidized bed of coke particles in a range of low to high gas velocity.

- Study of the effect of bed wetness on entrainment for different levels of liquid loadings, and comparing to the results obtained for a dry bed.

- Developing a model to measure the entrainment of clusters which are ejected from fluidized bed using a modified radioactive particle tracking.

1.7 References

Baron, T., Briens, C.L., Bergougnou, M.A., 1988a. Measurement of the Flux of Clusters Ejected from a Fluidized Bed. Powder Technol. 55, 115–125.

Baron, T., Briens, C.L., Bergougnou, M.A., 1988b. Study of the transport disengaging height. Can. J. Chem. Eng. 66, 749–760. doi:10.1002/cjce.5450660508

Bartels, M., Nijenhuis, J., Kapteijn, F., van Ommen, J.R., 2010. Case studies for selective agglomeration detection in fluidized beds: Application of a new screening methodology. Powder Technol. 203, 148–166. doi:10.1016/j.powtec.2010.05.003

Benoni, D., Briens, C.L., Baron, T., Duchesne, E., Knowlton, T.M., 1994. Procedure to determine particle agglomeration in a fluidized bed and its effect on entrainment. Powder Technol. 78, 33–42. doi:10.1016/0032-5910(93)02780-E

Bi, H.T., Grace, J.R., Lim, C.J., Rusnell, D., Bulbuc, D., McKnight, C.A., 2008. Hydrodynamics of the Stripper Section of Fluid Cokers. Can. J. Chem. Eng. 83, 161–168. doi:10.1002/cjce.5450830202

Blaser, D.E., Chang, B.H., Baker, C.L., 1986. Fluid coking with improved stripping. U.S. Patent. 4587010.

Briens, C.L., Baron, T., Bergougnou, M.A., 1988. Prediction of entrainment of particles from fluidized beds. Powder Technol. 54, 183–196.

Cahyadi, A., Neumayer, A.H., Hrenya, C.M., Cocco, R.A., Chew, J.W., 2015. Comparative study of Transport Disengaging Height (TDH) correlations in gas–solid fluidization. Powder Technol. 275, 220–238. doi:10.1016/j.powtec.2015.02.010

Chastko, P.A., 2004. Developing Alberta's oil sands: from Karl Clark to Kyoto. University of Calgary Press; Reprint edition (May 3, 2007).

Chen, T.P., Saxena, S.C., 1978. No Title, in: Davidson, J.F., Keairns, D.L. (Eds.), Fluidization: Proceedings of the Second Engineering Foundation Conference. Cambridge University Press, Cambridge University Press, London, p. 151.

Chew, J.W., Cahyadi, A., Hrenya, C.M., Karri, R., Cocco, R.A., 2015. Review of entrainment correlations in gas-solid fluidization. Chem. Eng. J. 260, 152–171. doi:10.1016/j.cej.2014.08.086

D'Amore, M., Donsì, G., Massimilla, L., 1979. The influence of bed moisture on fluidization characteristics of fine powders. Powder Technol. 23, 253–259. doi:10.1016/0032-5910(79)87015-1

Darabi, P., Pougatch, K., Salcudean, M., Grecov, D., 2010. Agglomeration of Bitumen-Coated Coke Particles in Fluid Cokers. Int. J. Chem. React. Eng. 8. doi:10.2202/1542-6580.2346

Davies, C., 1954. Dust is dangerous. Faber and Faber, London.

Degaleesan, S., 1997. Fluid dynamic measurements and modeling of liquid mixing in bubble columns. PhD Thesis. Washington University, Saint Louis, Missouri, USA.

Fournol, A.B., Bergougnou, M.A., Baker, C.G.J., 1973. Solids entrainment in a large gas fluidized bed. Can. J. Chem. Eng. 51, 401–404. doi:10.1002/cjce.5450510402

Fuchs, N.A., 1975. Sampling of aerosols. Atmos. Environ. 9, 697–707. doi:10.1016/0004-6981(75)90156-0

Graf, H.G., Janssen, H.R., 1985. Process for improving product yields from delayed coking. U.S. Patent. 4518487.

Gray, M.R., 2002. Fundamentals of bitumen coking processes analogous to granulations: A critical review. Can. J. Chem. Eng. 80, 393 – 401.

Gray, R.M., 1994. Upgrading Petroleum Residues and Heavy Oils. CRC Press.

Hamidi, M., 2015. Development and Study of Measurement Methods for Jets and Bogging In a Fluidized Bed. PhD Thesis. Western University. London, Canada.

Hazlett, J.D., 1990. Entrainment From Gas-solid Fluidized Beds (volumes I And II). PhD Thesis. Western University. London, Canada.

Herb, B., Dou, S., Tuzla, K., Chen, J.C., 1992. Solid mass fluxes in circulating fluidized beds. Powder Technol. 70, 197–205. doi:10.1016/0032-5910(92)80054-Z

Horio, M., Taki, A., Hsieh, V.S., Muchi, I., 1980. Elutriation and particle transport through the freeboard of a gas–solid fluidized bed, in: Matsen, J.R.G. and J.M. (Ed.), Fluidization. Plenum Press, pp. 509–518.

House, P.K., Saberian, M., Briens, C.L., Berruti, F., Chan, E., 2004. Injection of a Liquid Spray into a Fluidized Bed: Particle−Liquid Mixing and Impact on Fluid Coker Yields. Ind. Eng. Chem. Res. 43, 5663–5669. doi:10.1021/ie034237q

Huc, A.-Y., 2010. Heavy Crude Oils: From Geology to Upgrading : an Overview. Editions TECHNIP.

Jankovic, J., 2005. Simulation of the Scrubber Section of a Fluid Coker. Master’s Thesis. University of British Columbia. Vancouver, Canada.

Kim, Y.T., Song, B.H., Kim, S.D., 1997. Entrainment of solids in an internally circulating fluidized bed with draft tube. Chem. Eng. J. 66, 105–110. doi:10.1016/S1385-8947(96)03166-X

Kruse, M., Werther, J., 1995. 2D gas and solids flow prediction in circulating fluidized beds based on suction probe and pressure profile measurements. Chem. Eng. Process. Process Intensif. 34, 185–203. doi:10.1016/0255-2701(94)04004-4

Kunii, D., Levenspiel, O., 1991. Fluidization Engineering, Fluidization Engineering. Elsevier. doi:10.1016/B978-0-08-050664-7.50001-9

Kunii, D., Levenspiel, O., 1977. No Title, in: Fluidization Engineering. Kreiger Publishing Co., New York.

Larachi, F., Chaouki, J., Kennedy, G., Dudukovic, M.P., 1997. Non-Invasive Monitoring of Multiphase Flows, Non-Invasive Monitoring of Multiphase Flows. Elsevier. doi:10.1016/B978-044482521-6/50012-7

Large, J.F., Martinie, Y., Bergougnou, M.A., 1976. Interpretive model for entrainment in a large gas-fluidized bed. J. Powders Bulk Solids Technol.

Lin, J.S., Chen, M.M., Chao, B.T., 1985. A novel radioactive particle tracking facility for measurement of solids motion in gas fluidized beds. AIChE J. 31, 465–473. doi:10.1002/aic.690310314

McDougall, S.L., Saberian, M., Briens, C., Berruti, F., Chan, E.W., 2004. Characterization of Fluidization Quality in Fluidized Beds of Wet Particles. Int. J. Chem. React. Eng. 2, A26.

McLaughlin, L.J., Rhodes, M.J., 2001. Prediction of fluidized bed behaviour in the presence of liquid bridges. Powder Technol. 114, 213–223. doi:10.1016/S0032-5910(00)00325-9

Moslemian, D., Devanathan, N., Dudukovic, M.P., 1992. Radioactive particle tracking technique for investigation of phase recirculation and turbulence in multiphase systems. Rev. Sci. Instrum. 63, 4361. doi:10.1063/1.1143736

Natural Resources Canada, 2015. Energy Markets Fact Book 2014 - 2015 112.

Nguyen, T., Nguyen, A., Nieh, S., 1989. An improved isokinetic sampling probe for measuring local gas velocity and particle mass flux of gas—solid suspension flows. Powder Technol. 59, 183–189. doi:10.1016/0032-5910(89)80064-6

Nikiforuk, A., 2008. Tar sands: dirty oil and the future of a continent. Greystone Books/David Suzuki Foundation; 2nd edition (March 15 2010).

Patel, R., Wang, D., Zhu, C., Ho, T.C., 2013. Effect of injection zone cracking on fluid catalytic cracking. AIChE J. 59, 1226–1235. doi:10.1002/aic.13902

Pemberton, S.T., Davidson, J.F., 1986. Elutriation from fluidized beds-I. Particle ejection from the dense phase into the freeboard. Chem. Eng. Sci. 41, 243–251.

Percy, K.E., 2012. Alberta oil sands: energy, industry and the environment. Elsevier; 1st edition.

Pfeiffer, R.W., Borey, D.S., Jahnig, C.E., 1959. Fluid coking of heavy hydrocarbons. U.S. Patent. 2,881,130.

Prociw, N.A., 2014. Effect of Nozzle Geometry on Jet Bed Interaction : Experiments with Commercial Scale Nozzles and Eroded Nozzles. Master's Thesis. Western University. London, Canada.

Rados, N., 2003. Slurry bubble column hydrodynamics. PhD Thesis. Washington University, Saint Louis, Missouri, USA.

Rhodes, M.J., Laussmann, P., 1992. A simple non-isokinetic sampling probe for dense suspensions. Powder Technol. 70, 141–151. doi:10.1016/0032-5910(92)85041-S

Sadeghbeigi, R., 2012. Fluid Catalytic Cracking Handbook: An Expert Guide to the Practical Operation, Design, and Optimization of FCC Units. Elsevier.

Saxena, S.C., Mathur, A., 1984. On the origin of solids projected from the surface of a gas-fluidized bed. Chem. Eng. Sci. 39, 917–918.

Schoenfelder, H., Kruse, M., Werther, J., 1996. Two-dimensional model for circulating fluidized-bed reactors. AIChE J. 42, 1875–1888. doi:10.1002/aic.690420709

Seville, J.P.K., Clift, R., 1984. The effect of thin liquid layers on fluidization characteristics. Powder Technol. 37, 117–129.

Shehata, A.H., Aljohani, M.S., Arabia, S., 2007. A Review of Nuclear Non-Intrusive Visualization Methods in Industry : Computed Tomography and. 4th Middle East NDT Conf. Exhib. Kingdom Bahrain.

Soo, S.L., 1999. Instrumentation for Fluid Particle Flow. Elsevier.

Speight, J.G., 2014. The Chemistry and Technology of Petroleum, Fifth Edition. CRC Press.

Van Ommen, J.R., n.d. Early warning of agglomeration in fluidized beds by attractor comparison. AIChE J. 46, 2183 – 2197.

Wen, C.Y., Chen, L.H., 1982. Fluidized bed freeboard phenomena: Entrainment and elutriation. AIChE J. 28, 117–128. doi:10.1002/aic.690280117

Werther, J., 1999. Measurement techniques in fluidized beds. Powder Technol. 102, 15–36. doi:10.1016/S0032-5910(98)00202-2

Yang, W.-C., 1975. A mathematical definition of choking phenomenon and a mathematical model for predicting choking velocity and choking voidage. AIChE J. 21, 1013–1015. doi:10.1002/aic.690210526

Yoon, Y.S., Kim, S.D., Park, W.H., 1986. Entrainment of coal particles in a gas fluidized bed. Korean J. Chem. Eng. 3, 121–125. doi:10.1007/BF02705023

Zenz, F.A., Weil, N.A., 1958. A theoretical-empirical approach to the mechanism of particle entrainment from fluidized beds. AIChE J. 4, 472–479. doi:10.1002/aic.690040417

Zhang, W., Johnsson, F., Leckner, B., 1995. Fluid-dynamic boundary layers in CFB boilers. Chem. Eng. Sci. 50, 201–210. doi:10.1016/0009-2509(94)00222-D

Chapter 2

2 Experimental setup

2.1 Fluidized bed

The experiments were carried out in a bubbling fluidized bed column made of Plexiglas. Figure 2-1 shows a schematic of the apparatus. To ensure relevant results, fluid coke particles extracted from an industrial Fluid Coker with negligible porosity (Furimsky, 2000) were used as bed material. The fluid coke has a particle density of 1470 kg/m^3 as measured by Mohagheghi Dar Ranji (2014). The size distribution of coke particles (Figure 2-2) was obtained using a Particle Size Analyser (Laser diffraction sensor HELOS/BR, Sympatec Inc.), giving a Sauter Mean Diameter of 135 μm. For all experiments, 12 kg of coke were fluidized by air with near zero percent humidity.

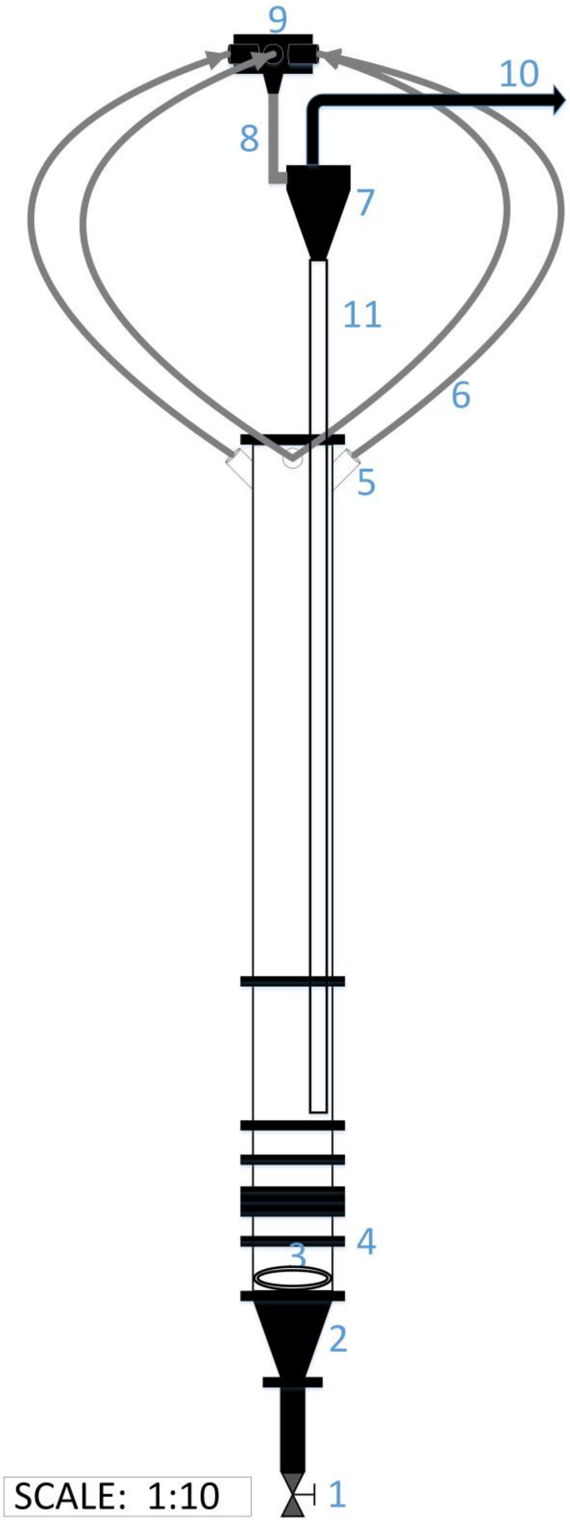

Figure 2-1. Experimental setup components (without the 1.1m high extension): (1) Pinch valve (2) Metallic cone frustum (3) Sparger loop (4) Flange (5) Column exhaust (6) Connection hose to manifold (7) Cyclone (8) Connection hose from manifold to cyclone (9) Manifold (10) Cyclone exhaust (11) Dipleg

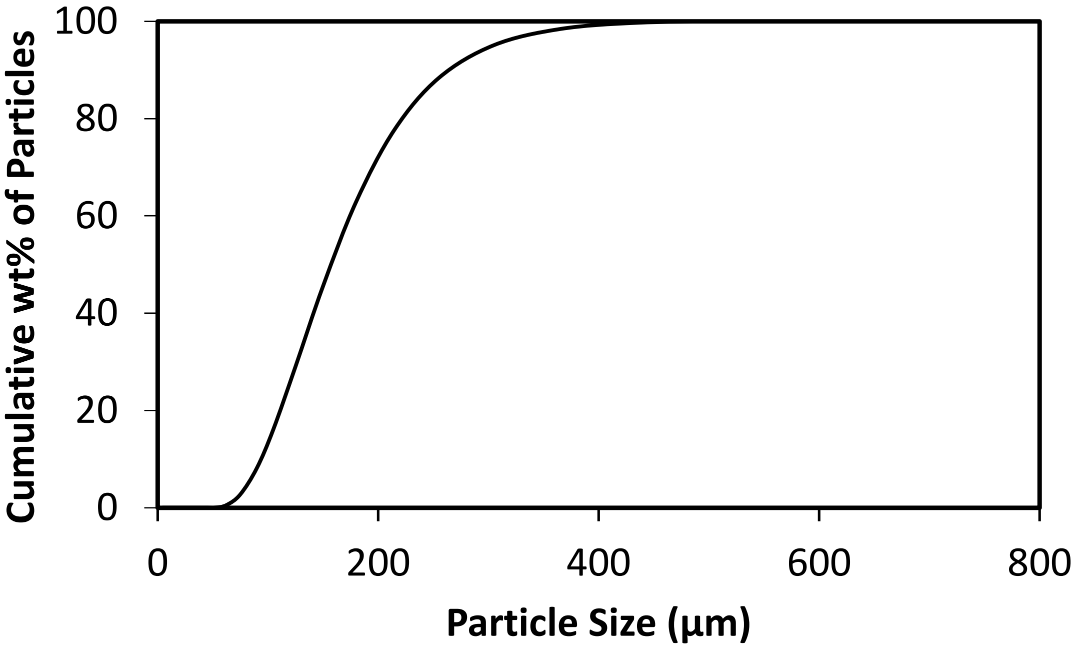

Figure 2-2. Particle size distribution of the coke used

The column was fabricated by University Machines Services and has an internal diameter of 0.1905 m (I.D. = 7.5 in) and an outer diameter of 0.2032 m (O.D = 8 in). In order to facilitate construction, replacement, and modification, the column was built in several sections. The total column height was originally 2.613 m (102.1 in) and for some experiments, the column height was lengthened by installing a 1.10 m extension section with the same I.D. and O.D. as the original column, for a total height of 3.713 m.

Figure 2-3. Left: Pinch valve. Right: Cone frustum section

The very bottom of the fluidized bed column is equipped with a 0.0635 m (2 ½ in) diameter pinch valve to ease the removal of solids and recovery of the radioactive tracer. The pinch valve is connected to the acrylic column by a metallic cone frustum (Figure 2-3). This conical design facilitates solids removal. A sparger located at the top of the conical section, which provides fluidization air to the bed, consists of two loops (one internal and one external) in order to equalize the pressure along the sparger and provide a uniform distribution (Figure 2-4). This sparger has nine 3.175 mm (1/8 in) holes per side (36 holes in total) and was constructed by Sanchez Careaga (2013) based on the distributor design guidelines by Kunii and Levenspiel (1990).

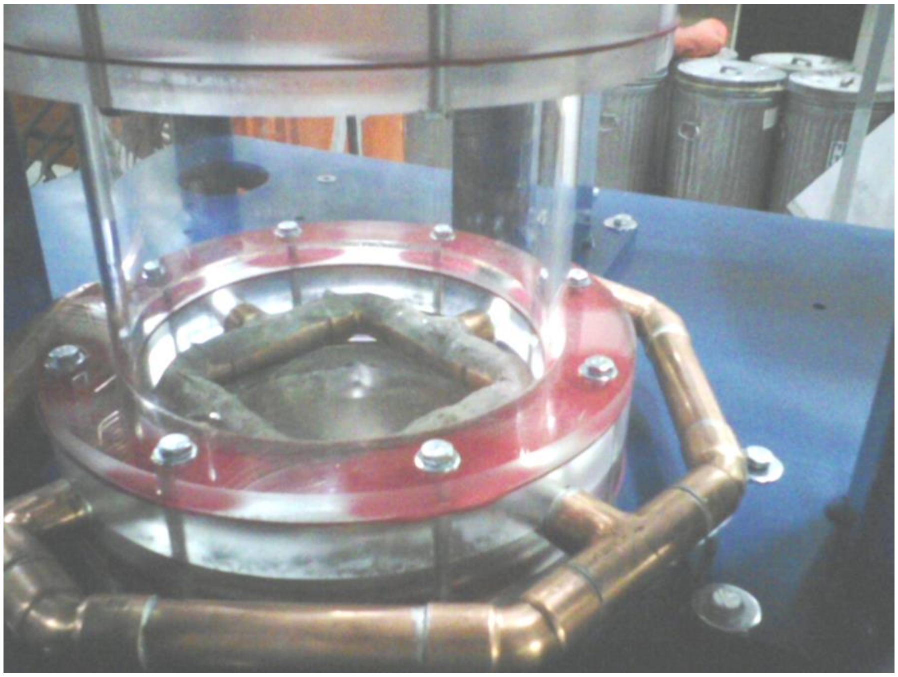

Figure 2-4. Sparger loop air feedstock (Sanchez Careaga, 2013)

Along the fluidized bed, several taps are fitted with pressure snubbers, which are connected to pressure transducers (OMEGA Engineering, INC) whose output are recorded with a computer through a National Instruments USB-6008 DAQ. These pressure measurements along the fluidized bed are used to provide information such as bed height and bed mass. Another tap is equipped with a nipple and a ball valve and is used for taking samples from bed while it is fluidized. The sample taken is the representative of the material for that ongoing experiment.

The column is equipped with two pressure relief valves to ensure that its pressure inside does not exceed ten psig.

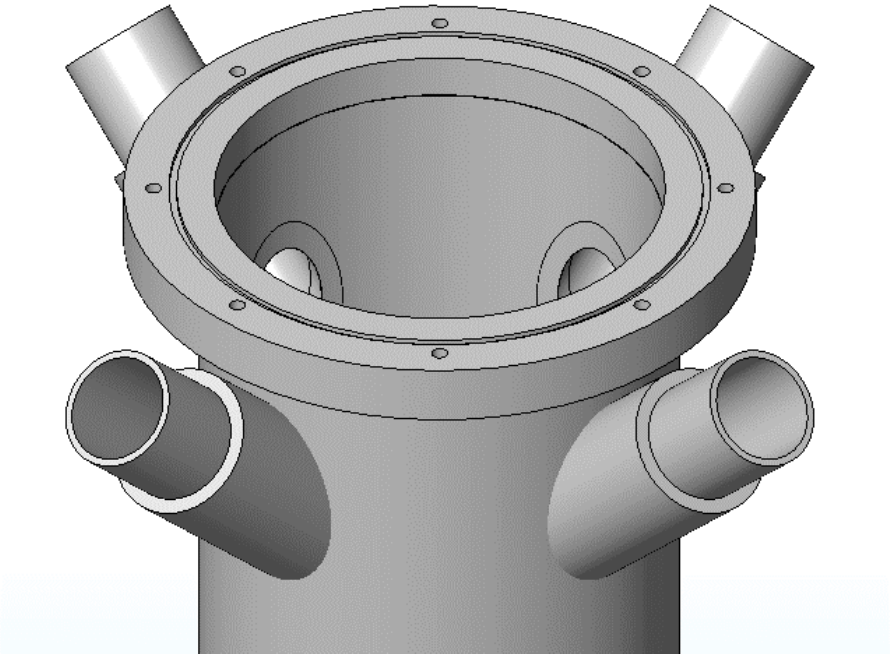

Figure 2-5. Column exhausts

Unlike ordinary fluidized columns for which one exhaust is located in the middle of column lid, four 44.704 mm I.D. (2 in O.D.) exhausts were improvised on every 90 degree around the top of the column. As shown later, this provides space for isokinetic sampling probes and a cyclone dipleg. Exhausts are connected to a manifold by flexible hoses. This manifold is connected to a cyclone, located right above the column on a separate structure. The cyclone returns the collected entrained solids to the bed through a 41.148 mm I.D. Lexan dipleg. A ball valve and a quick connection assembly are placed between the cyclone solids outlet and the dipleg which is used to sample the solids collected by the cyclone. The cyclone exhaust is vented outside of the lab.

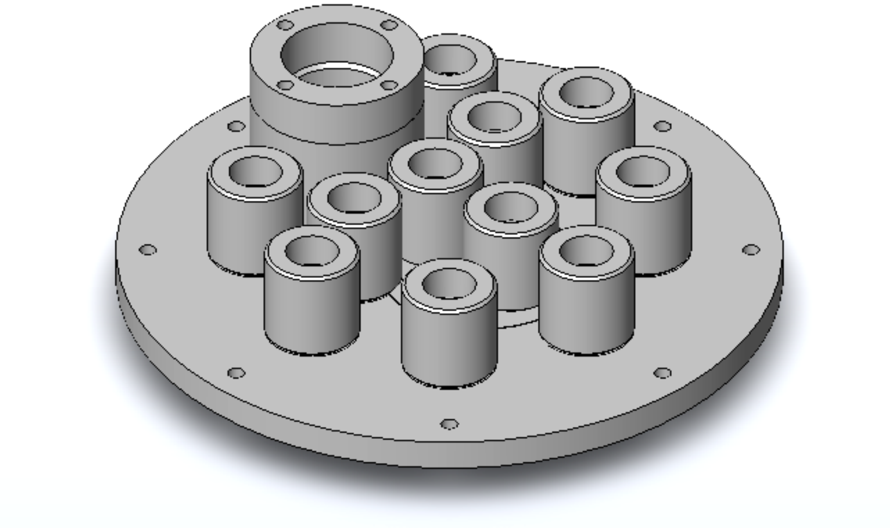

Figure 2-6. View of the column lid: Sampling ports and dipleg inlet.

Figure 2-6 shows the design of the column lid. The lid was designed in a way to allow us to conduct the pseudo-isokinetic sampling measurements from the top: ports have been set up at different radial and angular positions so that none of the probes inserted into these ports interfere with each other. The maximum achievable number of ports was eleven (See Figure A-1 for "to scale" drawing of the dipleg and the sampling ports on the column lid).

Figure 2-7 depicts the main column as well as the supporting structures. The supporting structure on which all the parts are mounted on is made of two sections: Internal and External structure. The internal structure on which the main fluidized bed is attached is made of iron. In the middle of its frame, there is a blue color iron sheet on which six vertical structures (Tracks) for mounting radiation detectors are placed at every 60° around the column. Enclosures which hold the scintillation detectors can slide vertically on the track. The scintillation detectors will be described thoroughly in Chapter 5.

The frame of external structure is made of metallic Unistrut® and has two wooden floors: on the first floor, one can access to the lid of the column as well as the sampling probes in order to justify the height of the probes or to take any required action. This section is accessible through a fixed ladder. The second floor of the structure is also wooden and used for mounting the manifold and cyclone.

Figure 2-7. Internal and external supporting structures. Internal has a blue color, and the external is made of Unistrut®

The compressed air used for fluidizing the materials is supplied by the lab compressors and reaches to the side of the unit at 120 psig. The pressure is dropped to the desired value (not less than 50 psig) using a pressure regulator. After the regulator, there is ball valve which is fixed at 10% opening and is used to mimic the effect of sonic nozzles. In this way, one can make sure that the pressure fluctuation in the downstream does not significantly affect the air flowrate measurements. The air passes through the valve and reaches the sparger through a 50.8 mm diameter copper pipe in which an orifice plate (31.75 mm opening diameter) for measuring the air flowrate is placed. The pressures difference on the sides of the orifice plates (Flange taps) are displayed directly by a digital manometer, and a pressure transducer along with a computer program registers this differential pressure for further analysis. Upstream pressure is registered by the same digital monometer by simply releasing the tube connected to downstream of the orifice plate from the monometer. Using these pressure data, one can calculate the mass flowrate (and gas velocity consequently) of the air using the equation provided by McCabe et al. (1993). The air flowrate can be set by adjusting the pressure upstream of the orifice plate using the aforementioned regulator.

2.2 Pseudo-Isokinetic sampling system

As mentioned in Section 1.3, most published studies have used sampling probes that are inserted into the fluidized bed horizontally, and the tip of the probe could face upward or downward to measure the upflux or downflux respectively. Due to the design limitation with the current fluidized bed, we came up with a novel design and strategy for using the pseudo-isokinetic sampling probe in our column. In our design, the probes are inserted into the column from the ports available on the column lid (See Figure A-1) vertically, and one can easily adjust the vertical location based on the needs. The advantages of this design are: i) the probes can be easily pulled back to the top of the column when performing radioactive tracer measurements, to prevent any interference with the radiation, ii) simultaneous sampling from different radial positions at any particular height from the bed surface was facilitated, and iii) the need for bending the metal tube (See Figure 2-9) and drilling ports across the column was eliminated. One of the disadvantages of this design is that it makes the whole experimental unit tall. Figure 2-8 shows the general scheme of the sampling system.

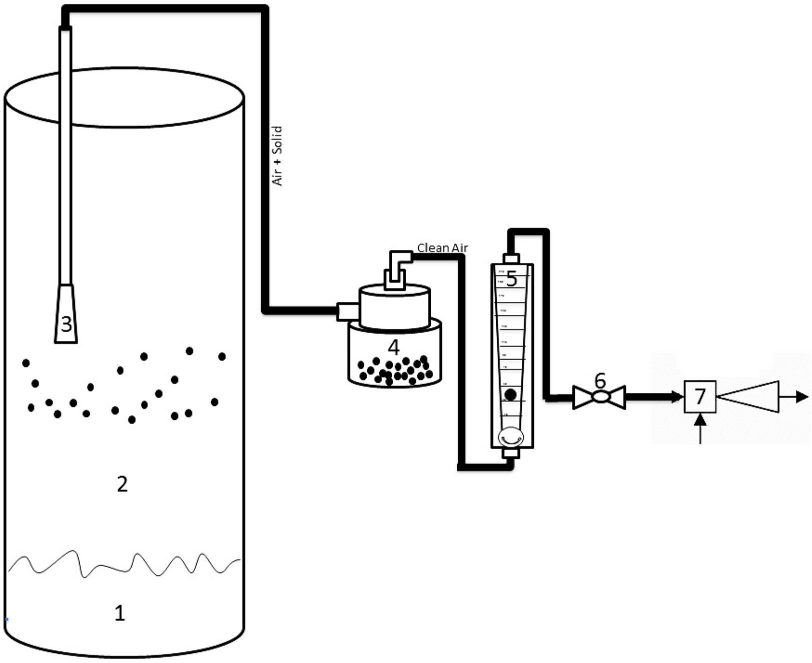

Figure 2-8. Scheme of the sampling system (Drawing not to scale): (1) Dense bed (2) Freeboard (3) Sampling probe (4) Collection vessel (5) Flowmeter (6) Ball valve (7) Ejector

The sampling system consist of the following parts:

1- Sampling probes

2- Collection vessels

3- Flow control and monitoring instruments

4- Ejector(s)

The sampling probe is made of a plastic conical shape tip which is connected to a metal tube. The plastic cone was designed according to recommendations from Hazlett (1990) and has a 30 mm diameter mouth and is tapered down to accelerate the particles with the angle of 11° and reduce the diameter to a size which saltation in the transfer line was not a problem. As a result, the metallic tube connected to the plastic cone has 12.903 mm O.D. (10 mm I.D.). Saltation velocity is important since, in any system with horizontal and vertical lines of the same diameter, the saltation velocity is always greater than the choking velocity - so if we avoid saltation, we avoid choking. The saltation velocity was calculated using correlations proposed by Rizk (1976) and Wirth (1983) to ensure that there was never any risk of saltation in the sampling lines. The probes were constructed in UMS. Figure 2-9 shows the design details of the sampling probe.

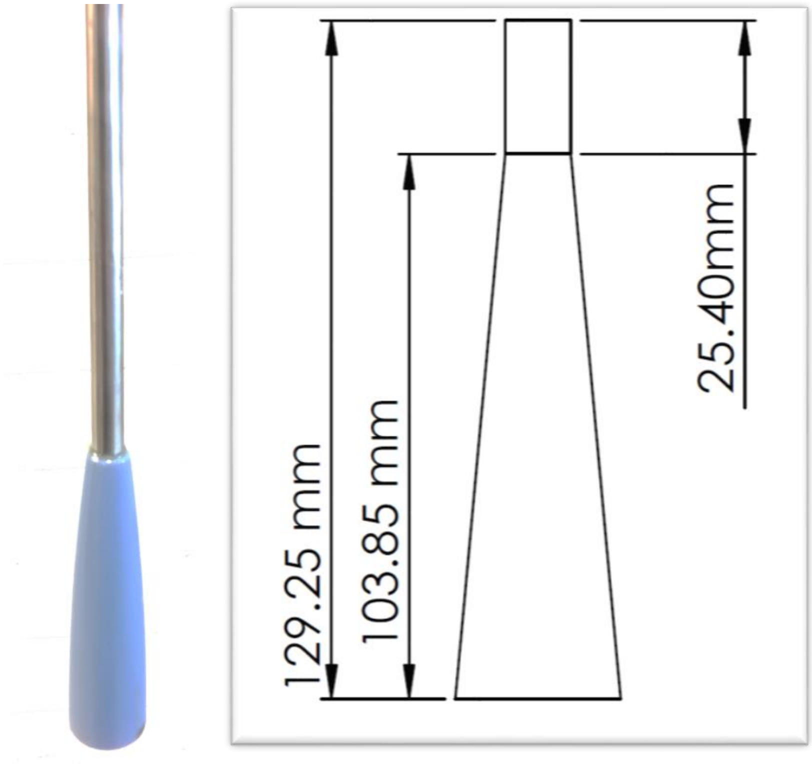

Figure 2-9. Full sampling probe and 11° plastic conical probe tip

The collection vessel consists of a removable jar in which the solids are accumulated and a filter (Whatman® quantitative filter paper, ashless, Grade 41, circles, diam. 47 mm) which stops the particles from being transported to the other sections. The filter has a particle retention of 25 μm. The solids and air enter the horizontal opening of the collection vessel. The top opening is connected to the bottom of a flowmeter in which the clean air passes through.

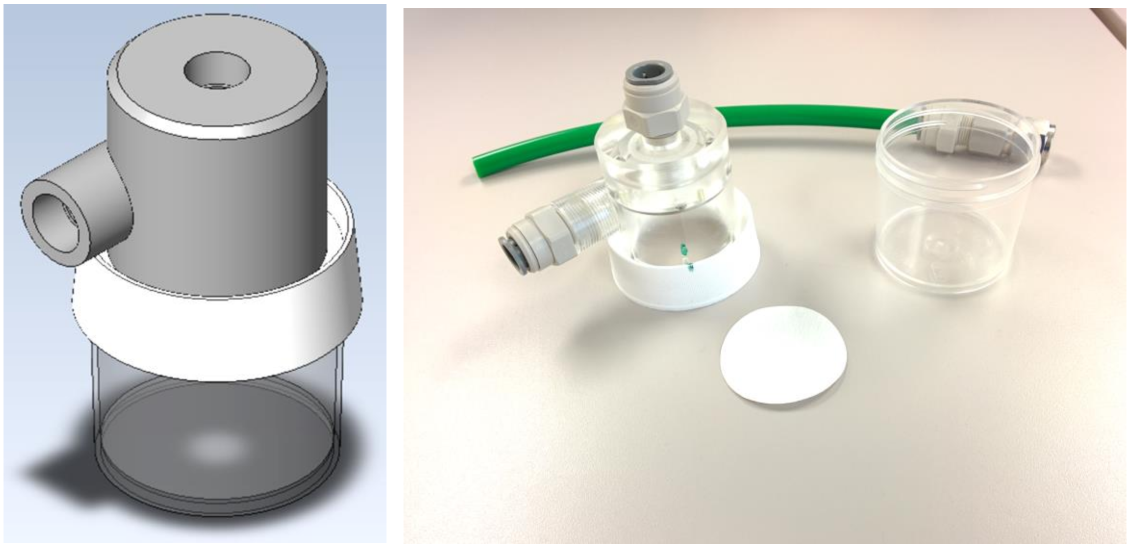

Figure 2-10. Collection vessel

For measuring and controlling air flowrate in each of the sampling lines, flowmeters with a control valve were utilized (Fl-807-V, ±4% full-scale accuracy, OMEGA Engineering, INC.). These flowmeters are located between the sampling vessel and the ejector and are used to adjust the flow to maintain velocity in the probe mouth equal to superficial gas velocity in freeboard. Each flowmeter is equipped with a needle valve for accurate control of the flowrate. The probes are called pseudo-isokinetic as the velocity that is matched is not the true local gas velocity but the cross-sectional average gas velocity, i.e. the superficial gas velocity. This has been shown to provide accurate results for the measurement of particles entrained from fluidized beds (Hazlett, 1990).

Figure 2-11. Flowmeter employed in the experiments (Fl-807-V)

To provide enough suction air at the probe tip to equalize the air velocity at the probe tip to the one in the freeboard, an ejector was utilized. The ejector uses compressed air (100 psig or 690 kPa) as motive fluid, and its discharge port is connected to the outside of the lab through a hose which works as a silencer. The suction port of the ejector is connected to a manifold, which provides suction to all five sampling probes equally. From the manifold, the negative pressure reaches to a ball valve and then to the flowmeter (See Figure 2-8). The ball valve is used to start and stop sampling. In order to connect all the different parts of the sampling system to each other 12.7 mm O.D. (½ inch O.D.) plastic pneumatics hoses along with the pneumatic fittings were used. Sampling from five different locations can be conducted simultaneously which is beneficial for comparing the results (Figure 2-12).

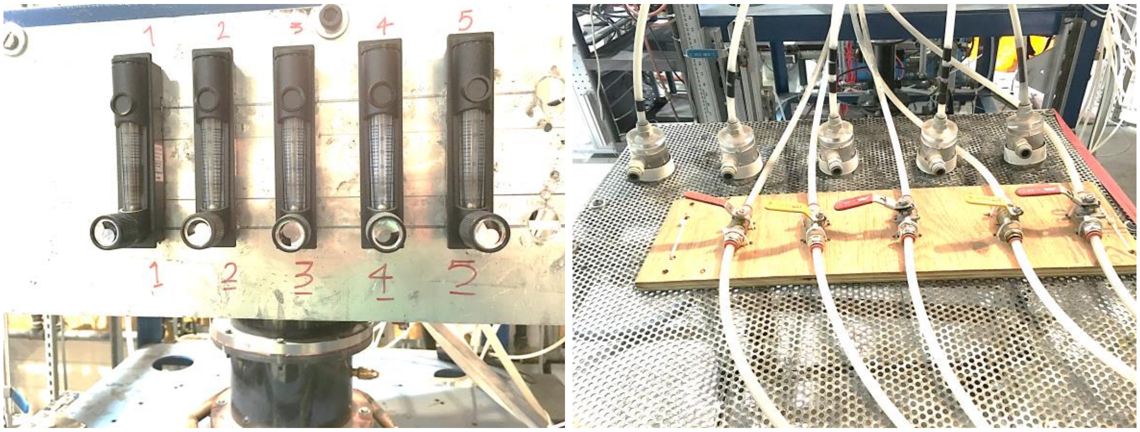

Figure 2-12. Five Sampling systems

2.3 Measurement method

The measurement procedure can be divided into the following stages:

Stage 1: Filling the column: the old bed solids are removed from the column and replaced by fresh solids. Then these solids are fluidized at $V_g = 0.2$ m/s for a few hours for three reasons: to fully dry the bed solids, which may have been stored outdoors, to break possible agglomerates and to thoroughly mix the bed.

Stage 2: Determining the bed surface location. The bed is fluidized at the desired velocity and the pressures along the bed wall are measured. By plotting the pressure data along the bed, one can easily estimate the location of the bed surface.

Stage 3: The position of the probe(s): One should fix the axial and radial position of the probes for that particular experiment. Eleven ports are available on the column lid and cover the cross-sectional area of the column. By choosing a port, one literally has chosen the radial location as each of these ports has a fixed known radial position. By sliding the probes up or down in each port, one can achieve the desired probe axial location. The axial location is defined as the distance between the probe tip and the bed surface. (Bed surface is located at $Z = 0$)

Stage 4: Estimation of the required gas flowrate in the probes: in order to maintain pseudo-isokinetic condition during the measurements, the superficial velocity above the bed should be equal to the velocity in the probe inlet. For this, a program in MS Excel has been developed to calculate the required flowrate in the probe from variables such as freeboard superficial gas velocity, bed pressure, ejector suction pressure, probe mouth area, etc.

Stage 5: Collection vessel preparation: This includes cleaning the bottle and placing a new filter between the two metal rings. It is not necessary to change the filter for each experiment, and one can just clean it using compressed air.

Stage 6: Estimation of the sampling duration (sampling time): One should notice that there is a limitation on the amount of solids can be collected in the vessel, which depends on the sampling time and solids flux. By estimating the solids flux for the current experiment from theoretical models, correlations or previous experiments, one can obtain a reasonable sampling duration. Even though Hazlett (1990) showed that the sampling time has no effect on the results, we try to sample as long as possible to minimize random and weighing errors (Maximum sampling time achievable for each experiment).

Stage 7: Doing experiments: After everything is appropriately adjusted, the system would be ready for doing experiments. The user opens the ball valve for the first probe and at the same time, starts the stopwatch, and continues opening the other valves promptly to allow sampling from other probes. Then, the user sets the flowrates of the 5 flowmeters to the required value calculated in stage 4 using the control valve located on each flowmeter. The user shall monitor the flowmeters during the experiment to ensure the flowrate does not go over or below the required value. Whenever an experiment requires adjusting the flowrate in the middle of the run, the results from that experiment will be not be considered. The user closes ball valves at the end of the sampling time in the same order as they were opened to ensure equal sampling time for all the probes.

It should be noted that for those experiments which require sampling from the cyclone as well as sampling from the probes, the user should climb to the first level of the supporting structure, right after the sampling from probes started, and close the ball valve located between the dipleg and the cyclone, at a certain time, to allow collection of solids from the cyclone. In this case, the user should cut off the main fluidization gas to end the experiment

Stage 8: Registering the results for further analysis: Once the experiment is finished, one disengages the quick connector assembly to empty the collected solids from the cyclone to a vessel. Then, one disconnects the collection vessels. All the vessels are transferred to the Analytical Lab for accurate weight measurements. Once the weight of the solids collected obtained one can calculate the flux using:

$$Flux = \frac{m_{solids\ collected}}{A \times t} \tag{2-1}$$

In above equation, *A* is the cross-sectional area (probe mouth or bed, depending on whether the measurements have been made with an isokinetic probe or the cyclone dipleg), and *t* is the sampling duration.

Then a portion of each sample is taken for analysis with the PSA to determine the size distribution of collected solids. Although coke particles do not present the same electrostatic issues as sand or FCC particles, the size measurements will be performed in an aqueous environment, with surfactants, to prevent particle-particle agglomeration. Accurate size distributions will allow for the determination of the local flux of particle clusters by assuming that the particles inside the clusters have the same size distribution as the bed particles (Baron et al., 1988b). The unused portions are transferred to a bucket and returned to the bed before the next experiments.

2.4 Validation of the sampling system

In order to make sure experimental instruments are working properly, verification experiments were performed by comparing the flux and size distribution results from the cyclone and the sampling probes. The solids collected by the cyclone originate from the entrained solids which make their way through the 4 column exhausts. One should notice that some of the solids which are ejected to the freeboard will return to the bed except the solids which are above the TDH. These solids will be carried out by air to the cyclone.

2.4.1 Finding TDH

It is clear that in the verification experiment, the column exhaust must be above the TDH. The velocity V_g = 0.30 m/s was chosen because the TDHs calculated from theoretical models were lower than the relative location of the exhaust to the bed surface. The predictions from the models are shown in Table 2-1.

Table 2-1. TDH prediction from few different models, $V_g = 0.30$ m/s, current fluidized bed

Model	Predicted TDH(m)
Amitin et al. (1968)	1.92
Baron et al. (1988)	0.14
Horio et al. (1980)	1.02
Zenz (1983)	0.47
Zenz and Weil (1958)	0.92

Poor agreement between predicted values persists due to the reliance on empirical data-fitting in the absence of a fundamental understanding of the TDH phenomenon. However, the model from Baron et al. (1988) seems to have a stronger fundamental theoretical background as they derived their correlations by performing a force balance on clusters ejected into the freeboard and neglecting the drag force and other inter particle forces for the largest clusters. Still, a good prediction of TDH dependents on the prediction of right ejection velocity of particles and consequently prediction of bubbles velocity at the bed surface. Due to this, it is best to find the TDH at different gas velocities by experiments. It is worth noting that the aim of this project is not developing a general model for TDH prediction. The generated data will be only compared to predicted values to check which of the mentioned models are in best agreement with the generated data.

To find the TDH experimentally, the sampling port that was located in the center of column lid was selected (Universal port number: 11- Details in Appendix A). This probe was placed at different distances from the bed surface and the flux and the size distribution at each location was registered. The results are shown below.

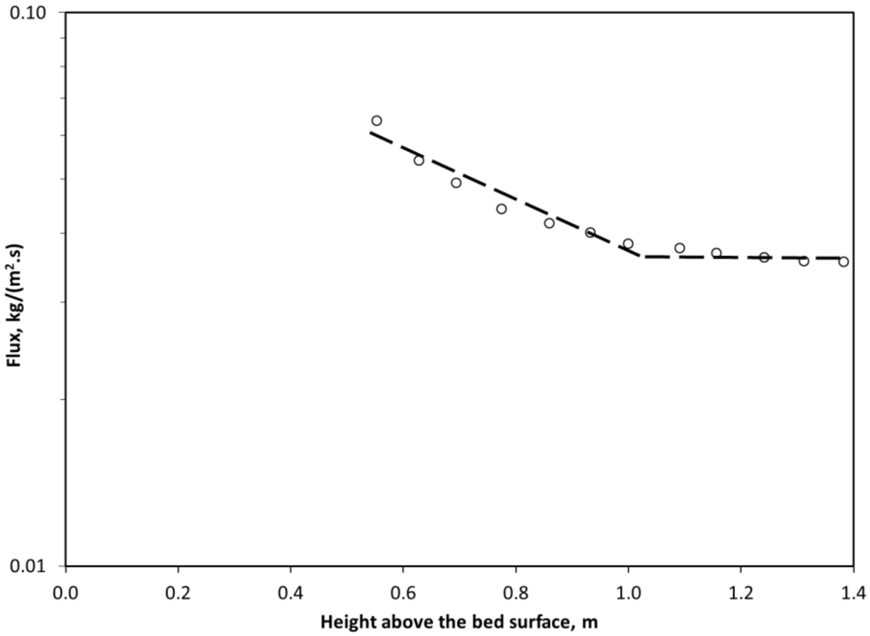

Figure 2-13. Solid Flux vs. height above the bed surface, center probe, dry bed, V_g = 0.30 m/s (Each point averaged over 3 consequent replicates)

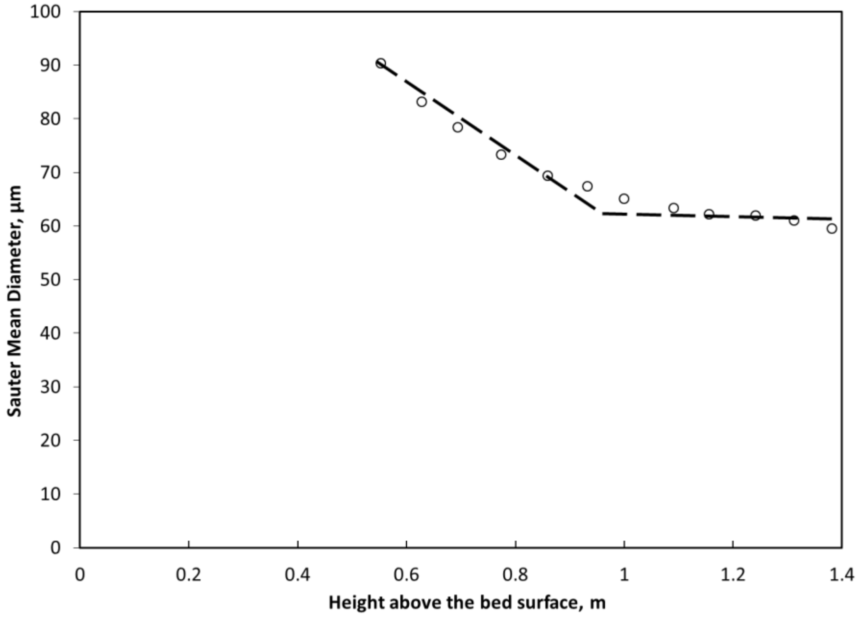

Figure 2-14. SMD vs. height above the bed surface, center probe, dry bed, V_g = 0.30 m/s (Each point averaged over 3 consequent replicates)

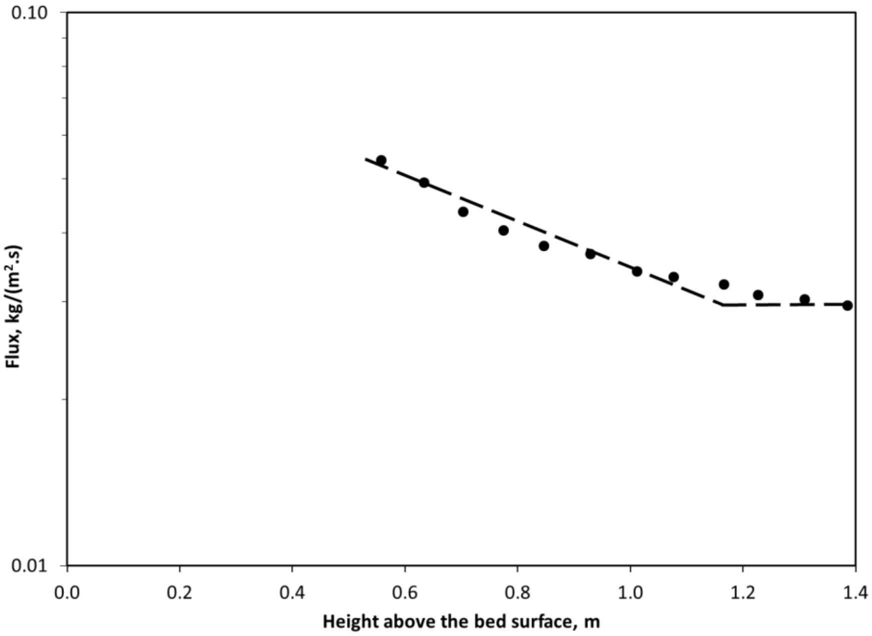

Figure 2-15. Solid Flux vs. height above the bed surface, center probe, wet bed (Wetness = 0.1 wt. %), V_g = 0.30 m/s (Each point averaged over 3 consequent replicates)

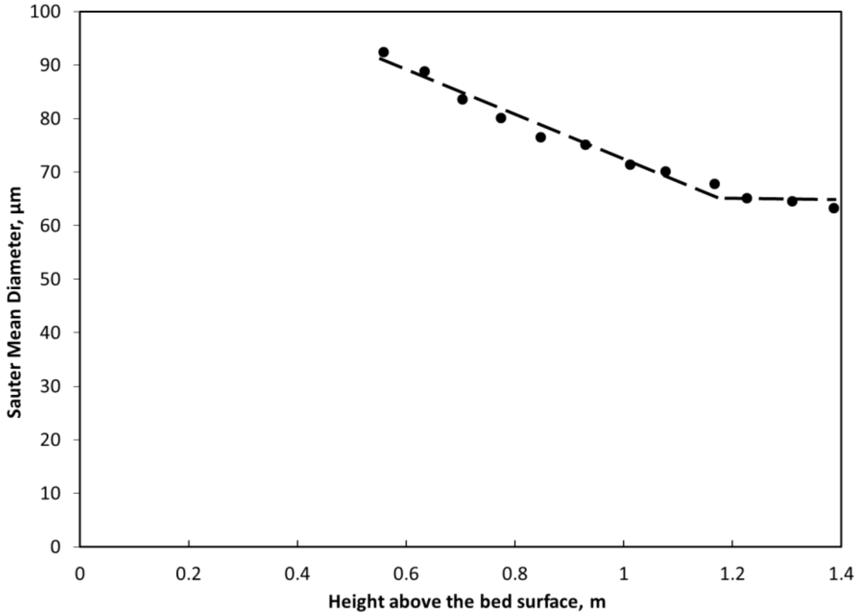

Figure 2-16. SMD vs. height above the bed surface, center probe, wet bed (Wetness = 0.1 wt. %), V_g = 0.30 m/s (Each point averaged over 3 consequent replicates)

Figure 2-13 and Figure 2-14 predict the TDH for the dry bed and V_g of 0.3 m/s around 1 m as the changes in the measured flux and size distribution become negligible. The bed eight (distance from bed surface to sparger) at this velocity fluctuates around 0.6 m.

Figure 2-15 and Figure 2-16 predict the TDH for the wet bed and V_g of 0.3 m/s around 1.2 m. However, there is less accuracy in the value of TDH for wet bed in comparison to the dry bed because as it can be seen from the Figure 2-15 and Figure 2-16, the flux and SMD are still changing beyond 1.2 m. One should keep in mind that due to limitations of the system, measurements beyond the point 1.4 m were not feasible. The bed height (distance from bed surface to sparger) at this velocity fluctuates around 0.62 m.

Considering the above findings and the fact that distance from the exhausts to sparger is 2.1 m ensures us that at this velocity, the column four exhausts are well above the TDH especially in the dry bed.

2.4.2 Organization in taking samples

As mentioned before, there are eleven ports available across the column lid, and five simultaneous sampling is doable over one run. In order to have a redundancy of data, three different arrangements (or configurations) of sampling ports (and sampling probes consequently) were selected (five ports out of eleven ports available for each arrangement) and a color was assigned to each arrangement. The location of the ports in each arrangement is shown in Figure 2-17, and the details are available in Appendix A. As a result of this, for a single run, fifteen samples will be collected. Later on, a different arrangement of the ports which produces enough data from the experiments will be found to save the experimenter much time.

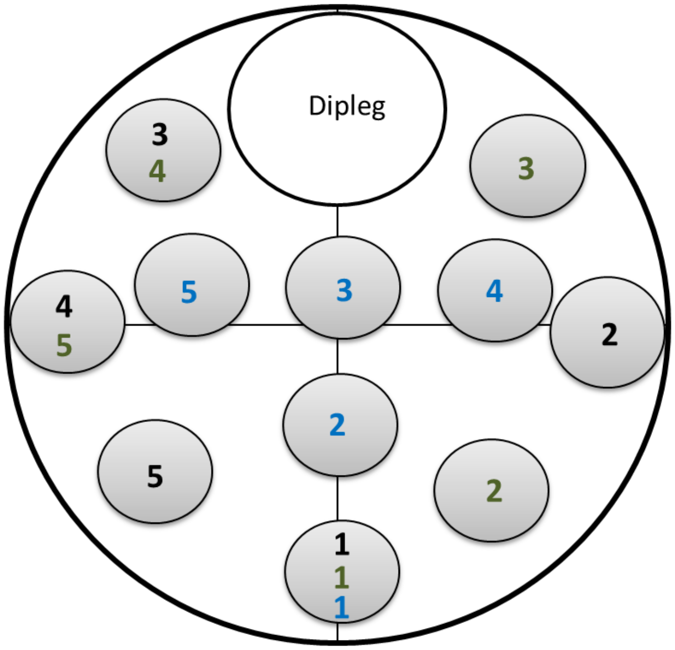

Figure 2-17. Location of ports in each arrangement: ports in the same arrangement have the same color (Drawing not to scale)

2.4.3 Comparing size distribution results from dipleg and sampling probes (Above TDH)

The size distribution of the probes and the dipleg for both wet and dry bed at V_g = 0.30 m/s are plotted. In the results below, the probes are located at the highest distance possible from the bed surface ensuring the probes are above the TDH. Replicates were not performed.

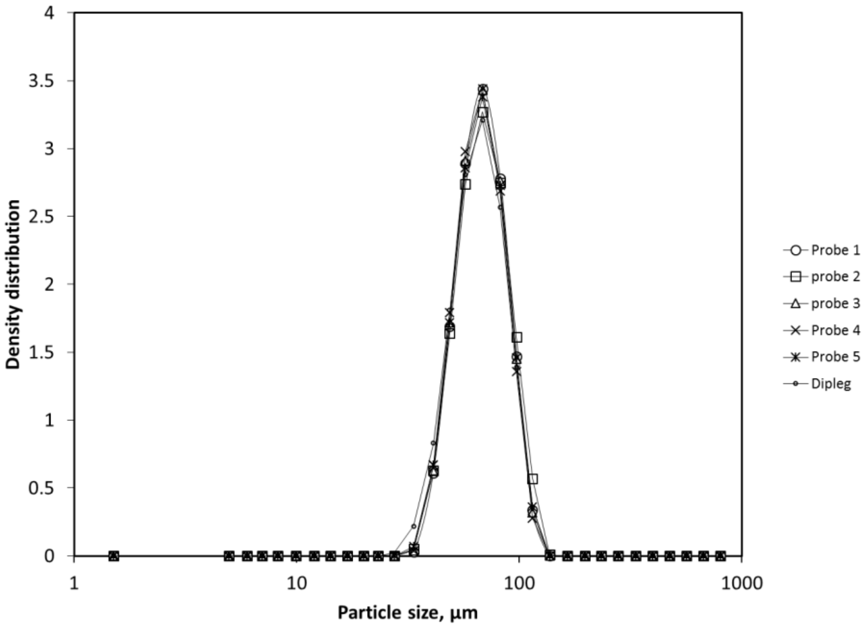

Figure 2-18. Comparison of the size distributions, V_g = 0.3 m/s, Black configuration of figure 1-17, Dry bed, SMD average = 60 micron

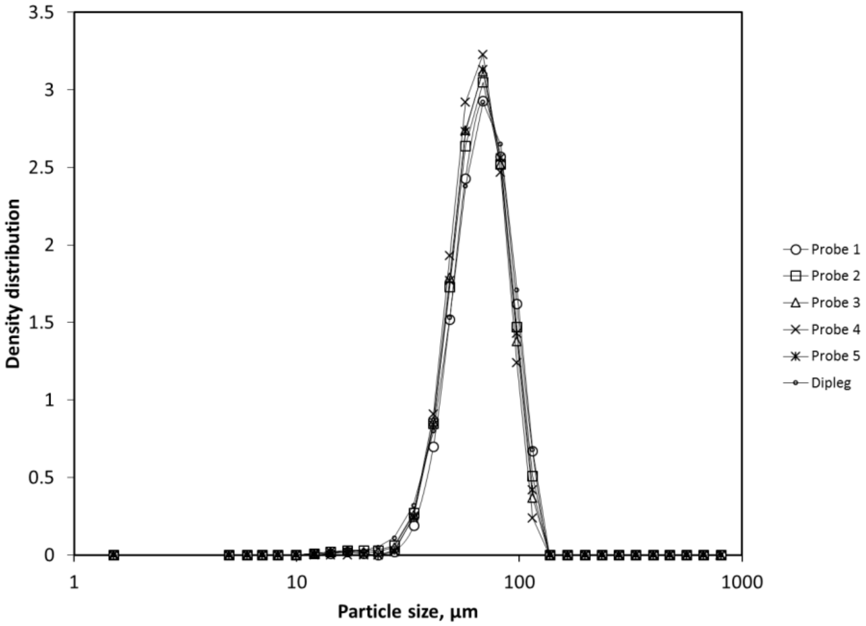

Figure 2-19. Comparison of the size distributions, V_g = 0.3 m/s, Green configuration of figure 1-17, Dry bed, SMD average = 60 micron

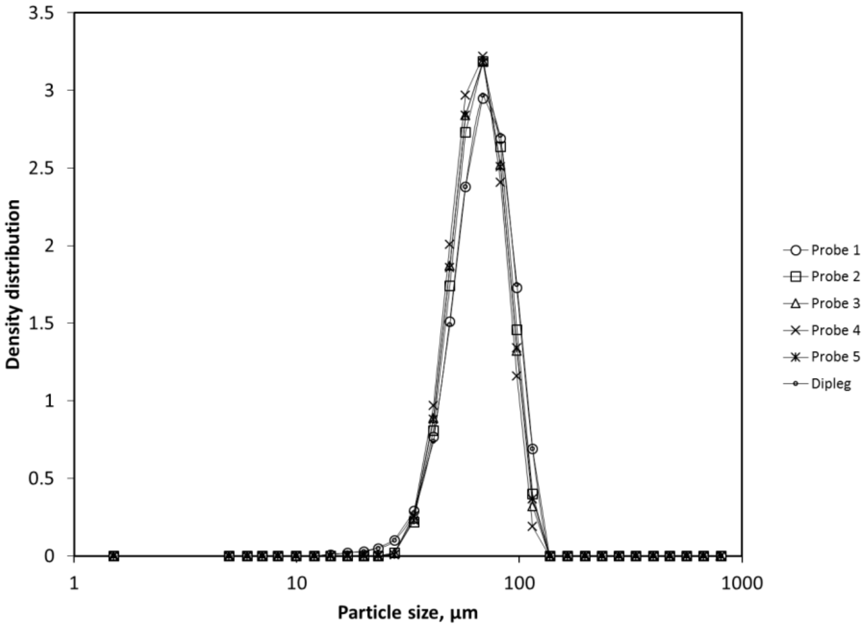

Figure 2-20. Comparison of the size distributions, V_g = 0.30 m/s, Blue configuration of figure 1-17, Dry bed, SMD average = 60 micron

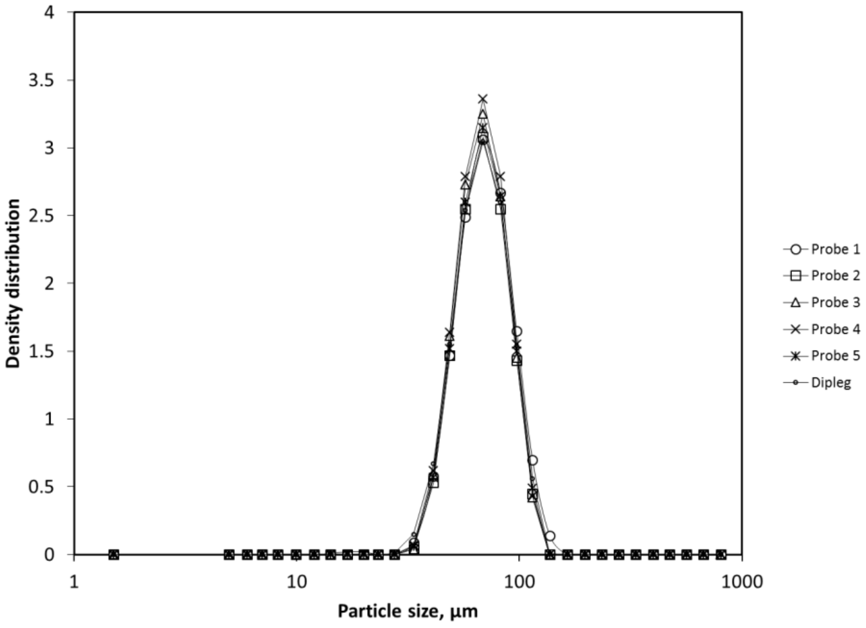

Figure 2-21. Comparison of the size distributions, V_g = 0.30 m/s, Black configuration of figure 1-17, Wetness = 0.1 wt. %, SMD average = 63 micron

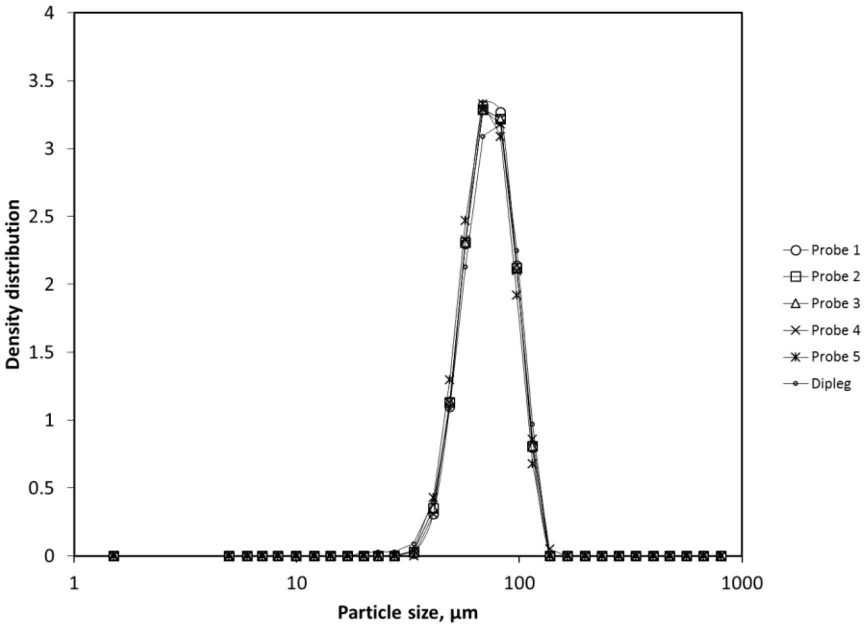

Figure 2-22. Comparison of the size distributions, V_g = 0.30 m/s, Green configuration of figure 1-17, Wetness = 0.1 wt. %, SMD average = 63 micron

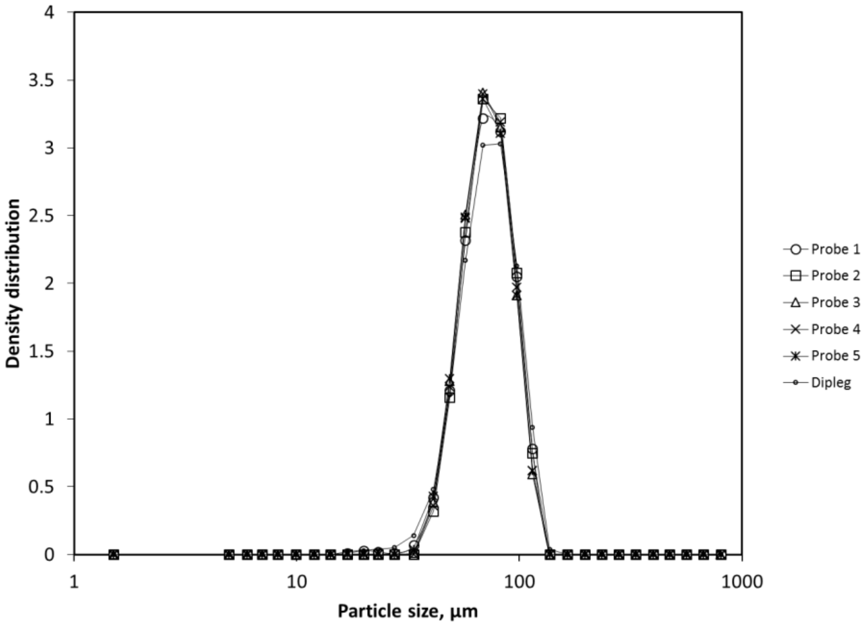

Figure 2-23. Comparison of the size distributions, V_g = 0.30 m/s, Blue configuration of figure 1-17, Wetness = 0.1 wt. %, SMD average = 63 micron

The solids collected from the dipleg have the same size distribution as the solids from the sampling probes. This means that the probes are in pseudo-isokinetic conditions. If this were not true, the probes should have collected larger or finer particles, which would skew the size distribution graphs. More conclusions will be drawn from these graphs in the next chapters.

2.4.4 Comparing solids flux results from dipleg and sampling probes

Here, dipleg and probe solids fluxes are plotted for all the tested configurations described in section 2.4.2. The probes are located at the highest distance possible from the bed surface ensuring the probes are above the TDH. It should be noted that in the results below, no replicate experiments were conducted, i.e. if several points appear for a single configuration, this is because several probes are at the same radial coordinate, but different angular coordinates (Figure 2-17).

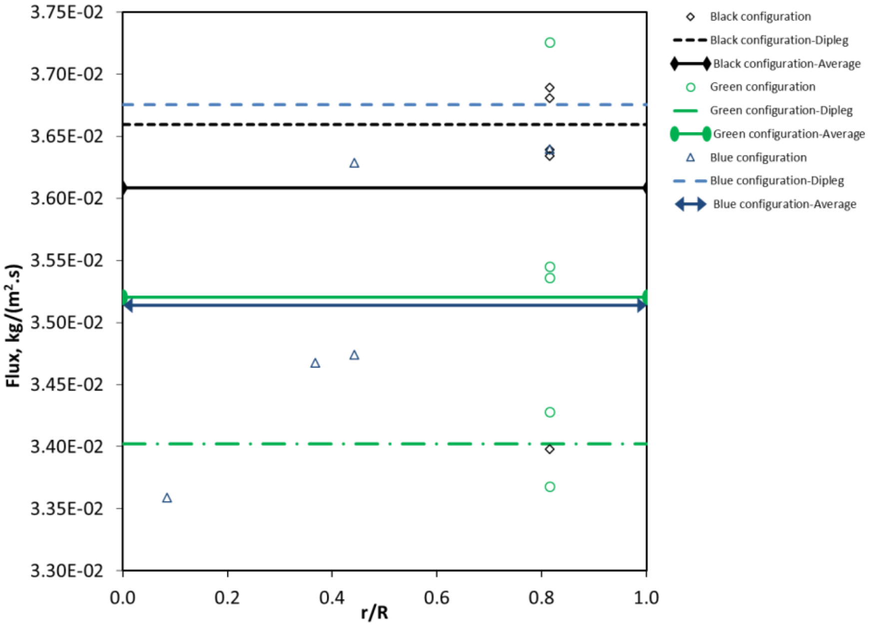

Figure 2-24. Comparison of the fluxes in 3 different probes configuration (Above TDH) and the dipleg, Dry bed, V_g = 0.30 m/s

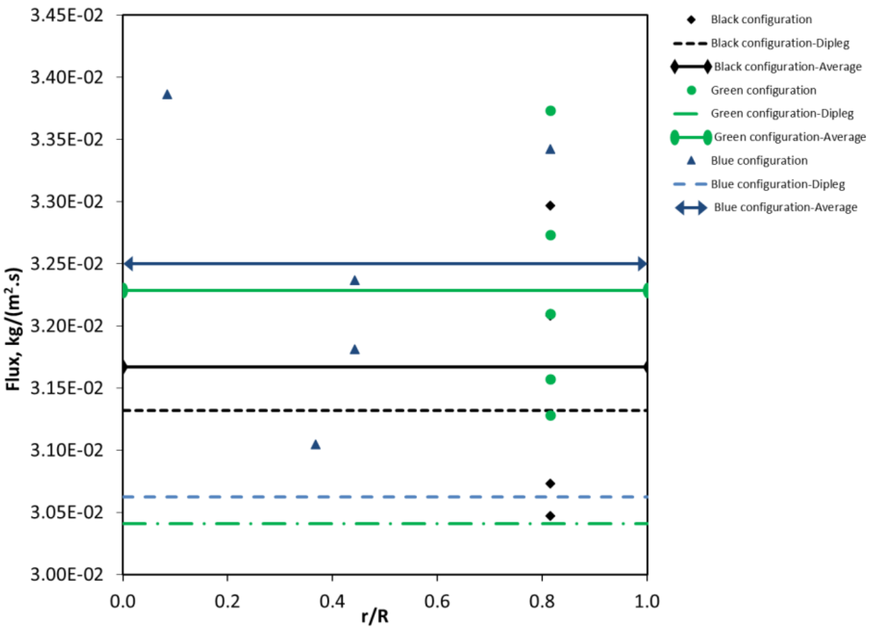

Figure 2-25. Comparison of the fluxes in 3 different probes configuration (Above TDH) and the dipleg, Bed wetness = 0.1 wt. %, V_g = 0.30 m/s

It can be seen that in Figure 2-24 the dipleg flux and the average flux of the probes in three configurations are very close to each other and differ by less than 12 %. This in addition to the graphs from size distribution proves that the sampling system works in pseudo-isokinetic condition.

In Figure 2-25 the average values measured by probes are higher than what is being collected in the dipleg for the wet bed (0.1 wt. %). This is probably because the TDH was higher than 1.4 meters. This assumption can be verified by the Figure 2-25 in which the TDH was not perfectly predicted due to the system limitation. As a result of that, the sampling probes were below the TDH and more solids were collected. One should note that the column exhausts were below the TDH as well, but some of the large entrained solids de-entrained in the connecting hose before reaching the cyclone, and fell back to the column. The amount of large particles, however, were so negligible and did not affect the size distributions (Figure 2-21, Figure 2-22 and Figure 2-23) significantly.

Table 2-2. Variation in dipleg flux measured above TDH

Dry bed			Wet bed		
Configuration	**Flux measured, kg/(m^2.s)**	**% difference relative to average**	**Configuration**	**Flux measured, kg/(m^2.s)**	**% difference relative to average**
Black	3.66E-02	2%	Black	3.13E-02	2%
Green	3.40E-02	5%	Green	3.04E-02	1%
Blue	3.68E-02	3%	Blue	3.06E-02	1%
Average	3.58E-02		Average	3.08E-02	

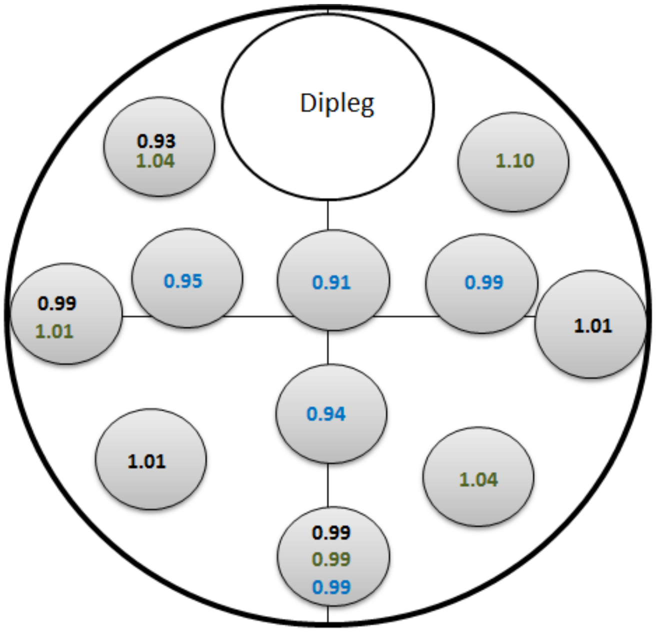

Figure 2-26. Ratio of flux measured in each probe to the flux measured in the dipleg, Above TDH, Dry bed, V_g = 0.30 m/s

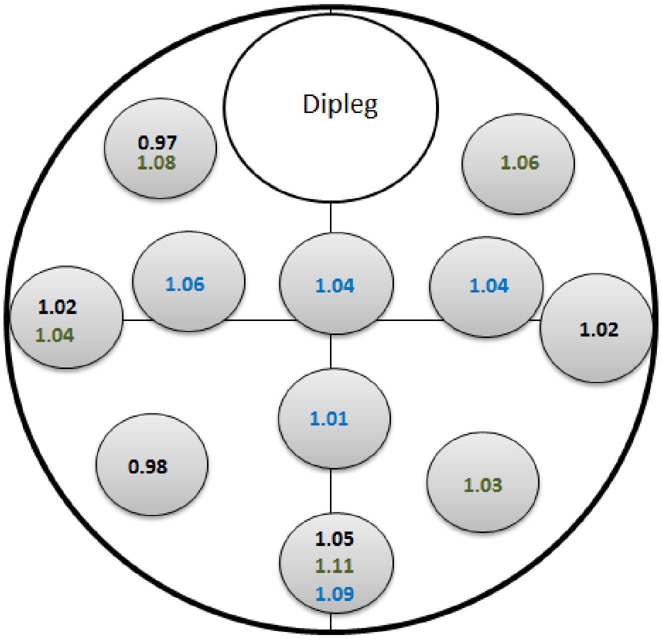

Figure 2-27. Ratio of flux measured in each probe to the flux measured in the dipleg, Above TDH, Bed wetness = 0.1 wt. %, V_g = 0.30 m/s

As can be seen in Table 2-2, minor variation between the dipleg flux registered in the three experiments exists.

One should keep in mind that these variations might have several known and unknown originates for instance they might be due to the fluctuations in the superficial gas velocity, increased electrostatic charges in the hoses connecting the exhausts to the cyclone, variation of air humidity, external forces exerted on the whole structure which result in shaking the equipment and fluidized bed, general experimental error such as mistakes in time-keeping to end the experiments or mistakes in reading the weight shown by the balance, inaccuracy in measurement equipment such as balance and other sources of errors of any kind.

Also, by looking to Figure 2-26 and Figure 2-27, it can be seen that flux measured by each probe in each configuration. This variation exists among the both probes with similar radial but different angular positions, as well as the probes with similar angular but different radial positions. Moreover, the probes with similar angular and radial positions showing some variations (except for the probe 1 in dry bed). However, these variations seem to have a random nature and do not imply any trend, and one cannot conclude that the solids flux is higher near the column wall and vice versa. But, one can conclude the flux measured above the TDH is not dependent on the radial and angular position of the probe. Even though the previous argument is true when the measurements are performed above the TDH so far, but one can simply broaden this by measuring the fluxes below the TDH at different heights for different probe configurations. By looking at Figure 2-28 through Figure 2-33, one can conclude that the radial and angular dependency in any axial position below the TDH does not exist. Besides the lowest and highest values measured in each probe differs by less than 20 percent comparing to the lowest value. This variation would be lower than 15 percent if one compares the extreme values to the average values.

Here it is worth noting that the variation among the data reported for each probe exists due to several known and unknown reasons. For example, the required flowrate in the flowmeters are adjusted manually and monitored by just the user without any special equipment. However, the actual flowrate values in each flowmeter (and the resulting suction velocity in the probe) might be slightly different in reality that cannot be detected by human’s eyes. In addition to that, one should consider that these variation might be due to the fluctuation on the bed surface resulting in more solid being picked up by some of the probes.

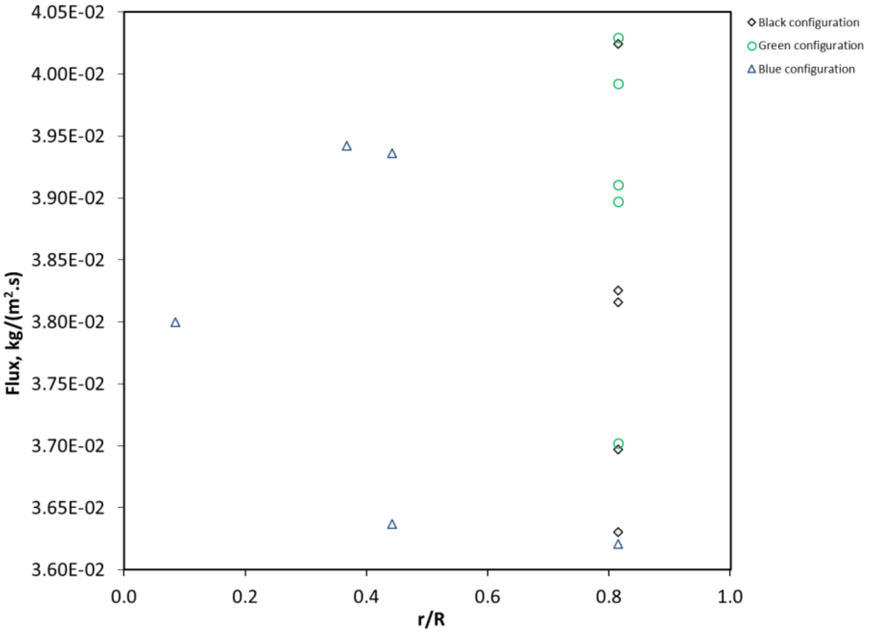

Figure 2-28. Comparison of the fluxes in 3 different probes configuration (Distance from bed surface = 1 m), Dry bed, V_g = 0.30 m/s

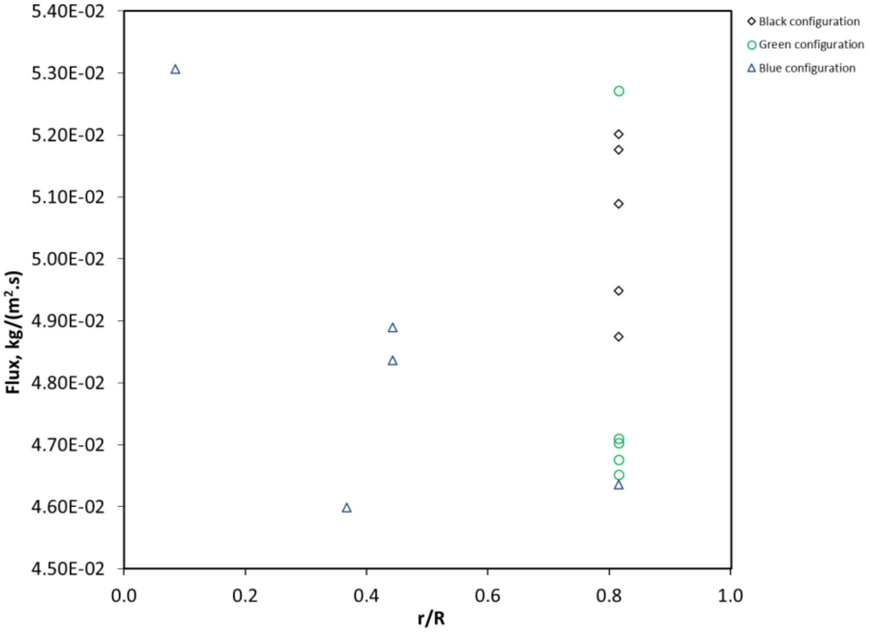

Figure 2-29. Comparison of the fluxes in 3 different probes configuration (Distance from bed surface = 0.7 m), Dry bed, V_g = 0.30 m/s

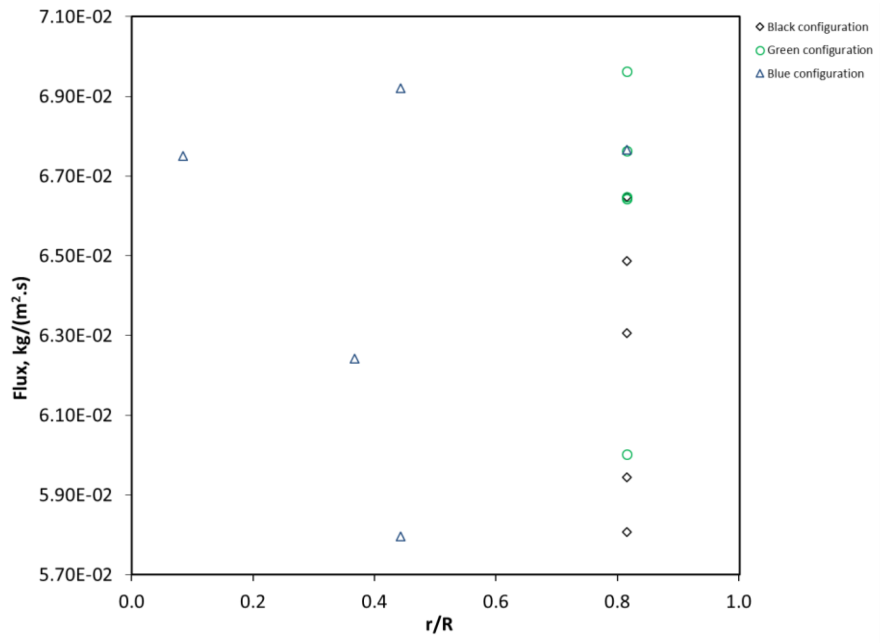

Figure 2-30. Comparison of the fluxes in 3 different probes configuration (Distance from bed surface = 0.55 m), Dry bed, V_g = 0.30 m/s

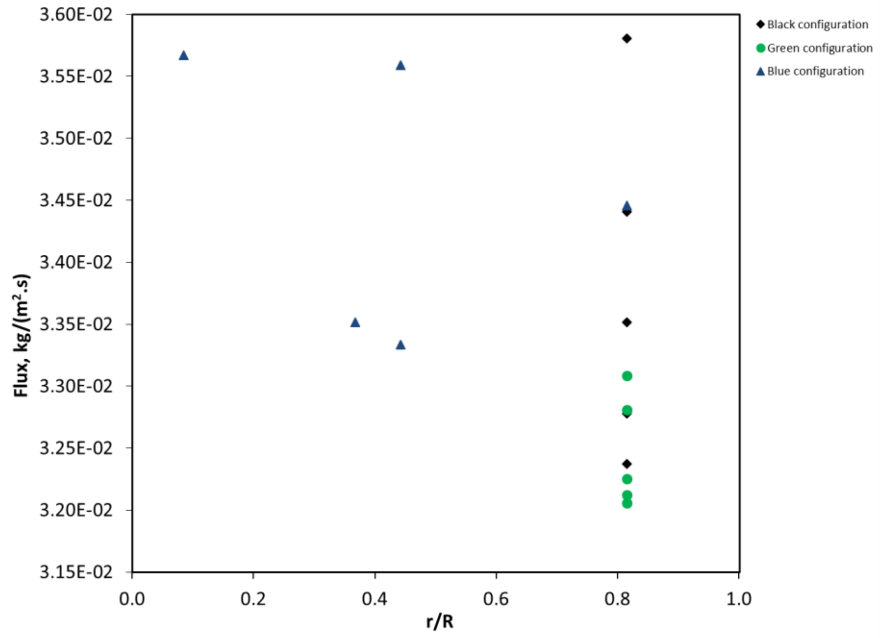

Figure 2-31. Comparison of the fluxes in 3 different probes configuration (Distance from bed surface = 1 m), Wetness = 0.1 wt. %, V_g = 0.30 m/s

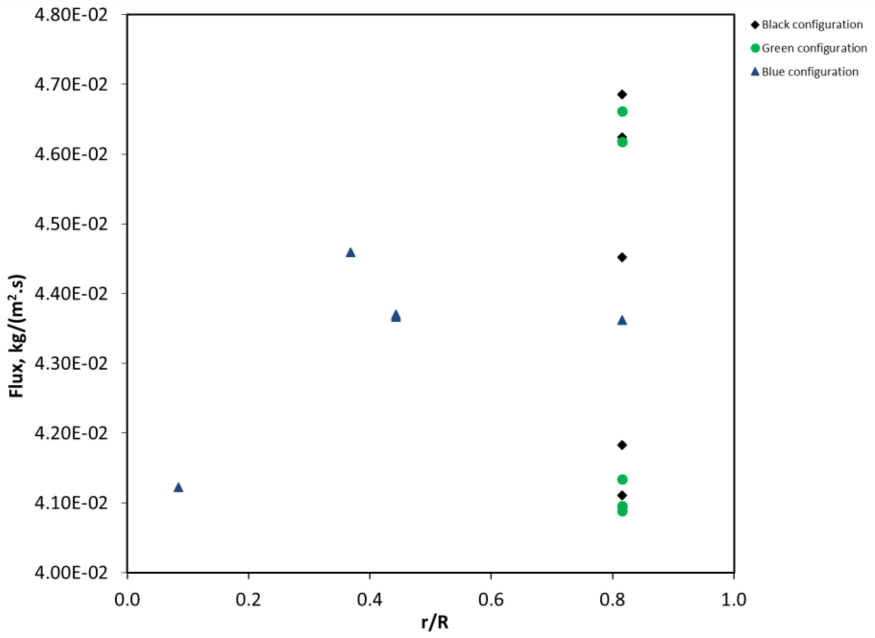

Figure 2-32. Comparison of the fluxes in 3 different probes configuration (Distance from bed surface = 0.7 m), Wetness = 0.1 wt. %, V_g = 0.30 m/s

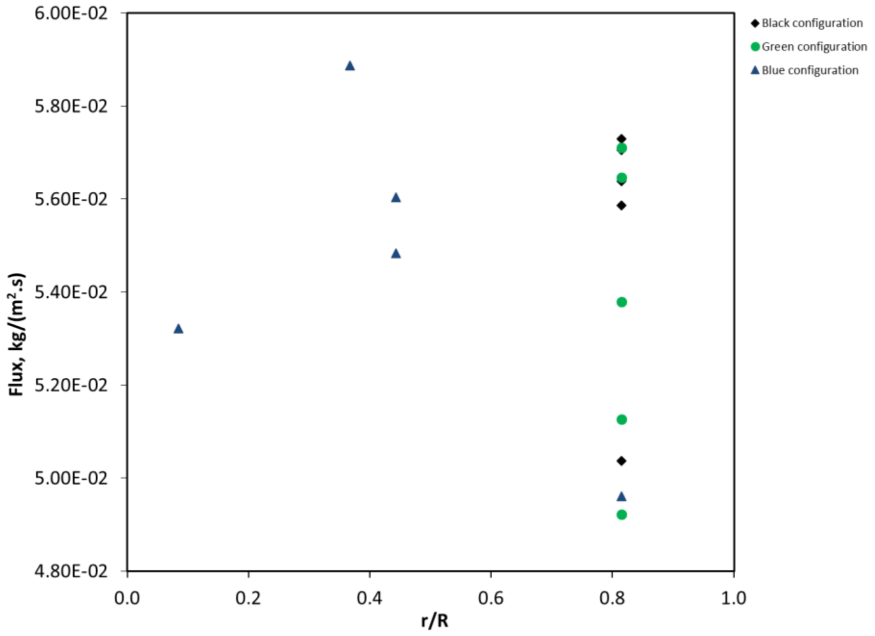

Figure 2-33. Comparison of the fluxes in 3 different probes configuration (Distance from bed surface = 0.55 m), Wetness = 0.1 wt. %, V_g = 0.30 m/s

2.4.4.1 Statistical analysis of the flux registered by probes in different configurations

In order to get a better insight of the variations observed in the solids fluxes measured by the sampling probes, Two-Sample T-Test, using Minitab was performed on the raw data associated with the graphs presented on Section 2.4.4. This test is mainly used to determine if two sets of data are significantly different from each other. Details of this test and its application can be found elsewhere (Montgomery and Runger, 1994). The results of this test on the raw data are available in Appendix E.

From this test, and focusing on the results obtained by comparing the fluxes measured by probes in Black and Green configurations, it can be concluded that the average values obtained from these two configurations are not significantly different. All the ports in these two configurations are located at r/R = 0.81, thus it can be implied that, sampling from any 5 ports out of 7 available probes at r/R = 0.81 will give “not significantly different” average fluxes. In other words, average solids flux at this radial position is not dependent on the angular position of the probes.

Also by comparing the T-Test results on the Blue configuration with Black and Green configurations, it can be seen that no significant difference exists between the average fluxes from these three configurations. All the ports in Black and Green configurations are located near the column wall (r/R = 0.81) while the ports in the Blue configuration are located mainly close the center. Thus, one can conclude that sampling from any 5 ports out of 11 available ports will give “not significantly different” average flux. This proves our previous statement that no radial or angular dependency of the entrained solids flux exists along the freeboard.

The average flux values obtained from the probes in each of the three configuration above the TDH were compared to the dipleg fluxes. For the dry bed, no significant difference among them observed, implying the probe flux and dipleg flux are not significantly different in that experimental condition.

However for the wet bed, the dipleg fluxes and the average probe fluxes found to be significantly different, which proves our previous postulation that for the wet bed in that experimental condition, the sampling probes at their highest point were below the TDH.

2.5 Final configuration

It will be insufficient and inaccurate to report the total solids flux above the TDH based on only one data from one probe. On the other hand, it would be time-consuming to do the experiments for all the proposed configurations considering that one should do replicate experiments. The fluxes should be measured in as many probes as possible to ensure better results. Hence, we have selected a new configuration based on the following argument:

As mentioned before, there are five sampling systems and eleven sampling probes (or ports) available so the maximum number of simultaneous measurements can be five.

By drawing an imaginary line from the center of dipleg to the port 1 in Figure 2-34, it can be seen that corresponding probes on the right and left of this line have symmetrical radial positions.

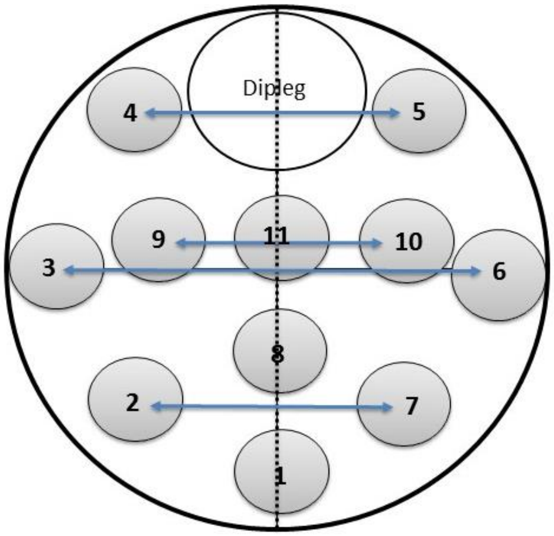

Figure 2-34. Ports position and their universal number (Details in Appendix A)

Considering that one chooses to take samples from the right side of the imaginary line, one will have seven options. Among these seven options, three ports are located near the center of the column (ports number 8, 10 and 11) and have different radial positions. It would be wise to choose these three then. The other four ports have exact same radial positions:

Port 5 is the closest to the dipleg and port 1 is the furthest from it. Assuming that the dipleg may affect the flux measurements by the probes (However nothing has been detected), it would be better to choose the two extremes so that the data from one can compensate the higher or lower value of the other one to result in a more accurate value.

As a result, samples will be taken simultaneously from ports 1, 8, 11, 10 and 5. Besides, to have more accurate and reliable solid flux and particle size distribution values at each height, three replicate experiments will be performed and the average value will be reported.

2.6 Conclusion

A new fluidized bed has been designed and constructed to fluidize a bed of coke particles. This bed is designed in a way to enable us to study the entrainment of solids specifically. Besides, five pseudo-isokinetic sampling systems were developed and tested which collect the entrained solids at different heights. Preliminary tests show that these sampling systems work in pseudo-isokinetic condition or close to it and the results from them can be trusted.

In addition to above findings, it was found that the solids flux increase as the probes get closer to the bed surface, but no radial dependency has been observed at any axial location in the freeboard region. Based on that finding, and to avoid unnecessary experiments, one configuration of the probes were selected.

2.7 References

Amitin, A. V., Martyushin, I.G., Gurevich, D.A., 1968. Dusting in the space above the bed in converters with a fluidized catalyst bed. Chem. Technol. Fuels Oils 4, 181–184. doi:10.1007/BF00718533

Baron, T., Briens, C.L., Bergougnou, M.A., 1988b. Measurement of the Flux of Clusters Ejected from a Fluidized Bed. Powder Technol. 55, 115–125.

Baron, T., Briens, C.L., Bergougnou, M.A., 1988a. Study of the transport disengaging height. Can. J. Chem. Eng. 66, 749–760. doi:10.1002/cjce.5450660508

Furimsky, E., 2000. Characterization of cokes from fluid/flexi-coking of heavy feeds. Fuel Process. Technol. 67, 205–230. doi:10.1016/S0378-3820(00)00103-X

Hazlett, J.D., 1990. Entrainment From Gas-solid Fluidized Beds (volumes I And II). PhD Thesis. Western University. London, Canada.

Horio, M., Taki, A., Hsieh, V.S., Muchi, I., 1980. Elutriation and particle transport through the freeboard of a gas–solid fluidized bed, in: Matsen, J.R.G. and J.M. (Ed.), Fluidization. Plenum Press, pp. 509–518.

Kunii, D., Levenspiel, O., 1990. Entrainment of solids from fluidized beds I. Hold-up of solids in the freeboard II. Operation of fast fluidized beds. Powder Technol. 61, 193–206. doi:10.1016/0032-5910(90)80155-R

Mohagheghi Dar Ranji, M., 2014. Impact of Local Bed Hydrodynamics on Jet-Bed Interaction. PhD Thesis. Western University. London, Canada.

Montgomery, D.C., Runger, G.C., 1994. Applied statistics and probability for engineers. John Wiley & Sons.

Rizk, F., 1976. Pneumatic conveying at optimal operation conditions and a solution of Bath’s equation. Proc Pneumotransp. 3, 443–458.

Sanchez Careaga, F.J., 2013. Hydrodynamics in Recirculating Fluidized Bed Mimicking the Stripper Section of the Fluid Coker. Electron. Thesis Diss. Repos. Western Ontario, London, ON, Canada.

Zenz, F.A., 1983. Particulate Solids: The Third Fluid Phase in Chemical Engineering. Chem. Eng 90, 61–67.

Zenz, F.A., Weil, N.A., 1958. A theoretical-empirical approach to the mechanism of particle entrainment from fluidized beds. AIChE J. 4, 472–479. doi:10.1002/aic.690040417

Chapter 3

3 Entrainment from the fluidized bed with dry material

3.1 Introduction

It was mentioned earlier in Chapter 1 that during the Coking process, the vapors rise through the Fluid Coker until they exit to be refined in downstream processes. Separating entrained solids from vapors is accomplished in cyclones. Fine coke particles from the freeboard region enter the cyclones and are separated from the vapors by means of centrifugal forces in the cyclones. In an ideal manner, these solids entering the cyclones should be dry so that the fouling of the cyclone be minimized. However, during the coking process, wet agglomerates are ejected to the freeboard. The flux of these particles can affect the flux of fines entrained above the Transport Disengaging Height (TDH), although some researchers believe that, in Fluid Cokers, the cyclones are located below the TDH. The entrainment of fine particles in the Coker freeboard contribute to the fouling of the Coker cyclones, which can lead to the premature shut-down of Fluid Cokers. As a result of this it as of high importance and interest to study the entrainment from Fluid Cokers.

This chapter studies the entrainment of fluidized coke particles from a dry bed, while the next chapter studies the impact of bed wetness on entrainment. Entrainment above and below the TDH are both investigated. Although this chapter focuses on coke particles and the Fluid Coking process, its methods and findings should be applicable to other processes.

In a fluidized bed, entrainment is caused by gas bubbles, which burst at the bed surface and eject solids into the freeboard. The flux of entrained solids decreases exponentially with freeboard height (Baron et al., 1988a; Large et al., 1976; Wen and Chen, 1982). The transport disengaging height (TDH) is the freeboard height above which the entrainment rate does not change appreciably (Baron et al., 1988a). In the freeboard zone, the larger particles tend to fall back to the bed while the smaller ones tend to be carried over with the flowing gas. Thus the average size of the entrained particles decreases with freeboard height up to the TDH point above which the average size remains roughly constant (Chew et al., 2015; Yoon et al., 1986). The entrained solids, especially the fines are collected and returned to the bed as the lack of fines in the bed can have detrimental effects on the quality of fluidization. For example, it may result in defluidized zones or result in low reaction conversions due to a degradation of particle-gas mass transfer in the bed (Kunii and Levenspiel, 1991). Cyclones, which are used to recover entrained particles, are typically installed above the TDH, but in some cases, the cyclones may be located below the TDH. To design cyclones and find their best location requires accurate prediction of the flux and size distribution of entrained particles at different heights. The flux of entrained particles and their size distribution depends on flux and size of the particles ejected from the bed surface to the freeboard zone. It should be noted that cyclones may need to be installed below the TDH for economic reasons.

Numerous researchers have tried to predict and model the Transport Disengaging Height (TDH), and more than 25 correlations have been developed since 1958. A recent comprehensive study in this area by Cahyadi et al. (2015) compared the results from all these correlations and found that a poor agreement between the predictions from various correlations. This poor agreement result from the ad hoc inclusion and/or exclusion of parameters, and the use of empirical constants to improve empirical data-fitting in the generation of empirical TDH correlations are not useful in either improving predictions of TDH values or advancing the understanding of the TDH phenomenon. Correlations empirically derived do not perform well beyond the narrow scope of experimental condition tested, while semi-empirical or theoretical models available fall short. The lack of predictive capability of the available TDH correlations appears to stem from a deficiency in an understanding of the impact of interparticle (e.g., cohesion or clustering effects) and inter-species interactions (e.g., collisional momentum transfer effects). However, the model from Baron et al. (1988) seems to have a stronger fundamental theoretical background as they derived their correlations by performing a force balance on clusters ejected into the freeboard, neglecting the drag force and other inter particle forces for the largest clusters. Still, a good prediction of TDH dependents on the prediction of right ejection velocity of particles and consequently prediction of bubbles velocity at the bed surface (Cahyadi et al. (2015) did not use the correlations for bubble properties that were recommended by Baron et al. (1988)). Consequently measurements of the TDH experimentally using a bench or lab scale fluidized bed under relevant conditions is essential.

In predicting the flux and size distribution of entrained particles above the TDH, several models were developed (Zenz and Weil, 1958; Gugnoni and Zenz, 1980; Briens et al., 1988; Benoni et al., 1994). The common assumption among all of these models is that above the TDH, the column operates as a vertical pneumatic line. There are four stages in the evolution of models (Briens, 2015).

Zenz and Weil (1958) modelled the freeboard as a pneumatic transport line. Their model assumes that the fluidization characteristics of the dense bed have no impact on the entrainment above the TDH. This model provides a crude evaluation of the size distribution of entrained particles.

Gugnoni and Zenz (1980) introduced (V_g - U_{mb}) to account, roughly, for the effect of the fluidization characteristics of the dense bed. They used the same crude evaluation of the size distribution of entrained particles as Zenz and Weil (1958).

Briens et al. (1988) accounted fully for the effect of the fluidized bed characteristics. To estimate the size distribution of the particles entrained above the TDH, they also used a crude method which was, however, different from Zenz and Weil (1958).

Benoni et al. (1994) characterized and took into account particle agglomeration in the dense bed and its effect on entrainment. It was found, for particles ranging from cracking catalyst to sand and polyethylene that the assumption, made by prior models that the fines are preferentially entrained, was wrong. Actual experimental data with a pressure polyethylene pilot plant (60°C, 20 atm.) demonstrates this clearly. The explanation is that many of the fines, which have a large surface/volume ratio, will not be present in the bed as individual particles but will be stuck to larger particles. They show how the agglomeration function may be obtained from experimental data (e.g. in a pilot plant). This function depends on the particle and gas properties and is also a "weak" function of the fluidized operating conditions. Presence of many fines in both dense fluidized beds and freeboards in form of agglomerates because of Van Der Waals or electrostatic forces has been experimentally confirmed by Cocco et al. (2010).

Based on this, it will be interesting to find the agglomeration function for a bed of coke particles and use the Benoni et al. (1994) to predict the flux and size distribution of entrained particles above TDH.

Solids concentration/flux below the TDH was also an important subject in the entrainment area. Several researchers have developed correlations and models to predict and measure the solids concentration as a function of freeboard height as well as measuring the flux of solids ejected at the bed surface to the freeboard.

Large et al. (1976) derived the Equation 1-1 and stated that it applies to each particle size cut. Using this they were able to explain the increase in fines concentration with height. They also stated that the variable "A" is independent of particle size.

$$F = F_{\infty} + F_0 exp(-Az) \qquad \textbf{3-1}$$

Where, F is the entrainment rate of particles in the freeboard at a height, z, above the bed surface, and F_{∞}, is the entrainment rate above the TDH.

Kunii and Levenspiel, (1977) assumed 3 phases in the freeboard: 1) gas stream with completely dispersed solids moving upward. 2) agglomerates (or clusters) projected by bubbles and are moving upward. 3) agglomerates returning to the bed. Most of the upward moving dispersed particles are assumed to be generated by attrition of the clusters. They obtained the Equation 3-1 as well.

Wen and Chen, (1982) corrected the model proposed by Large et al. (1976) as that model takes into account the F_{∞} twice at the bed surface:

$$\boldsymbol{F = F_{\infty} + (F_0 - F_{\infty})\, exp(-Az)} \qquad \textbf{3-2}$$

Wen and Chen (1982) used the published entrainment data as well as the corrected model proposed by Large et al. (1976) and concluded that the value of "A" is usually between 3.5 and 6.5 m^{-1}. They stated that that the value of "A" is not a strong function of gas velocity or bed composition. The available data was in bubbling and slugging regimes.

Baron et al. (1988b) modified the model by Large et al. (1976) through some assumptions. They confirmed the presence of clusters and the exponential decay of the clusters flux with height up to the TDH where its value become nil. Based on their observation, they assumed that the most of the ejected particles to the freeboard are clusters and not individual particles, and they could predict the total flux at different heights more accurately. The dominant mechanism for clusters in the freeboard appears to be cluster formation in the bed. Some of these clusters are then subsequently ejected into the freeboard region. Hydrodynamics does not appear to be solely responsible for cluster formation. Cohesive forces such as electrostatics, capillary and van der Waals forces, appear to play a significant role in particle cluster formation (Cocco et al., 2010).

Although it is known that particles ejected into the freeboard are due to bubbles erupting at the surface, the origin of ejected particles remains unclarified and different schools of thought exist on whether particles ejection stems from the bubble nose or bubble wake (Chew et al., 2015). The different origins have been reported to cause a discrepancy of up to one order of magnitude in the entrainment flux at the bed surface, due primarily to differences in (i) particle size distribution above the bed surface, and (ii) particle dispersion in the freeboard. Regarding (i), the bubble nose is observed to preferentially eject fine particles, whereas the bubble wake ejects both fine and coarse particles. According to (ii), the bubble nose aids dispersion of particles after ejection from the bed surface, whereas the bubble wake ejects particle clusters into the freeboard. Measuring the flux of solids ejected to the freeboard has been extensively investigated. However, the entrainment rate at the bed surface is not easy to measure and fluctuates significantly even under a specific operating condition. An indirect solution to do so is obtained by extrapolation of the measured values of F(z) to the bed surface level. For example, Equations 3-1 or 3-2 can be used to smooth the experimental data and obtain F_0 by extrapolation to the bed surface level. The best technique in this area comes from Baron et al. (1988b) which uses both total and cluster fluxes. They used the fact that practically all particles ejected from the bed surface belong to the clusters. This technique uses both the measured vertical profile of the flux of ejected particles and the size distribution of these particles.

Some correlations have been proposed for predicting the flux of solids from the bed surface, for example, the correlations by Wen and Chen, (1982), Pemberton and Davidson (1986), Chen and Saxena (1978), Saxena and Mathur (1984), Briens et al. (1988). Most of these correlations include assumptions, and their application may not be expandable to all ranges.

As a result of the above argument, the objectives pursued in this part of research is:

1- To measure the total flux as well as the size distribution of solids at different heights.

2- To calculate the TDH based on the experimental data, and comparing it with results from correlations and models available.

3- To calculate the flux and size distribution of solids entrained above the TDH based on experimental data and comparing them with the results obtained from different correlations. Then, to find the appropriate agglomeration function to use with Benoni et al. (1994) model for prediction of both flux and size distribution above TDH.

4- Calculating the flux of solids ejected from the bed surface using experimental data and comparing the results with a few well-known correlations.

5- Calculations of cluster and non-cluster fluxes at different heights using the total flux and the size distribution data.

6- Using the cluster model proposed by Baron et al. (1988b) to improve the accuracy of:TDH value, flux of solids ejected at the bed surface and flux of solids at different heights in the freeboard.

3.2 Experimental setup and measuring technique

The experimental setup, as well as the sampling technique and procedure, has been extensively demonstrated in Chapter 2. Here they will be reviewed very briefly:

A 0.19 m I.D column made of Plexiglas was designed and modified as the new fluidized bed. The total column height was 2.61 meter, which later lengthened to 3.7 m by adding an extension section with the same I.D as the original column. Fluid coke with a Sauter Mean Diameter (SMD) of 133 μm and a particle density of 1470 kg/m^3 was used as the bed materials to ensure relevant results. For all the experiments, 12 kg of solids were charged to the column and the bed height as well as the bed mass was measured by monitoring the pressure gradient along the column. Compressed air with near zero percent humidity was introduced to the column through a sparger as the fluidizing fluid.

The column has four exhaust lines, which are located on the very top section of the column at every 90°, enabling us with to benefit from isokinetic sampling probes with a novel design. All the entrained solids are collected by a cyclone, which is connected to the four exhausts, and are returned to the bed through a dipleg. Sampling from the dipleg was performed in some of the preliminary experiments.

The column lid was designed and constructed with eleven ports, so the pseudo-isokinetic sampling measurements were conducted from the top of the column. Ports have been set up at different radial and angular positions so that none of the probes inserted into these ports interfere with each other.

Five new pseudo-isokinetic sampling systems were developed and tested to conduct entrainment-related measurements at different heights. Each system is only capable of measuring the upflux, and it mainly consists of:

1-The sampling probe which is inserted vertically into the column thorugh the ports available on the column lid, and whose vertical location can be easily adjusted as needed. It is made of a plastic conical shape tip which is connected to a metal tube.

2- The collection vessel which consists of a removable jar in which the solids are accumulated and a filter which captures fine particles.

3- The flow control and monitoring instrument which consists of a flowmeter with a control valve.

4- The ejector which provide enough suction air at the probe tip to equalize the air velocity at the probe tip to the one in the freeboard.

Previous studies have shown that pseudo-isokinetic sampling provides accurate results for the measurement of particles entrained from fluidized beds (Hazlett, 1990). Also, this is verified in Chapter 2 through the preliminary experiments.

The measurement and operating procedures for the available system were developed in Chapter 2.

3.3 Determining the gas fluidization velocity and fluidization regime

Prior to any experiment, it was necessary to determine what range of superficial gas velocity is appropriate and will benefit both academic research and industry. According to Pfeiffer et al. (1959), the vessel dimension and operating conditions of a typical Fluid Coker are listed in the table below:

Table 3-1. Dimensions and Operating Conditions of a Fluid Coker (Pfeiffer et al., 1959)

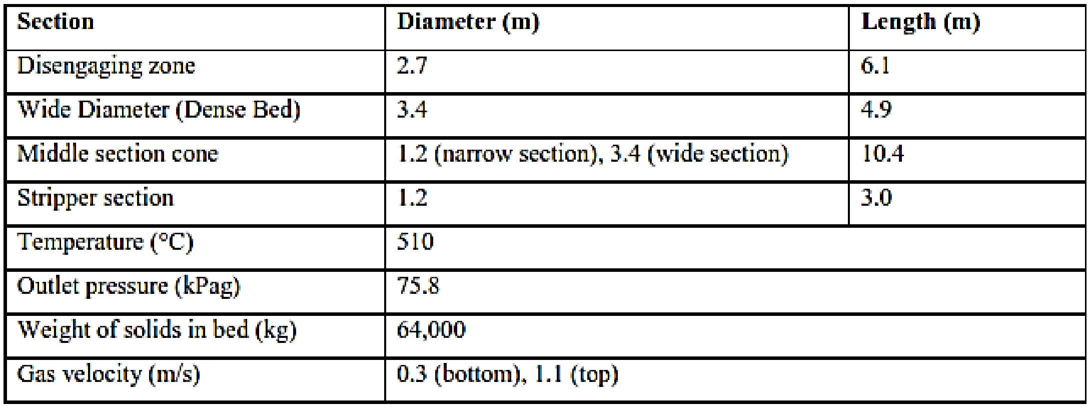

Section	Diameter (m)	Length (m)
Disengaging zone	2.7	6.1
Wide Diameter (Dense Bed)	3.4	4.9
Middle section cone	1.2 (narrow section), 3.4 (wide section)	10.4
Stripper section	1.2	3.0
Temperature (°C)	510	
Outlet pressure (kPag)	75.8	
Weight of solids in bed (kg)	64,000	
Gas velocity (m/s)	0.3 (bottom), 1.1 (top)	

Based on the above table, it would be of high interest to the industry that the entrainment study be conducted at gas velocities close to velocities at the top of Coker. Also, this was strongly recommended by our industrial partner. However, experiments were also conducted at lower velocities to better understand the basic phenomena.

As the gas velocity increases, the fluidized bed undergoes different fluidization regimes. It is well accepted that with increasing gas velocity, a gas–solid fluidized bed goes through particulate fluidization, bubbling fluidization, turbulent fluidization, fast fluidization, and pneumatic transport (Lim et al., 1995). The onset of fluidization is typically characterized by the minimum fluidization velocity U_{mf} which is the superficial gas velocity at which the gas-particle mixture starts behaving in a liquid-like manner. According to the two-phase theory of fluidization, as U_{mf} is exceeded, gas bubbles may appear throughout the bed enhancing the degree of solids mixing. A bubbling fluidized bed is characterized by a gas-solid mixture where the solids are the continuous phase and the gas the dispersed phase. As the superficial gas velocity is increased, particles may become entrained by the gas stream leaving the top of the bed (Berruti et al., 1995).

When the increasing superficial gas velocity reaches a certain critical value, U_c, the bed is said to become turbulent (Chehbouni et al., 1994). A turbulent fluidized bed is characterized by two different coexisting regions: a lower region, where the solids are the continuous phase and the gas the dispersed phase and an upper region, where the gas is the continuous phase and solids are dispersed. Under these conditions particle carryover through the top of the column becomes more significant.

Yerushalmi and Cankurt (1979) first clearly proposed and measured the transition criterion to identify the transition from bubbling/slugging to turbulent fluidization. They defined two gas velocities to demark the transition: U_c the velocity at which the standard deviation of pressure fluctuations reached a maximum and demarcating the beginning of the transition to turbulent fluidization, and U_k (or in some references as U_{tr}) at which the standard deviation of the pressure fluctuations levels off, indicating the end of the transition and the onset of turbulent fluidization (or when the turbulent regime is fully developed) (Zhu and Zhu, 2008). Some other researchers suggested that the turbulent regime starts at U_c (Cai et al., 1990; Rhodes, 1996).

Several measurements have been reported on the values of U_c and U_{tr} and the details can be found in (Zhu and Zhu, 2008). To the best knowledge of authors of this research, the turbulent regime for a bed of coke materials has not been experimentally measured or reported.

In this experiment, fluctuations of the differential pressure signals were measured over distances (from the distributor) of 0.089- 0.209 m and 0.356- 0.450 m. The signals of the differential pressure fluctuations were sampled every ten milliseconds. The total acquisition time was 2 minutes, giving a time series of 120000 points. The velocity was changed from 0.194 m/s to 0.7 m/s at the increment of approximately 0.05 m/s. As the pressure differential is a linear function of the voltage obtained by pressure transducers, the standard deviation of voltage is used for further analysis. It is worth noting that the bed height was fluctuating around an average value of 0.6 m, ensuring that the pressure measurements are done for the dense bed. The results are plotted in Figure 3-1 and Figure 3-2.

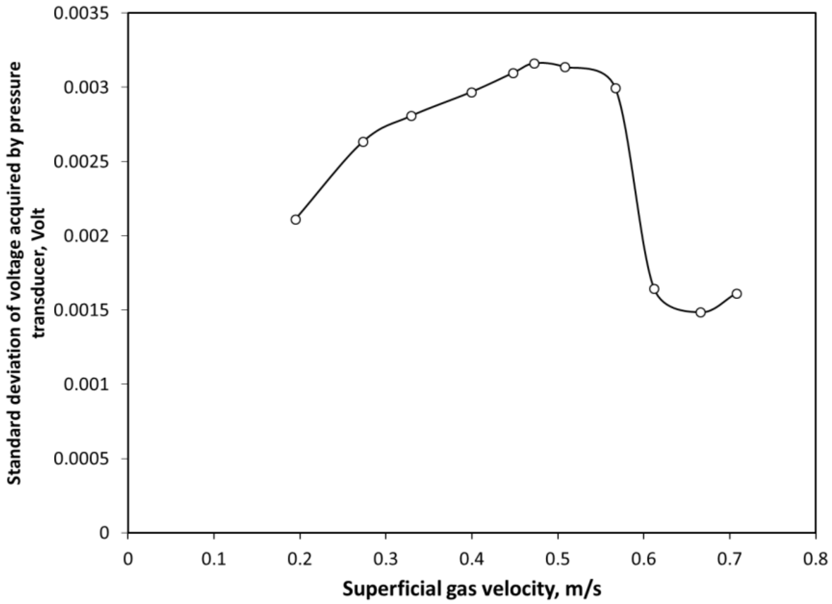

Figure 3-1. Determination of the transition velocity by analysis of the standard deviation of differential pressure fluctuations over distances 0.356-0.45 m above the gas distributor

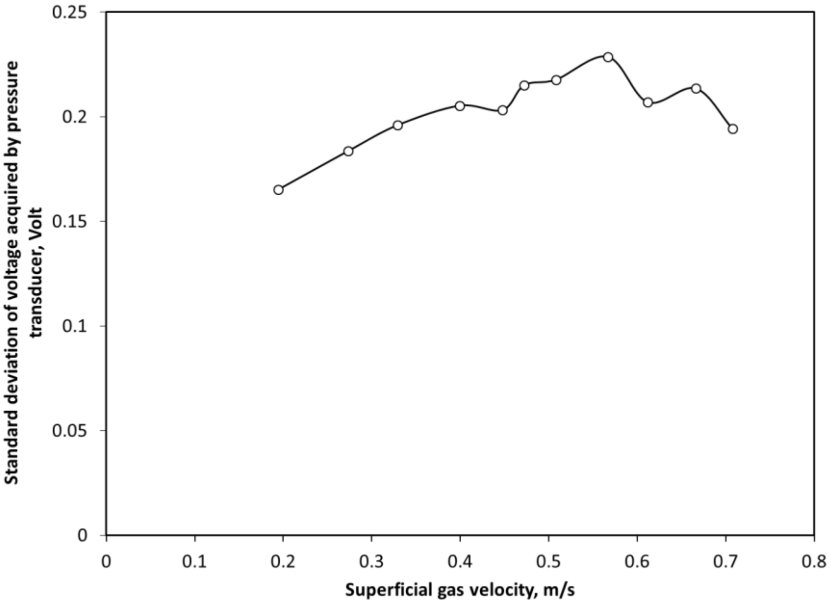

Figure 3-2. Determination of the transition velocity by analysis of the standard deviation of differential pressure fluctuations over distances 0.09-0.2 m above the gas distributor

It is clear that as the standard deviation reaches its peak with increasing gas superficial velocity around 0.45–0.55 m/s and then decreases with further increasing gas velocity. The standard deviation starts to level off when gas velocity is increased beyond 0.6 m/s. This shows that the turbulent regime is in the range of 0.45 to 0.65 m/s. Based on the findings above, three different velocities in three different fluidization regimes were chosen to help understanding how the entertainment at different superficial velocities varies. Besides, most of the correlations and models available to predict the entrainment at the bed surface or above the TDH are developed based on experiments conducted in the bubbling regime. It would be of high interest to determine whether these correlations work for the turbulent regime.

As a result, superficial gas velocities of 0.3 m/s, 0.6 m/s and 0.9 m/s were chosen to investigate the entrainment phenomena in bubbling/slugging, transition regime to turbulent regime and fully developed turbulent regime respectively.

As mentioned before, most of the industrial Fluid Cokers operate at velocities higher than 1 m/s, meaning that the fluidization regime is probably fully developed turbulent regime.

However, one should note that 0.9 m/s was the maximum achievable superficial gas velocity in the bed as increasing the gas velocity beyond that was not safe to operate due to the increase of the pressure inside the column and risk of cracking it. It worth noting that at all gas velocities, the recovery of the cyclone was near 100%, and no significant solids loss was observed during any runs.

3.4 Results and discussion

3.4.1 Pseudo-Isokinetic measurements: General overview

In the previous chapter it was found that the entrained solids flux increases as the probes get closer to the bed surface, but no radial dependency has been observed at any axial location in the freeboard region. Based on that finding, and to avoid unnecessary experiments, one configuration (Section 2.5) of the probes was selected.

As mentioned earlier, the main aim of this study was to measure the entrainment from a bed of coke materials. The experiments were conducted at 3 different velocities. Efforts were made to match the exact desired velocities, but due to some limitations, the exact values were not obtained. In other words, due to fluctuation in the gas velocities, an average value for the gas velocity was obtained, and the standard deviation of gas velocity calculated based on the data obtained.

One should keep in mind that for the experiments for V_g = 0.3 m/s are performed in the column before adding the extension section and the experiments with higher superficial gas velocities were performed in the column with the 1.1 m extension section. For all the experiments, 12 kg of coke particles were poured into the bed.

For each height (distance from the probe to the bed surface), samples from five probes were obtained and the average bed surface was registered. The amount of solids by each probe is then weighted and the collected solids flux were calculated. Also, the size distribution of the samples as well as of the bed for each run were obtained by performing particle size analysis. After these steps, all the collected solids were returned to the bed, ensuring a roughly constant size distribution and mass of particles in the bed. Three replicates were conducted for each probe height. The same procedure was followed for all the heights and all the three velocities. As a result of this, 648 samples were obtained and the PSA was performed on all of them.

The results for averaged total fluxes are plotted below.

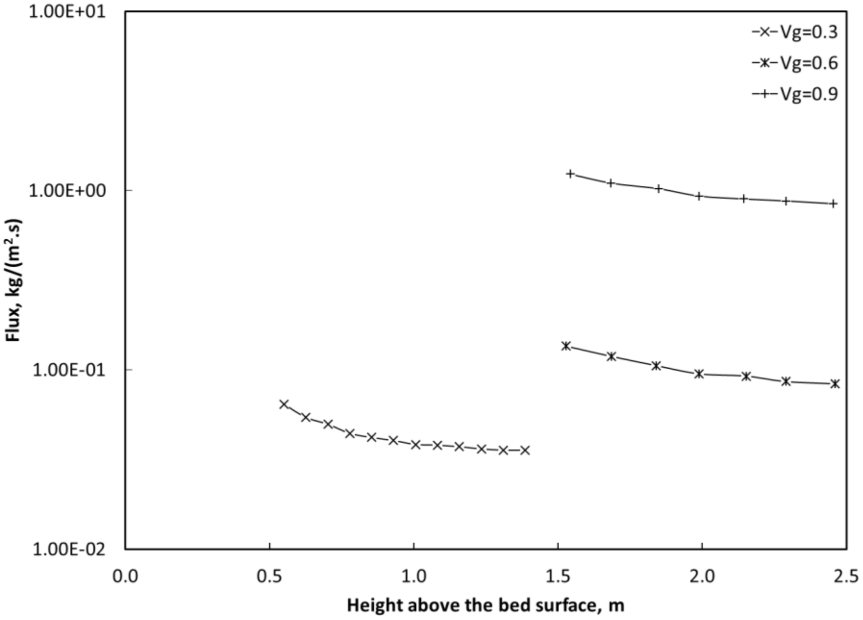

Figure 3-3. Comparison of total fluxes at different velocities

As mentioned earlier, it is well accepted that the bursting of bubbles at the bed surface is the reason for entrainment. Obviously, by increasing the gas velocity the flux of entrained particles are increasing. This is due to two reasons: the bubbles are becoming larger at the bed surface and they have higher velocities, thus ejecting more particles to the freeboard. Also capacity to entrain above the TDH is higher with higher V_g. Further investigations are performed in the next sections.

3.4.2 Pseudo-Isokinetic measurements: TDH results

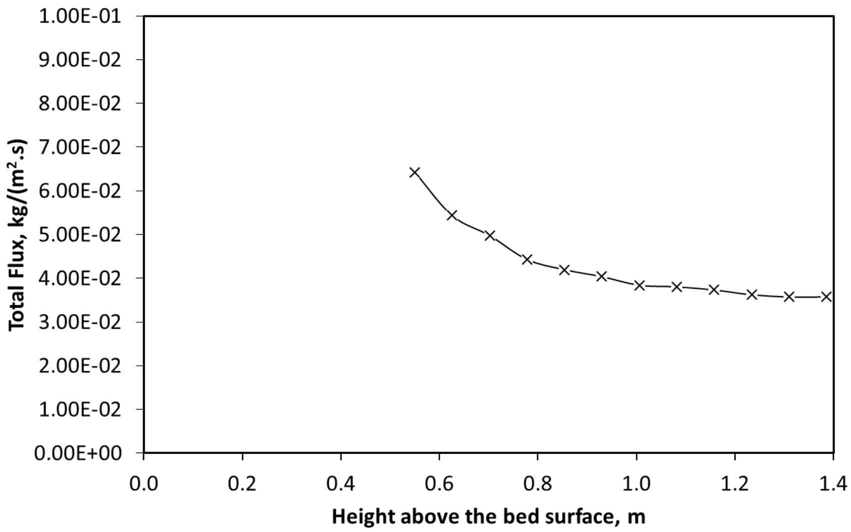

Figure 3-4. Total Flux measured at V_g = 0.3 m/s

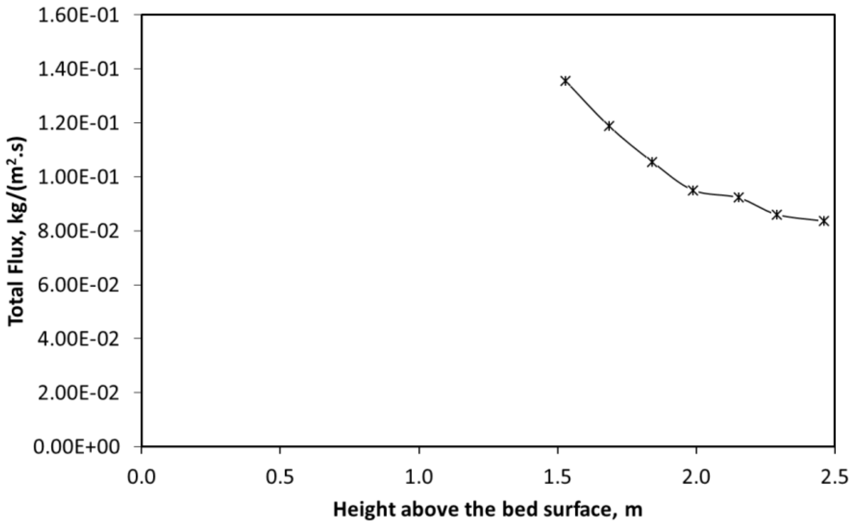

Figure 3-5. Total Flux measured at V_g = 0.6 m/s

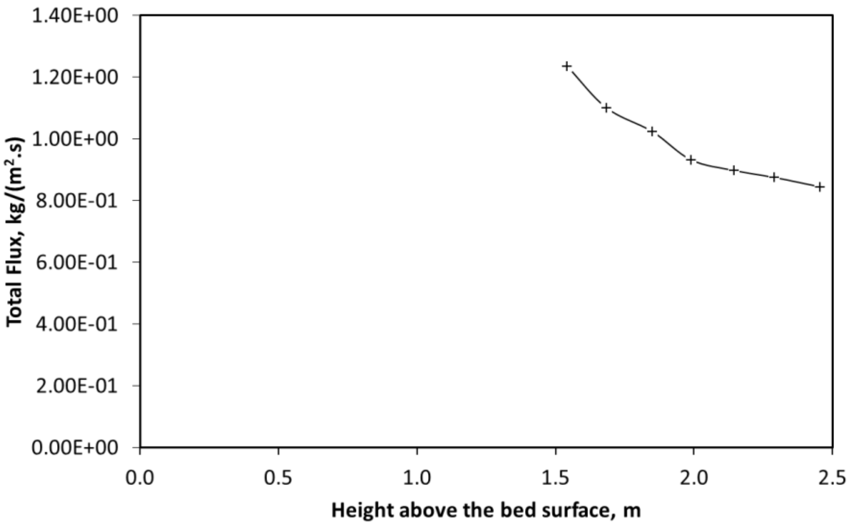

Figure 3-6. Total Flux measured at V_g = 0.9 m/s

As mentioned earlier, the transport disengaging height (TDH) is the freeboard height above which the entrainment rate does not change appreciably. By examining the Figure 3-4, one can visually observe that the total flux, after Z = 1.2 m does not change significantly. Thus TDH at V_g = 0.3 m/s can be estimated to be 1.2 m above the bed surface. These findings are in accordance with findings in chapter 2.

By looking at Figure 3-5 and Figure 3-6 it is difficult to find the TDH visually, thus the percentage of change at each point comparing to the previous point is shown in the table below:

Table 3-2. Percentage of change in Total flux

V_g = 0.6 m/s		**V_g = 0.9 m/s**	
Z, m	change in flux compared to the previous point	Z, m	change in flux compared to the previous point
2.46	-2.03%	2.45	-3.47%
2.29	-2.84%	2.29	-2.54%

2.15	-3.38%	2.14	-3.69%
1.99	-3.98%	1.99	-8.96%
1.84	-9.10%	1.84	-6.96%
1.69	-8.94%	1.68	-10.92%
1.53	N/A	1.54	N/A

As shown in the table, at V_g = 0.6 m/s, after the point Z = 2.3 m the flux varies by approximately 2 %, and at V_g = 0.9 m/s, the flux varies by less than 3 % after the Z = 2.5 m. Finding the TDH experimentally, it is interesting to calculate the TDH by a few well-known correlations. The experimental conditions were fed to the software developed by Briens (2008) and the results are listed in the table below. The correlations can be found in the original work by the authors.

Table 3-3. Prediction of TDH in different gas velocities using different correlations

Correlation	**TDH at V_g = 0.3 m/s, m**	**TDH at V_g = 0.6 m/s, m**	**TDH at V_g = 0.9 m/s, m**
Experimental observation (This study)	1.2	2.3	>2.5
Amitin et al. (1968)	1.92	4.11	6.45
Baron et al. (1988a)-Bubbling regime	0.14	0.27	0.44
Baron et al. (1988a)- Slugging regime	1.78	3.44	5.61
Horio et al. (1980)	1.02	3.25	5.75
Zenz (1983)	0.47	0.79	1.17
Zenz and Weil (1958)	0.92	1.37	1.93

Obviously, the values predicted by each correlations at a specific velocity vary by a few centimeters to a few meters. At the design stage, one may use these correlations to estimate the value of TDH, but due to the variations in the predicted values, it is a necessity to determine the TDH experimentally.

3.4.3 Pseudo-Isokinetic measurements: Flux above TDH

Cyclones are usually installed above the TDH and thus one of the most important criteria in designing the cyclones for fluidized beds is the rate of solids entering the cyclone. There are few correlations that can predict this value. The results from these models are listed in the table below:

Table 3-4. Values predicted by models for flux above the TDH

Correlation	**Flux above TDH at V_g = 0.3 m/s, kg/(m^2.s)**	**Flux above TDH at V_g = 0.6 m/s, kg/(m^2.s)**	**Flux above TDH at V_g = 0.9 m/s, kg/(m^2.s)**
Experimental observation (This study)	0.0351	0.0821	0.8292
Benoni et al. (1994)	0.0377	0.3845	1.2119
Briens et al. (1988)	0.0058	0.0649	0.2354
Gugnoni and Zenz (1980)	0.1466	1.4364	5.3986
PSRI	0.0026	0.1993	1.6602
Zenz (1983)	0.0005	0.0638	0.5942

Table 3-5. Values predicted by models for SMD above the TDH

Correlation	**SMD above TDH at V_g = 0.3 m/s, micron**	**SMD above TDH at V_g = 0.6 m/s, micron**	**SMD above TDH at V_g = 0.9 m/s, micron**

Experimental observation (This study)	63.3	70.5	85.0
All models assuming vertical pneumatic line	54.7	69.9	81.5

As can be seen, a significant difference between the calculated values by different models exist. However, in all the cases, the experimental values fall between the minimum and maximum calculated by the models. It is worth noting that at $V_g = 0.3$ m/s, the model by Benoni et al. (1994) predicts a very close but slightly higher value than the experimental values. This is probably due to the fact that there is agglomeration (fines attach to the larger particles, thus changing the effective bed size distribution) in the bed, but this phenomena was not considered during the calculations. However, at higher velocities none of the models can predict a value close to the experimental values. This simply suggests that these models only work for the conditions similar to the experimental conditions that the data were collected. As a result, direct measurement is required to obtain the flux above the TDH

3.4.4 Pseudo-Isokinetic measurements: Flux ejected from bed surface

As mentioned earlier, the flux of ejected particles from the bed surface affects the flux of fines entrained above the Transport Disengaging Height (TDH). Thus, predicting a correct value of the flux of ejected particles from the bed surface is an important criteria.

Like previous sections, first we are looking at the results predicted by a few correlations:

Table 3-6. Values predicted by models for flux ejected from the bed surface

Correlation	**Flux ejected from the bed surface at $V_g = 0.3$ m/s, kg/(m^2.s)**	**Flux ejected from the bed surface at $V_g = 0.6$ m/s, kg/(m^2.s)**	**Flux ejected from the bed surface at $V_g = 0.9$ m/s, kg/(m^2.s)**
Bubble explosion model: bubble nose model*	1.91	3.87	5.70

Bubble explosion model: bubble wake model**	25.12	50.76	74.80
Wen and Chen (1982)	1.92	11.16	29.41
Briens et al. (1988)	4.75	8.83	14.21

*(Pemberton and Davidson, 1986) **(Saxena and Mathur, 1989)

As can be seen, there is a significant difference between the predicted values.

Using the exponential decay law (Equation 1-1), Large et al. (1976) proposed to extrapolate ln $(F-F\infty)$ as a function of the freeboard height to $Z = 0$ to obtain the flux at the bed surface. The results obtained using linear regression (with 95% confidence intervals) are shown in the table below:

Table 3-7. Parameters obtained from fitting Equation 1-1 to the experimental data

Parameters	**Values at $V_g = 0.3$ m/s**	**Values at $V_g = 0.6$ m/s**	**Values at $V_g = 0.9$ m/s**
***A* Average**	5.30	3.22	3.35
F_0	0.56	4.33	72.76
F_0 Lower 95%	0.28	2.32	16.21
F_0 Upper 95%	1.13	8.12	326.53
Relative margin of error on F_0	75%	67%	213%

The relative margin of error is the percentage of deviation possible around the point estimate at a specific confidence interval. Here, the point estimate is F_0 and deviation around this estimate is calculated at a 95 percent confidence interval. The relative margin of error is calculated by dividing the absolute margin of error (“radius" or half the width of a confidence interval) by the point estimate.

By looking at the Table 3-7, one can see that the relative margin of error on the F_0 is high. This leads us to the next section to use a different method to obtain the flux at the bed surface.

3.4.5 Pseudo-Isokinetic measurements: Cluster flux analysis

Previous studies have shown that determining the flux of clusters improves the accuracy of both the TDH and the flux of particles ejected from the bed surface (Baron et al., 1988a, 1988b). According to Baron et al. (1988b), the maximum height reached by the agglomerates should correspond to the TDH.

Several studies have been performed to measure and model the entrainment in the freeboard section of the fluidized bed. The most successful model is proposed by Baron et al. (1988b) in which they suggested that the entrained particles in the freeboard are divided into two groups: Individual particles and Clusters.

In the freeboard region particles and clusters eventually either rise or fall back depending on their free-falling terminal velocity (U_t) in comparison to the gas superficial velocity (V_g). These particles may also rise up to a certain point depending on their initial velocity resulting from the ejection velocity and bubble eruption at the bed surface. Having this in mind, the particles or cluster with terminal velocity smaller than the local gas velocity will be carried up by the gas and never fall back. As a result, the maximum entrainable particle size (d_{pl}) at a certain superficial gas velocity has the same size as a particle with the free-falling terminal velocity equal to the superficial gas velocity.

Clusters which are the agglomerates of the bed of particles ejected to the bed surface by bubble eruption at the bed surface. The composition of this group of particles is the same as the emulsion phase. As a result, when a sample is taken from a certain point at the freeboard height, any particle which has the diameter larger than the maximum entrainable particle must belong to the clusters. The sample also includes individual particles which have the size equal or smaller than maximum entrainable particle and also ejected along with the clusters.

As a result, the cluster flux can be calculated by:

$$F_c = F_z \frac{\sum_{d_p > d_{pl}} x_{i_{(z)}}}{\sum_{d_p > d_{pl}} x_{i_{bed}}} \qquad \textbf{3-3}$$

In other words:

$$\frac{F_c}{F_z} = \frac{\%\ of\ non-entrainable\ particles\ entrained\ above\ the\ bed\ surafce}{\%\ of\ non-entrainable\ particles\ in\ the\ bed} \qquad \textbf{3-4}$$

The difference between the total flux and the cluster flux represents the flux of individual particles:

$$F = F_I + F_c \qquad \textbf{3-5}$$

The exponential decrease of the entrained particles with freeboard height has been reported by several authors and was reported to be due to the exponential dissipation of effective gas jet velocity with freeboard height and also from the fact that particles ejected to the freeboard follow a certain velocity distribution (Baron et al., 1988a). As a result, the Equation 1-1 proposed by Large et al. (1976) can be used to represent the entrainment rate or flux of solids at different freeboard heights. By using the same exponential law for the clusters:

$$F_c = (F_c)_\infty + (F_c)_0 \exp(-A_c z) \qquad \textbf{3-6}$$

Where $(F_c)_\infty$ is the cluster flux entrained above the TDH, $(F_c)_0$ is the cluster flux ejected from the bed surface and A_c is the constant for a given operating conditions.

Baron et al. (1988b) made three important assumptions base on their observation to simplify the model:

- Above the TDH, the cluster flux is negligible and the total flux is equal to the flux of individual particles.
- Below the TDH, the flux of individual particles is close to its value above the TDH.

- Besides, they assumed that the flux of individual particles ejected from the bed surface $(F_I)_0$ is always very small in compare to the total flux of particles ejected from the bed surface.

As a results of those assumptions, they derived:

$$F = F_\infty + F_0 \exp(-A_c z) \qquad \textbf{3-7}$$

Using the above equation, they claimed that they could successfully and more accurately calculate the flux of solids ejected from the bed surface.

In order to find the cluster flux, one is required to calculate the maximum entrainable particle size at that superficial velocity. As mentioned earlier, maximum entrainable particle size is equal to the size of the particle which has the same free-falling terminal velocity equal to the gas superficial velocity. The fluctuation was observed in the gas superficial velocity, thus an average value obtained and the maximum gas velocity was calculated with 95.5% confidence interval. For calculating the free-falling terminal velocity, the equation from Briens (1991) was used.

Table 3-8. Presentation of actual velocities and maximum entrainable particle

Target (Nominal) superficial gas velocity, m/s	**Average gas velocity measured, m/s**	**St. dev of gas velocity, m/s**	**Maximum gas velocity with 95% confidence interval, m/s**	**d_{pc}, micron**
0.3	0.29	0.015	0.32	95.0
0.6	0.58	0.015	0.61	146.3
0.9	0.81	0.030	0.87	191.5

It has been observed that the d_{pc} falls between the two size cuts reported by the Particle Size Analyser, thus an interpolation was required. For this reason, it was assumed that the particle size distribution between the two size cuts follows a normal (Gaussian) distribution. The exact desired value then obtained by interpolating between these two points. By finding the cumulative size distribution at that d_{pc}, the cluster flux is calculated using the Equation 3-3. The flux of non-cluster particles was calculated by subtracting the cluster flux from the total flux at each height. The results are available in Appendix B in tabular format. The cluster, non-cluster and total flux at each velocity are plotted below.

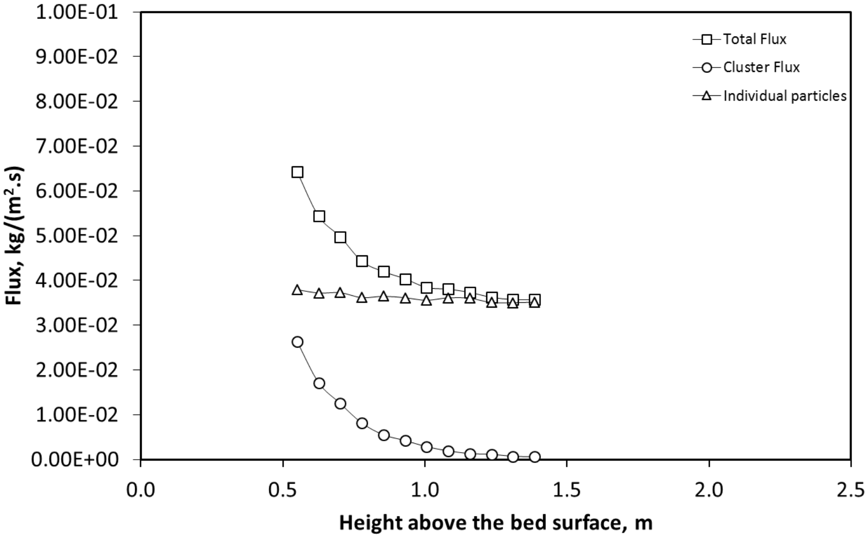

Figure 3-7. Cluster, non-cluster and total flux at V_g = 0.3 m/s

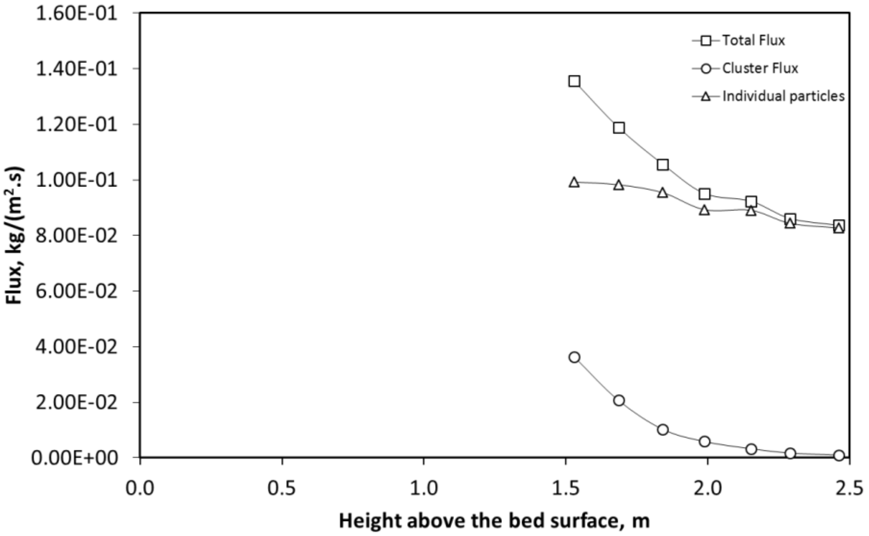

Figure 3-8. Cluster, non-cluster and total flux at V_g = 0.6 m/s

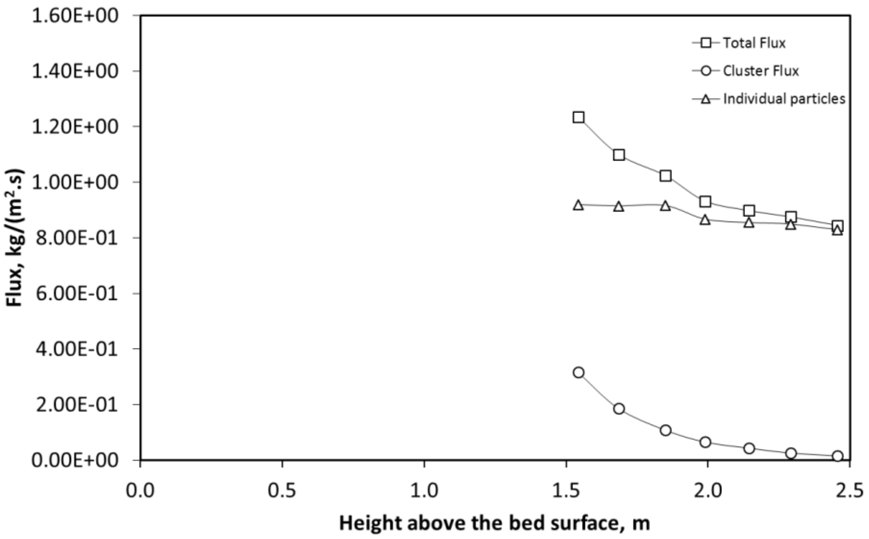

Figure 3-9. Cluster, non-cluster and total flux at V_g = 0.9 m/s

By increasing the gas velocity, the flux of both cluster and non-cluster particles are increasing. As mentioned earlier, increasing the superficial gas velocity results in formation of larger bubbles at the bed surface, which travel at higher velocities upward. The increase in the gas velocity resulted in increasing the cluster flux, suggesting that the particles are ejected from the bed surface in the form of clusters. Also, the total flux decays exponentially with freeboard height and the same shape for decay of clusters has been observed, verifying that the particles ejected to the bed surface as clusters.

The non-cluster flux increase with increasing gas velocity as well simply due to the fact that at higher velocities more particles in the bed have terminal velocities greater than the superficial gas velocity and thus, have more chance to be ejected and be carried out by the upflowing gas. The other interesting point here is that for each gas velocity, the value of non-cluster particles flux does not change appreciably, and this will be more obvious when one extrapolates the values to Z = 0, where the bed surface is. Also, the reduction in the non-cluster flux is negligible in comparison to the cluster flux across the freeboard. The minute decay of non-cluster flux with height can be justified by assuming that the falling clusters shed the non-cluster particles and drag them down to the bed.

The non-cluster flux is more dominant at distances far from the bed surface, while the cluster flux is more dominant near the bed surface. If one extrapolates the values of the flux obtained far from the bed surface (similar to what we have) to get the flux of ejected particles from the bed surface may obtain erroneous results as one has inadvertently extrapolated the non-cluster flux to the bed surface. This will be discussed further later.

To perform a deep investigation, it is required to perform a linear regression on the logarithm of cluster flux data. The results are shown in the table below.

Table 3-9. Parameters obtained from linear regression of the logarithm of the cluster flux vs. height

Parameters	**Values at V_g = 0.3 m/s**	**Values at V_g = 0.6 m/s**	**Values at V_g = 0.9 m/s**
A_c Average	4.58	3.99	3.27
F_0	0.29	16.85	46.89
F_0 Lower 95%	0.24	13.66	36.99
F_0 Upper 95%	0.37	20.78	59.43
Relative margin of error on F_0	22%	21%	24%

3.4.5.1 Cluster flux analysis: TDH determination

By definition, the cluster flux is nil above the TDH. This characteristic height can thus be defined as the height where cluster flux become negligible compared to the total flux. Baron et al. (1988b) defined as the minimum cluster flux that can be measured experimentally. This value in their case was 10^{-4} kg/(m^2.s) which is similar to ours and thus they wrote:

$$Z = \frac{1}{A_c} \ln \frac{F_0}{F_c} \qquad \textbf{3-8}$$

$$TDH_1 = \frac{1}{A_c} \ln(10^4 F_0) \qquad \textbf{3-9}$$

However, other authors have defined TDH in different ways. For example, Wen and Chen (1982) defined TDH as the height where the entrained flux is within 1% of the flux entrained above the TDH. As a result one can write:

$$TDH_2 = \frac{1}{A_c}(\ln 100 + lnF_0 - lnF_\infty) \qquad \textbf{3-10}$$

Pemberton and Davidson (1986b) defined TDH as the freeboard height where:

$$\frac{F_0 - F}{F_0 - F_\infty} = 99\% \qquad \textbf{3-11}$$

Which can be approximated to:

$$\frac{F - F_\infty}{F_0} = 1\% \qquad \textbf{3-12}$$

Considering the exponential decay law:

$$Z = \frac{1}{A_c}\, ln \frac{F_0}{F - F_\infty} \qquad \textbf{3-13}$$

Joining the two equations:

$$TDH_3 = \frac{ln100}{A_c} = \frac{4.6}{A_c} \qquad \textbf{3-14}$$

One should note that the A and F_0 can be obtained by linear regression of total flux or cluster flux. As the parameters obtained by cluster flux analysis are more accurate, they will be used. The results are shown below:

Table 3-10. TDH calculated from experimental data

	V_g = 0.3 m/s	**V_g = 0.6 m/s**	**V_g = 0.9 m/s**
TDH observed (This study), m	1.2	2.3	>2.5
TDH_1, m	1.74	3.02	3.98

TDH_2, m	1.46	2.48	2.63
TDH_3, m	1.00	1.15	1.40
Average of TDH_1 and TDH_3	1.37	2.08	2.69

It can be seen that the best agreement with the observation is derived from the Equation 3-10 which was proposed by Wen and Chen (1982). This is because this equation considers the value of F_∞ in the calculation. However, the other two equations calculate the TDH without considering the value of F_∞ which can come very useful in several cases. For example, by a few measurements of the total flux below the TDH, the slope *A* of the exponential decay and the flux ejected from the bed surface can be easily estimated by the linear regression and extrapolation technique which was described earlier. Then by using these two equations, one can easily estimate the TDH. It can be seen that Equation 3-9 overestimates the TDH while Equation 3-14 underestimates the TDH. However, the averaged value of those two have a very good agreement with the values of observed TDH, giving the engineer at the design stage, an opportunity to estimate a value for TDH more accurately.

3.4.5.2 Cluster flux analysis: Flux along the freeboard

By using 3-8 and the parameters obtained from the linear regression available in Table 3-9 one can estimate the value at any height. To compare the values, they have been plotted in the figures below:

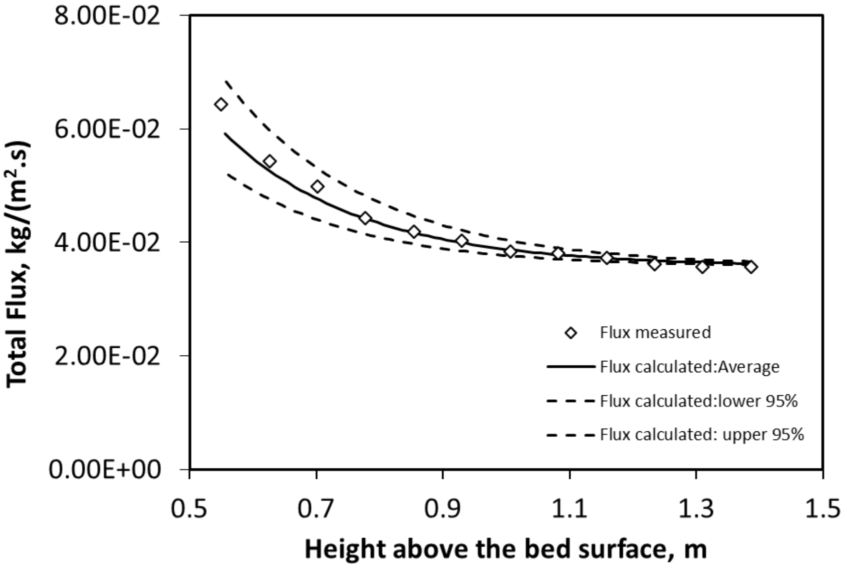

Figure 3-10. Comparison of fluxes in $V_g = 0.3$ m/s

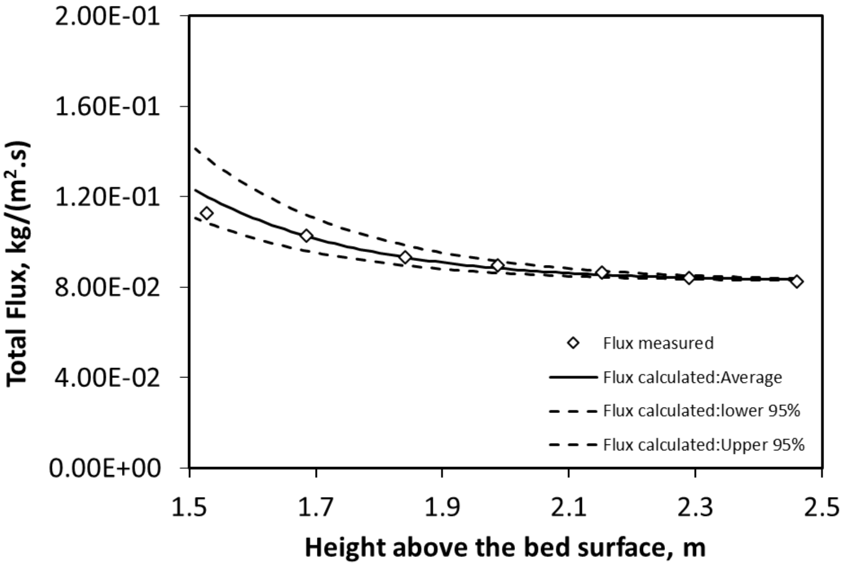

Figure 3-11. Comparison of fluxes in $V_g = 0.6$ m/s

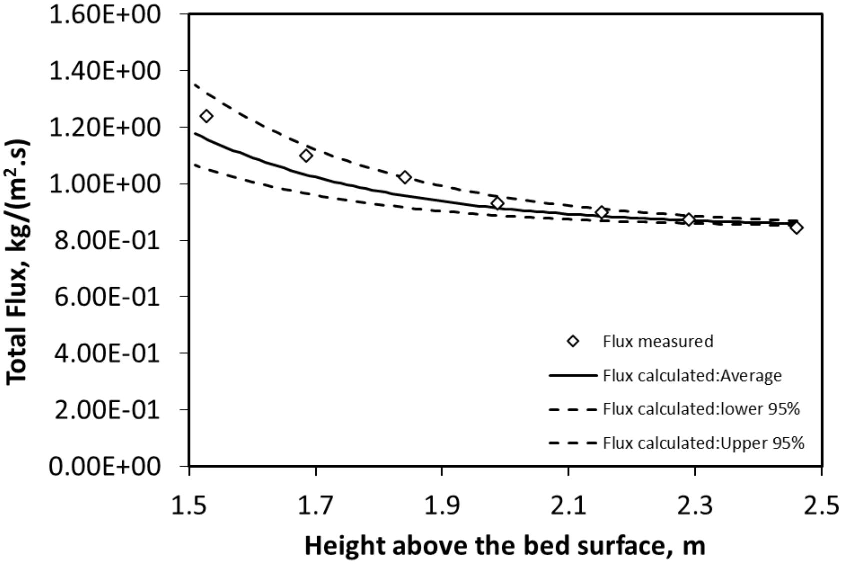

Figure 3-12. Comparison of fluxes in $V_g = 0.9$ m/s

It can be seen from the graphs that the measured flux falls within the two calculated values with 95% confidence intervals.

3.4.5.3 Cluster flux analysis: Flux ejected from bed surface

The flux of ejected particles can be obtained by extrapolating the cluster flux to Z = 0. The values obtained have less errors comparing to the obtained by extrapolating the total flux to the bed surface. By comparing the results from Table 3-7 and Table 3-9, it can be seen that the relative margin of error on F_0 (at a 95% confidence interval) was dropped to one third when one uses cluster flux instead of the total flux. Thus, one can more accurately predict the flux ejected from the bed surface resulting in more accuracy in predicting the flux above the TDH as well as any height of the freeboard. This makes sense as the cluster flux analysis incorporates extra measurements, i.e. the particle size distribution at every height.

3.5 Conclusions

The entrainment from a bed of coke particles was investigated extensively. Different correlations were used and shown that are not reliable in predicting entrainment-related parameters. As a result, experimental data are in demand. There are few models which one can use to fit the experimental data into to get the parameters needed in the design stage. The best results however, came from the model proposed by Baron et al. 1988b which takes into account of the cluster flux. With only a few measurements in the freeboard of the fluidized bed, the results from this model can predict the flux of ejected particles from the bed surface more accurately. Also, this model provides a better understanding of the disengagement process and can well predict the TDH. Moreover, using this model, one can predict the particle flux any height as well as above the TDH which provides enough information for an engineer at the design stage.

3.6 References

Amitin, A. V., Martyushin, I.G., Gurevich, D.A., 1968. Dusting in the space above the bed in converters with a fluidized catalyst bed. Chem. Technol. Fuels Oils 4, 181–184. doi:10.1007/BF00718533

Baron, T., Briens, C.L., Bergougnou, M.A., 1988a. Measurement of the Flux of Clusters Ejected from a Fluidized Bed. Powder Technol. 55, 115–125.

Baron, T., Briens, C.L., Bergougnou, M.A., 1988b. Study of the transport disengaging height. Can. J. Chem. Eng. 66, 749–760. doi:10.1002/cjce.5450660508

Benoni, D., Briens, C.L., Baron, T., Duchesne, E., Knowlton, T.M., 1994. Procedure to determine particle agglomeration in a fluidized bed and its effect on entrainment. Powder Technol. 78, 33–42. doi:10.1016/0032-5910(93)02780-E

Berruti, F., Chaouki, J., Godfroy, L., Pugsley, T.S., Patience, G.S., 1995. Hydrodynamics of Circulating Fluidized Bed Risers : A Review. Can. J. Chem. Eng. 73, 579–602. doi:10.1002/cjce.5450730502

Briens, C.L., 2015. Advanced Particles and Fluidization Technologie Course notes. University of Western Ontario.

Briens, C.L., 1991. Correlation for the direct calculation of the terminal velocity of spherical particles in newtonian and pseudoplastic (power-law) fluids. Powder Technol. 67, 87–91. doi:10.1016/0032-5910(91)80030-M

Briens, C.L., Baron, T., Bergougnou, M.A., 1988. Prediction of entrainment of particles from fluidized beds. Powder Technol. 54, 183–196.

Cahyadi, A., Neumayer, A.H., Hrenya, C.M., Cocco, R.A., Chew, J.W., 2015. Comparative study of Transport Disengaging Height (TDH) correlations in gas–solid fluidization. Powder Technol. 275, 220–238. doi:10.1016/j.powtec.2015.02.010

Cai, P., Jin, Y., Yu, Z.-Q., Wang, Z.-W., 1990. Mechanism of flow regime transition from bubbling to turbulent fluidization. AIChE J. 36, 955–956. doi:10.1002/aic.690360619

Chehbouni, A., Chaouki, J., GUY, C., KLVANA, D., 1994. Characterization of the flow transition between bubbling and turbulent fluidization. Ind. Eng. Chem. Res. 33, 1889–1896. doi:10.1021/ie00032a002

Chen, T.P., Saxena, S.C., 1978. No Title, in: Davidson, J.F., Keairns, D.L. (Eds.), Fluidization: Proceedings of the Second Engineering Foundation Conference. Cambridge University Press, Cambridge University Press, London, p. 151.

Chew, J.W., Cahyadi, A., Hrenya, C.M., Karri, R., Cocco, R.A., 2015. Review of entrainment correlations in gas-solid fluidization. Chem. Eng. J. 260, 152–171. doi:10.1016/j.cej.2014.08.086

Cocco, R., Shaffer, F., Hays, R., Reddy Karri, S.B., Knowlton, T., 2010. Particle clusters in and above fluidized beds. Powder Technol. 203, 3–11. doi:10.1016/j.powtec.2010.03.023

Gugnoni, R.J., Zenz, F.A., 1980. Particle Entrainment from Bubbling Fluidized Beds. Plenum Press. New York.

Hazlett, J.D., 1990. Entrainment From Gas-solid Fluidized Beds (volumes I And II). PhD Thesis. Western University. London, Canada.

Horio, M., Taki, A., Hsieh, V.S., Muchi, I., 1980. Elutriation and particle transport through the freeboard of a gas–solid fluidized bed, in: Matsen, J.R.G. and J.M. (Ed.), Fluidization. Plenum Press, pp. 509–518.

Kunii, D., Levenspiel, O., 1991. Fluidization Engineering, Fluidization Engineering. Elsevier. doi:10.1016/B978-0-08-050664-7.50001-9

Kunii, D., Levenspiel, O., 1977. No Title, in: Fluidization Engineering. Kreiger Publishing Co., New York.

Large, J.F., Martinie, Y., Bergougnou, M.A., 1976. Interpretive model for entrainment in a large gas-fluidized bed. J. Powders Bulk Solids Technol.

Lim, K.., Zhu, J.., Grace, J.., 1995. Hydrodynamics of gas-solid fluidization. Int. J. Multiph. Flow 21, 141–193. doi:10.1016/0301-9322(95)00038-Y

Pemberton, S.T., Davidson, J.F., 1986a. Elutriation from fluidized beds-I. Particle ejection from the dense phase into the freeboard. Chem. Eng. Sci. 41, 243–251.

Pemberton, S.T., Davidson, J.F., 1986. Elutriation from Fluidized Beds I. particl Ejection from the Dense Phase into the Freeboard. Chem. Eng. Sci. 41, 2981–2987. doi:10.1016/0009-2509(86)87005-1

Pemberton, S.T., Davidson, J.F., 1986b. Elutriation from fluidized beds—II. Disengagement of particles from gas in the freeboard. Chem. Eng. Sci. 41, 253–262. doi:10.1016/0009-2509(86)87006-3

Pfeiffer, R.W., Borey, D.S., Jahnig, C.E., 1959. No Title. 2,881,130.

Rhodes, M., 1996. What is turbulent fluidization? Powder Technol. 88, 3–14. doi:10.1016/0032-5910(96)03093-8

Saxena, S.C., Mathur, A., 1989. A model for the projection of solid particles from the surface of a gas-fluidized bed. Chem. Eng. Sci. 44, 774–777. doi:10.1016/0009-2509(89)85052-3

Saxena, S.C., Mathur, A., 1984. On the origin of solids projected from the surface of a gas-fluidized bed. Chem. Eng. Sci. 39, 917–918.

Wen, C.Y., Chen, L.H., 1982. Fluidized bed freeboard phenomena: Entrainment and elutriation. AIChE J. 28, 117–128. doi:10.1002/aic.690280117

Yerushalmi, J., Cankurt, N.T., 1979. Further studies of the regimes of fluidization. Powder Technol. 24, 187–205. doi:10.1016/0032-5910(79)87036-9

Yoon, Y.S., Kim, S.D., Park, W.H., 1986. Entrainment of coal particles in a gas fluidized bed. Korean J. Chem. Eng. 3, 121–125. doi:10.1007/BF02705023

Zenz, F.A., 1983. Particulate Solids: The Third Fluid Phase in Chemical Engineering. Chem. Eng 90, 61–67.

Zenz, F.A., Weil, N.A., 1958. A theoretical-empirical approach to the mechanism of particle entrainment from fluidized beds. AIChE J. 4, 472–479. doi:10.1002/aic.690040417

Zhu, H., Zhu, J., 2008. New investigation in regime transition from bubbling to turbulent fluidization. Can. J. Chem. Eng. 86, 553–562. doi:10.1002/cjce.20059

Chapter 4

4 Entrainment from the fluidized bed with wet material

4.1 Introduction

As mentioned in the previous chapters, during the Fluid Coking process, bitumen or heavy oil is sprayed with atomization steam into a fluidized bed of hot coke particles. The bitumen undergoes thermal cracking and is converted into gasses, condensable vapors, and solid coke, which deposits on the coke particles. The vapors produced are separated from the coke in the stripping section at the bottom of the vessel through steam injection. These vapors are rising through the vessel and result in entrainment of coke particles. Fine coke particles from the freeboard region enter the cyclone and are separated from the vapors by means of centrifugal forces in the cyclone. In an ideal manner, these solids entering the cyclone should be dry so that the fouling of the cyclone be minimized. However, during the coking process, the wet agglomerates are ejected to the freeboard. The flux of these particles can affect the flux of fines entrained above the Transport Disengaging Height (TDH). The entrainment of fine particles in the Coker freeboard contributes to the fouling of the Coker cyclones which can lead to the premature shut-down of Fluid Cokers. It is believed that fouling is greatly accelerated when wet particles enter the cyclones.

The entrainment from a fluidized bed containing relatively low to high liquid loading has not been well studied. The main objective of this chapter is to determine how bed wetness affects entrainment, by measuring the flux and size distribution of the entrained particles at various heights for different levels of bed wetness, and comparing to the results obtained for a dry bed, which have been reviewed in the previous chapter.

McDougall et al. (2004) measured the entrainment from a bed of coke particles in a bubbling regime for various liquid (1-propanol) loadings. They observed that the total flux of entrained particles decreased with increasing liquid content up to a point. They attributed this reduction to the decrease in the amount of free fine particles resulting from the adhesion of fine particles to other fine particles and larger particles in wet beds. This was observed for bed wetnesses below about 1 wt %.

When the wetness was increased beyond the 1 wt %., McDougall et al. (2004) observed an increase in the total flux. They related this to the appearance of larger bubbles as the bed fluidization changed. As bubbles become larger, clusters are projected higher. They stated that at first nothing happens as the TDH increases but remains shorter than the overall freeboard height. Once the TDH extends beyond the freeboard height, the proportion of clusters in the solids entrained out of the column grows and the total entrained flux increases. As the bed wetness is increased further, the bubbles become so large that slugging occurs, the bubble growth is restricted by the column diameter and the TDH stops increasing. However, by looking at their data, the above explanation may work for the distances close to the TDH and far from the bed surface (above 2 meter), but falls short in explaining why the total entrained flux decreases for distances close to the bed (below 1.5 meter) as these heights were already well below the TDH.

The mechanisms by which the particles are ejected from the fluidized bed are dependent on the bed characteristics, in particular, bubble properties at the bed surface as it is well accepted that the bursting of bubbles at the bed surface causes entrainment. Although the presence of liquid will generally have an adverse effect on fluidization, there are often strong incentives in operating with high liquid loadings. For example, in the Fluid Coking process, operating at lower reactor temperature increases yield and reduces emissions but increases the bed wetness, which may lead to local zones of poor mixing and a reduction in fluidization quality, compromising reactor performance and stability. The introduction of liquid in a fluidized bed results in the formation of wet agglomerates. A high local concentration of liquid in the fluidized bed may result in particles coated with liquid that stick together, which in turn causes poor fluidization, a condition called "bogging", and, eventually defluidization (Hamidi, 2015; McDougall et al., 2004). Degradation of fluidization quality has been attributed to a variety of fluidized bed phenomena such as particle cohesivity, particle agglomeration, reduced bubbling, an increase in minimum fluidization velocity and channeling (Hamidi, 2015; McLaughlin and Rhodes, 2001).

According to Hamidi (2015), changes in fluidization behavior caused by liquids can be classified into two categories:

1. Adding liquid to Geldart group B particles may result in the ratio of inter-particle forces to drag force to increase and may cause a transition to group A and group C behavior that finally can result in bogging or defluidization (Hamidi, 2015; McLaughlin and Rhodes, 2001; Seville and Clift, 1984).

2. The agglomeration of fluidized particles has been proposed as another mechanism that can lead to bogging and defluidization (Bartels et al., 2010; van Ommen, n.d.) In an agglomerating fluidized bed, the increase in effective particle size results in a higher minimum fluidization velocity that in turn degrades the fluidization.

Regarding the change in minimum fluidization velocity, Seville and Clift, (1984) noted that very light liquid loading causes a slight reduction in the minimum fluidization velocity, U_{mf}. This was observed for Group A materials by D'Amore et al. (1979) as well. However, they found that at higher liquid loading, the minimum fluidization velocity increases markedly but also show that other phenomena occur. At comparatively light loadings, the bed greatly expands beyond minimum fluidization and bubbling commences at higher velocity; this is the behavior characteristic of Group A. At higher loadings, where the bed lifts as a plug or channeling occurs, the behavior is clearly Group C.

As stated above, the changes in fluidization behavior caused by liquids was investigated, and previous studies have shown that the bubble behavior is greatly affected by the bed cohesivity but a clear pathway to predict the behaviour of a bubble in the presence of liquid is not provided. This results from the fact that powders, even the powders of the same group, have different characteristics particularly inter-particle forces which may be reduced or increased in the presence of low to high moisture content causing different behaviours to be observed.

In a study with coke particles in the presence of Voltesso™ oil as a background liquid, Hamidi (2015) observed that as liquid is added to the fluidized bed, the average bubble velocity first decreases slightly with increasing the Voltesso™ oil up to 0.2 wt%. He attributed this to the increase in the cohesivity of particles which result in an increase in the effective particle diameter and thus increasing the minimum fluidization velocity which explains the decrease in the bubble velocity. When the Voltesso™ oil fraction was increased past 0.2 wt%, the bubble velocity started increasing sharply with increasing oil fraction. He explained this by the appearance of channeling: when channeling begins at some locations of the fluidized bed, the bubble rise velocity increases due to limited routes for the fluidization gas and, eventually, most of the gas flows through channels, which should change the entrainment mechanism.

The current study, therefore, focuses on three Voltesso™ oil fractions, 0.1, 0.2 and 0.3 wt%, to investigate all the fluidization regimes observed by Hamidi (2015).

4.2 Experimental setup and procedure

The experimental setup, as well as the operating and measurement procedures, have been extensively described in Chapter 2 and Chapter 3.

The only change with previous chapters is that Voltesso™ oil was added to the same fluid coke used in previous chapters, with a Sauter Mean Diameter (SMD) of 133 μm and a particle density of 1470 kg/m^3. Voltesso™ oil was selected as it does not vaporize and simulates, at room temperature, the properties of bitumen in Fluid Coking. Voltesso™ oil at room temperature has the viscosity of 0.007 Pa.s and density of 864 kg/m^3 while bitumen at 300°C has the viscosity of 0.005 Pa.s and density of 922 kg/m^3. Voltesso™ has a negligible vapor pressure at room temperature and can be used to provide a constant liquid background during each experiment. Voltesso™ was mechanically mixed with particles to ensure uniform coating of all the particles and to prevent the formation of coke-Voltesso™ agglomerates (Hamidi, 2015).

A 0.19 m I.D column made of Plexiglas was designed and modified as the new fluidized bed. The total column height was 2.61 meter, which was later lengthened to 3.7 m by adding an extension section with the same I.D as the original column. For all the experiments, 12 kg of solids were charged to the column and the bed height as well as the bed mass was measured by monitoring the pressure gradient along the column. Compressed air with near zero percent humidity was introduced to the column through a sparger as the fluidizing fluid.

The column has four exhaust lines, which are located on the very top section of the column at every 90°, enabling us with to benefit from isokinetic sampling probes with a novel design. All the entrained solids are collected by a cyclone, which is connected to the four exhausts, and are returned to the bed through a dipleg. Sampling from the dipleg was performed in some of the preliminary experiments.

The column lid was designed and constructed with eleven ports, so the pseudo-isokinetic sampling measurements were conducted from the top of the column. Ports have been set up at different radial and angular positions so that none of the probes inserted into these ports interfere with each other.

Five new pseudo-isokinetic sampling systems were developed and tested to conduct entrainment-related measurements at different heights. Each system is only capable of measuring the upflux, and it mainly consists of:

1-The sampling probe which is inserted vertically into the column through the ports available on the column lid, and whose vertical location can be easily adjusted as needed. It is made of a plastic conical shape tip which is connected to a metal tube.

2- The collection vessel which consists of a removable jar in which the solids are accumulated and a filter which captures fine particles.

3- The flow control and monitoring instrument which consists of a flowmeter with a control valve.

4- The ejector which provide enough suction air at the probe tip to equalize the air velocity at the probe tip to the one in the freeboard.

Previous studies have shown that pseudo-isokinetic sampling provides accurate results for the measurement of particles entrained from fluidized beds (Hazlett, 1990). Also, this is verified in Chapter 2 through the preliminary experiments.

4.3 Results and discussion

The experiments were conducted with three different gas velocities and four different liquid contents (0 to 0.3 wt.%) which were measured as a mass fraction of the solids in the bed.

The results are summarized in graphs below and detailed data are available in Appendix C. For the sake of brevity, the results will be discussed for each gas velocity individually.

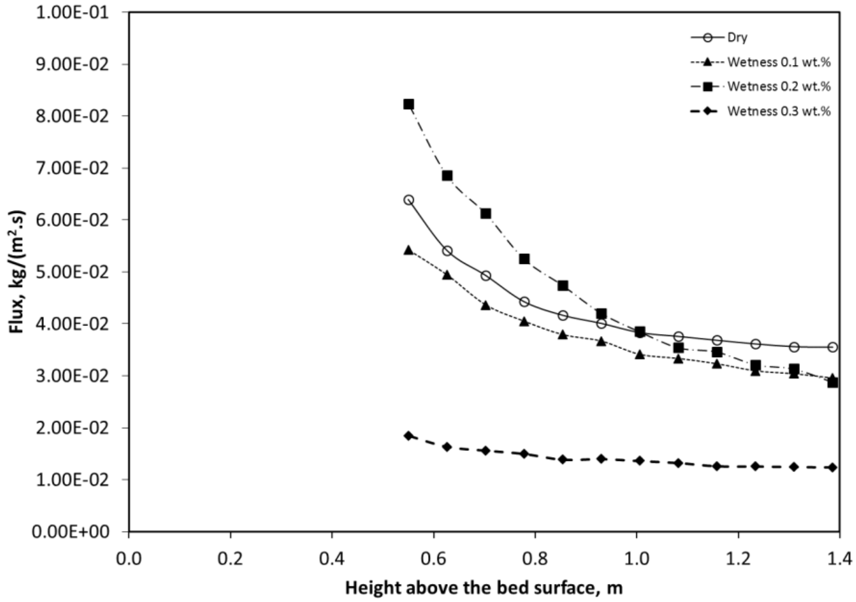

Figure 4-1. Effect of liquid content in the total flux measured, $V_g = 0.3$ m/s

From Figure 4-1, it can be seen, for a superficial gas velocity of 0.3 m/s that the flux at heights far from the bed surface decreases with increasing liquid content. At this velocity, the measurements reported in Figure 4-1 were performed at heights that can be assumed to be above the TDH or just below the TDH, meaning that the effect of bed wetness can be attributed mainly to the agglomeration of fines with other bed particles. The other interesting observation is that at bed wetness of 0.2 wt. %, and at heights closer to bed surface, the total flux of entrained particles is higher than one for the dry bed. This was shown in a Figure 4-2 clearly.

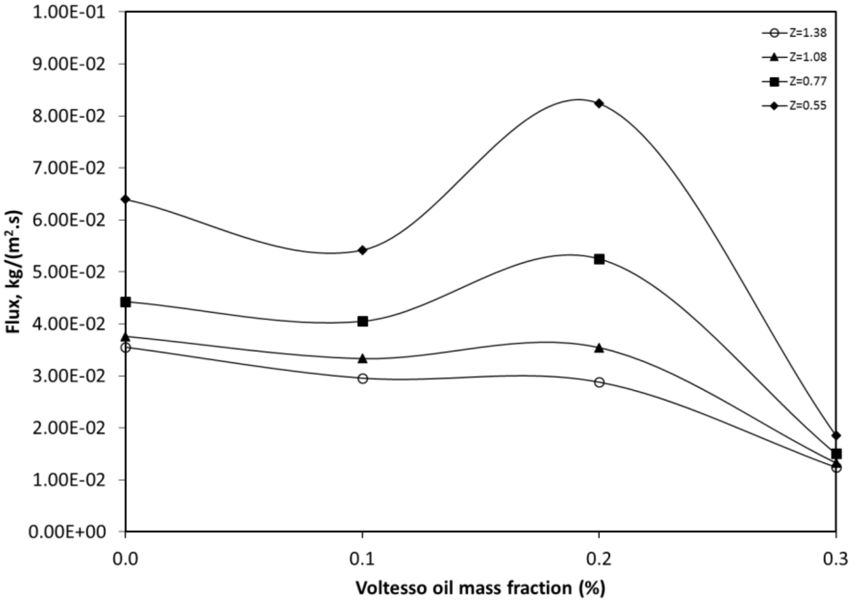

Figure 4-2. Flux of entrained solids at four different heights, $V_g = 0.3$ m/s

To further investigate this, the cluster analysis performed in section 3.4.5 has been applied to the data and results are summarized in Table 4-1.

Table 4-1. Parameters from cluster analysis for $V_g = 0.3$ m/s

Parameters	**Values at V_g = 0.3 m/s, Dry**	**Values at V_g = 0.3 m/s, 0.1 wt.% wetness**	**Values at V_g = 0.3 m/s, 0.2 wt.% wetness**	**Values at V_g = 0.3 m/s, 0.3wt.% wetness**
A_c Average	4.58	3.28	2.93	5.60
F_0	0.29	0.15	0.27	0.09
F_0 Lower 95%	0.24	0.12	0.22	0.07
F_0 Upper 95%	0.37	0.17	0.31	0.10
Relative margin of error on F_0	22%	16%	17%	19%

The relative margin of error is the percentage of deviation possible around the point estimate at a specific confidence interval. Here, the point estimate is F_0 and deviation around this estimate is calculated at a 95 percent confidence interval. The relative margin of error is calculated by dividing the absolute margin of error (“radius" or half the width of a confidence interval) by the point estimate.

First, by increasing the wetness from 0 to 0.1 wt.%, the larger agglomerates appear, the bed becomes less fluid and larger bubbles form. Larger bubble have higher velocity at the bed surface, ejecting clusters higher. According to Baron et al. (1988), the largest clusters will reach the highest level in the freeboard before falling back to the bed surface since they are so large that the drag force acting on them is negligible when compared to gravity. Thus TDH is related to the ejection velocity which itself is related to the bubble velocity at the bed surface, meaning that a higher velocity of bubbles at the bed surface should result in a higher TDH. In the previous chapter it was shown that the TDH can be calculated using:

$$TDH_3 = \frac{ln100}{A_c} = \frac{4.6}{A_c} \tag{4-1}$$

Based on the above argument, one can relate the A_c to the maximum height reached by the larger cluster, meaning that lower values of A_c originate from bubbles with a higher velocity. From the Table 4-1 it can be seen that the A_c has been decreased suggesting appearance of larger bubbles, which has higher velocity at the bed surface.

According to Kunii and Levenspiel (1991) the bubble velocity is a function of the (V_g-U_{mf}) and as well as of $d_b^{0.5}$. Meanwhile, according to Darton (1979) the d_b is a function of $(V_g-U_{mf})^{0.4}$. This suggest that the increase in the liquid content resulted in an increase in (V_g-U_{mf}). While V_g was constant, U_{mf} was decreased. This was observed by Seville and Clift (1984) and D’Amore et al. (1979) and the formation of larger bubbles was concluded by McDougall et al.(2004). The above findings contradicts the findings by Hamidi, (2015) who observed a lower bubble velocity at the presence of low liquid content.

The other challenging but interesting point is that at bed wetness of 0.1 wt.% , the flux of solids ejected from the bed surface is reduced by half; while one expect that the larger bubbles to eject larger amount of particles to the freeboard as they have larger bubble wakes. As the ejection mechanism of particles to the freeboard is still very controversial, and it was shown that none of the models or correlation are able to predict this properly, it is very hard to comment about this observation. However, one possible explanation can be the change in the dominant mechanism for ejection of particles to the freeboard. The other explanation is that even though the larger bubbles eject larger particles at a time, the frequency of these bubbles also matters. It is possible that in the presence of liquid, the larger bubbles with higher velocities form but at the frequencies lower comparing to for the dry bed.

As the liquid content increase to 0.2 wt. % larger bubbles form and result in the ejection of more particles to the freeboard. It can be also concluded that the minimum fluidization velocity was decreased further, resulting in the excess gas (V_g-U_{mf}) to form larger bubbles. The powder still behaves as Group A powder.

Beyond the bed wetness of 0.2 wt.%, the inter-particle or inter-agglomerate forces increases and the powder behaves as Group C powder. U_{mf} was increased markedly, resulting in an obvious reduction in the bubble size. It is expected that by increasing the bed wetness beyond this point, eventually channeling occurs which will result in defluidization of bed. No bubbles will appear and thus ejection from the bed surface stops.

TDH was calculated using three equations mentioned in Chapter 4.

Table 4-2. TDH calculated using three different equations

	V_g = 0.3 m/s, Dry	**V_g = 0.3 m/s, 0.1 wt.% wetness**	**V_g = 0.3 m/s, 0.2 wt.% wetness**	**V_g = 0.3 m/s, 0.3 wt.% wetness**
TDH_1, m	1.74	2.22	2.68	1.21
TDH_2, m	1.46	1.91	2.39	1.19
TDH_3, m	1.00	1.40	1.57	0.82
Average of TDH_1 and TDH_3	1.37	1.81	2.12	1.02

It is clear that by increasing the bed wetness, the TDH starts increasing. This increase continues until the bed wetness of 0.2 wt.% beyond which the TDH starts decreasing.

The entrainment results from the wet bed at higher velocities has been also investigated.

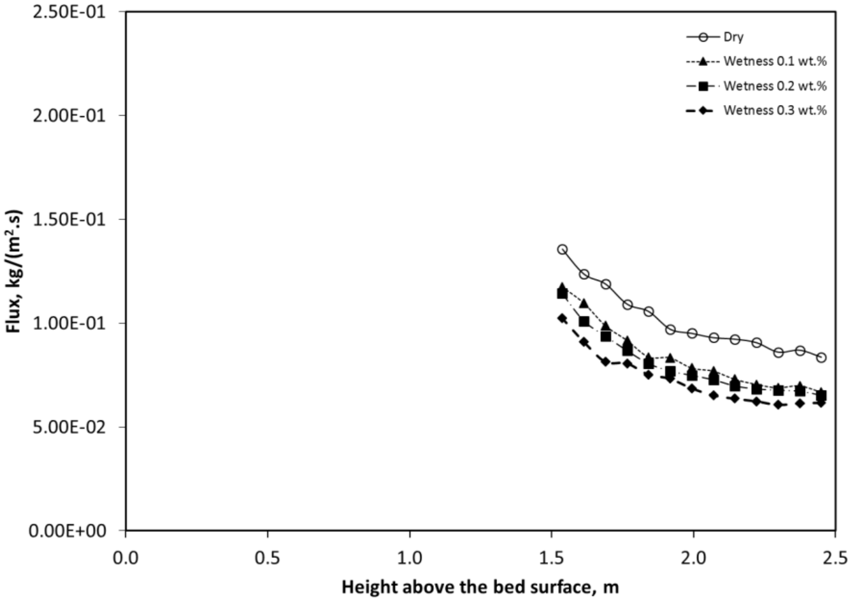

Figure 4-3. Effect of liquid content in the total flux measured, $V_g = 0.6$ m/s

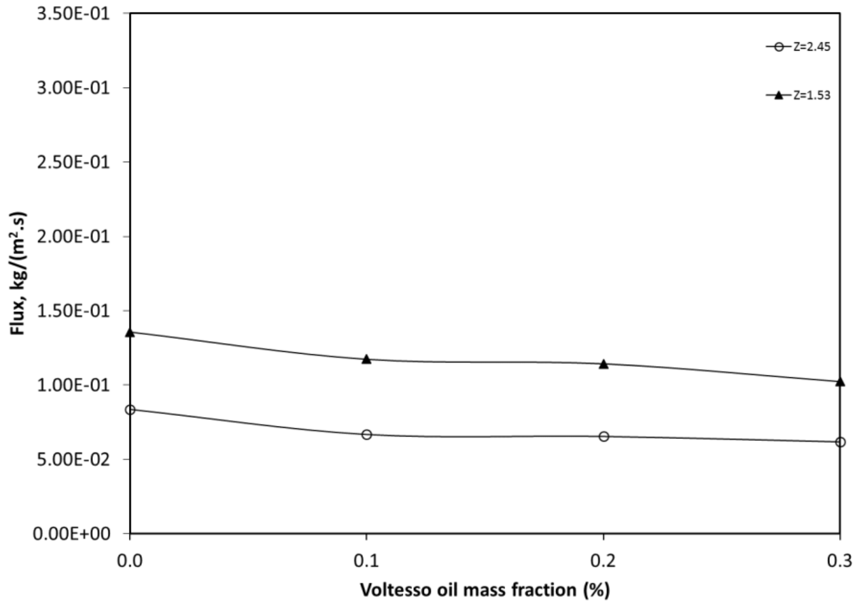

Figure 4-4. Flux of entrained solids at two different heights, $V_g = 0.6$ m/s

Table 4-3. Parameters from cluster analysis for $V_g = 0.6$ m/s

Parameters	**Values at V_g = 0.6 m/s, Dry**	**Values at V_g = 0.6 m/s, 0.1 wt.% wetness**	**Values at V_g = 0.6 m/s, 0.2 wt.% wetness**	**Values at V_g = 0.6 m/s, 0.3 wt.% wetness**
A_c Average	3.99	3.94	3.96	4.07
F_0	16.85	17.27	17.36	17.66
F_0 Lower 95%	13.66	13.09	13.13	11.99
F_0 Upper 95%	20.78	22.79	22.92	26.01
Relative margin of error on F_0	21%	28%	28%	39%

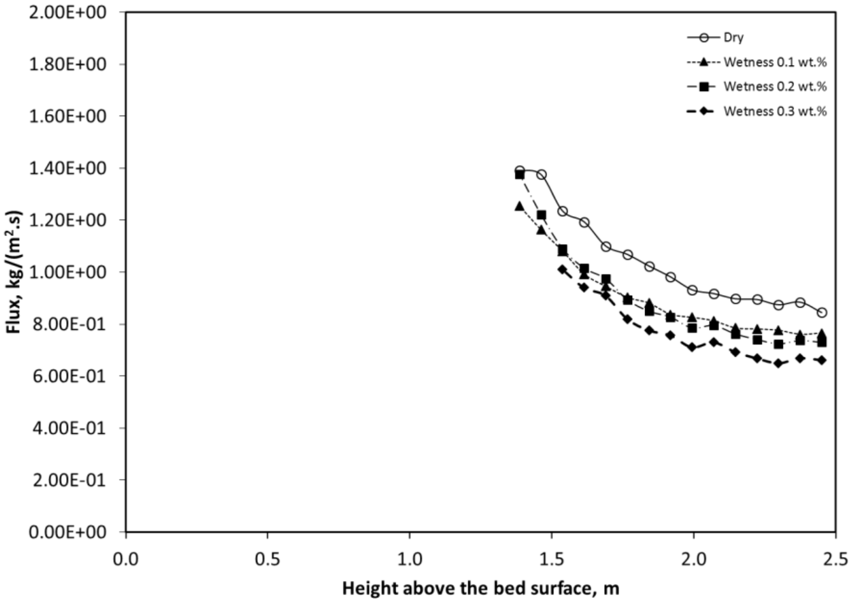

Figure 4-5. Effect of liquid content in the total flux measured, V_g = 0.9 m/s

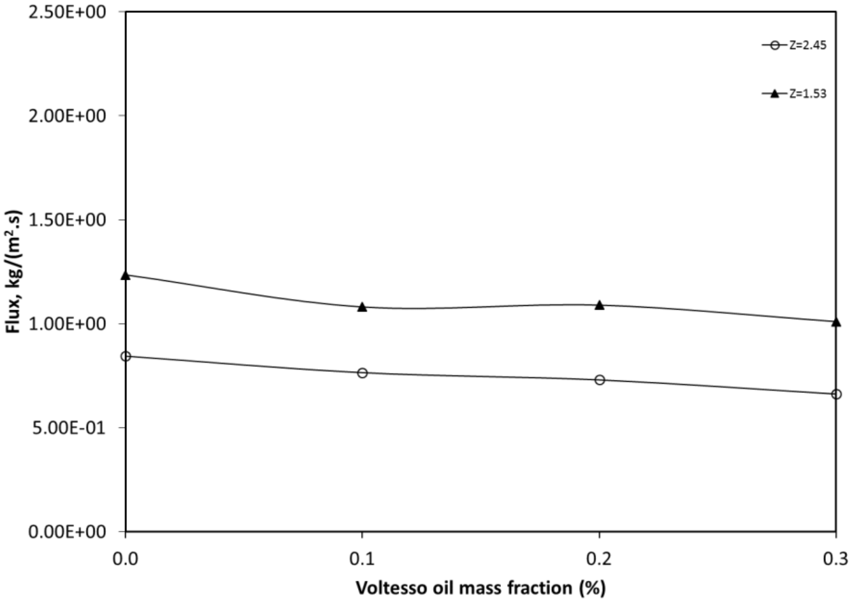

Figure 4-6. Flux of entrained solids at two different heights, V_g = 0.9 m/s

Table 4-4. Parameters from cluster analysis for V_g = 0.9 m/s

Parameters	**Values at V_g = 0.9 m/s, Dry**	**Values at V_g = 0.9 m/s, 0.1 wt.% wetness**	**Values at V_g = 0.9 m/s, 0.2 wt.% wetness**	**Values at V_g = 0.9 m/s, 0.3 wt.% wetness**
A_c Average	3.27	3.30	3.22	3.23
F_0	46.89	48.92	47.84	46.16
F_0 Lower 95%	37.00	36.78	35.12	29.89
F_0 Upper 95%	59.44	65.09	65.18	71.30
Relative margin of error on F_0	24%	29%	31%	45%

From Figure 4-3 it can be seen that the total solid entrainment decreased with increasing bed wetness. This is due to agglomeration of fines and their adherence to larger particles. However, comparing Figure 4-2 and Figure 4-4 shows that the reduction in the fines at height far from the bed surface is less at gas velocity 0.6 m/s relative to 0.3 m/s. This can be due to the fact that that at higher velocity, larger particles can be entrained above TDH, and these particles are more resistant to form agglomerates. The other explanation might be that at high velocity, due to the agitation in the bed, larger agglomerates will break down more easily rather than smaller ones.

By looking at the Table 4-3. Parameters from cluster analysis for V_g = 0.6 m/s it can be seen that the overall outcome of increasing liquid content was a slight increase in the flux of solids ejected from the fluidized bed to the freeboard. This is probably due to the transition of powder behavior to group A and formation of agglomerates. Also, it can be concluded that the dominant mechanism for ejecting the particles did not change. If one relates the ejection from the bed surface to the bubble wakes, might be able to conclude that at this velocity, the bubbles will reach the maximum size at the surface of the bed, thus changes in powder behavior due to increase of liquid content cannot affect size of bubbles. In other words, the velocity is so high that in the presence or absence of liquid, the bubble can reach their maximum size. The change in the bed behavior only changes the amount of excess gas (V_g-U_{mf}) which in turns result in change in the frequency of bubbles rising through the bed. Also the value of A_c which can be related to the bubble size did not change greatly. Thus one can conclude increasing liquid content up to 0.3 wt. % does not change the bed hydrodynamics and bubbles behavior significantly. This is because at this velocity, the bed operates at a velocity far from minimum fluidization velocity, thus small changes in U_{mf} can hardly affect the overall bed hydrodynamics.

By looking at the Figure 4-5, Figure 4-6 and Table 4-4 which shows the results for gas velocity of 0.9 m/s, it can be seen that the bed shows a similar behavior when the gas velocity is 0.6 m/s in the presence of liquid. Thus the recent explanation can be used to justify the behavior of powder at this gas velocity.

4.4 Conclusions

The entrainment from a bed of coke particles was investigated in the absence and presence of non-volatile liquid. The cluster analysis was performed to provide a deeper understanding of the phenomena. At all velocities, the total entrainment was reduced by increasing the liquid content, particularly at heights far from the bed surface. This was due to agglomeration of fines and their adherence to the larger particles.

At low gas velocity, which was a bubbling regime, increase in the liquid content first resulted in a decrease in the flux of solids ejected to the bed surface. This was explained by presence of larger but less frequent bubbles initiated from transition to Group A and decrease in the minimum fluidization velocity. By further increasing the liquid, the flux at the bed surface increased due to formation of larger bubbles suggesting a further decrease in the minimum fluidization velocity. By further increasing the liquid content, the inter-particle forces became dominant and the powder behaved as Group C, resulting in a significant increase in the U_{mf} and causing formation of small bubbles and significant reduction in the flux of ejected solids at the bed surface.

At higher velocities which the bed operates in the turbulent regime, the increase in the liquid content did not change the powder behavior and bed hydrodynamics significantly, thus no observable changes were observed in the flux of solids ejected from the bed surface or the value of TDH. To better understand the effect of liquid content in these velocities, one should increase the liquid content beyond the 0.3 wt.% which was the maximum value in our experiments, ensuring that changes in the U_{mf} due to the presence of liquid is not negligible comparing to the gas superficial velocity.

4.5 References

Baron, T., Briens, C.L., Bergougnou, M.A., 1988. Measurement of the Flux of Clusters Ejected from a Fluidized Bed. Powder Technol. 55, 115–125.

Bartels, M., Nijenhuis, J., Kapteijn, F., van Ommen, J.R., 2010. Case studies for selective agglomeration detection in fluidized beds: Application of a new screening methodology. Powder Technol. 203, 148–166. doi:10.1016/j.powtec.2010.05.003

D'Amore, M., Donsì, G., Massimilla, L., 1979. The influence of bed moisture on fluidization characteristics of fine powders. Powder Technol. 23, 253–259. doi:10.1016/0032-5910(79)87015-1

Darton, R.C., 1979. A Bubble Growth Theory of Fluidized Bed Reactors. Trans IChemE. 57, 134–138.

Hamidi, M., 2015. Development And Study Of Measurement Methods For Jets And Bogging In A Fluidized Bed. PhD Thesis. Western University. London, Canada.

Hazlett, J.D., 1990. Entrainment From Gas-solid Fluidized Beds (volumes I And II). PhD Thesis. Western University. London, Canada.

Kunii, D., Levenspiel, O., 1991. Fluidization Engineering, Fluidization Engineering. Elsevier. doi:10.1016/B978-0-08-050664-7.50001-9

McDougall, S.L., Saberian, M., Briens, C., Berruti, F., Chan, E.W., 2004. Characterization of Fluidization Quality in Fluidized Beds of Wet Particles. Int. J. Chem. React. Eng. 2, A26.

McLaughlin, L.J., Rhodes, M.J., 2001. Prediction of fluidized bed behaviour in the presence of liquid bridges. Powder Technol. 114, 213–223. doi:10.1016/S0032-5910(00)00325-9

Seville, J.P.K., Clift, R., 1984. The effect of thin liquid layers on fluidization characteristics. Powder Technol. 37, 117–129.

Van Ommen, J.R., n.d. Early warning of agglomeration in fluidized beds by attractor comparison. AIChE J. 46, 2183 – 2197.

Chapter 5

The objective of this chapter is to develop a radioactive tracer method for the measurement of clusters entrainment in both dry and wet fluidized beds. Two kinds of information are required:

1) The motion of ejected clusters in the freeboard.

2) The decrease in concentration of the clusters with height in the freeboard.

5 Computer Aided Radioactive Particle Tracking

5.1 Historical Background

Radioactive Particle Tracking known as RPT is a non-intrusive method for tracking a single particle in a vessel or column without disrupting the flow inside the vessel (Shehata et al., 2007). The concept of this technique is not new by its nature, but it has gone through several refinements and improvements. In 1965, Kondukov et al. came up with this idea but due to lack of proper data acquisition, they were not able to obtain quantitative results. Lin et al. (1985) developed a novel computer aided radioactive particle tracking facility to study solids motion in fluidized beds. They were relatively successful in their objectives and were able to observe a change in the direction of solids motion with an increase in gas velocity. Moslemian et al. (1992) then introduced digital pulse counters, which resulted in faster data sampling. Afterward various scientists contributed to improving different aspects of the RPT method. Also, several applications have been found for this technique.

5.2 General working principal

CARPT is a technique for tracking single radioactive tracer by detecting the intensity distribution of emitted γ-rays. The γ-rays are detected using an array of NaI scintillation detectors strategically placed externally around the controlled volume. (Rados, 2003)

During the CARPT experiment, a single radioactive tracer whose physical characteristics matches the material in the bed or vessel is introduced into the controlled volume. The tracer particle represents the solids or liquid in the bed and to ensure proper tracking of the solids it is of high importance to have very similar physical attributes as the materials, in the controlled volume. This tracer particle moves along with the bed materials, and its position is determined by a set of scintillation detectors that monitor the γ-ray emissions from the tracer. The radiation intensity recorded by each detector is a function of the distance of the tracer to the detector. To obtain the position of the tracer from the recorded radiation intensities, an in situ calibration should first be performed, by placing the tracer at various known locations and registering the radiation intensity recorded by each detector. Using the information acquired, a calibration curve is developed for each detector to relate the intensity registered by the detector to the distance between the tracer and the virtual center of the detector surface. The calibration curve is established by curve fitting of the raw data, and the fitted curve can have different shape and order. For example, Degaleesan (1997) fitted the calibration data to a cubic spline while Larachi et al. (1997) fitted the data to a polynomial equation of various orders.

Once the distance of the particle from each detector is evaluated, a weighted regression scheme is used to estimate the particle position at each time. Thereby, in a dynamic experiment, a set of instantaneous positions is obtained that gives the position of the tracer at each sampling time.

The fast processing time and the simplicity of the mathematics are the primary advantages of the CARPT method. The main disadvantages are that it requires a substantial calibration effort and that the model does not take into account the angle between the tracer and a horizontal plane through the virtual center of the scintillation detector.

5.3 Current CARPT Set-up

A complete RPT system consists of (Sanchez Careaga, 2013):

- A single radioactive tracer-particle emitting γ-rays and physically and aerodynamically similar to what is being studied (i.e. clusters, agglomerates, etc.).
- Several scintillation detectors to sense the radiation emitted by the tracer-particle.
- One computer or computers to record, process, and analyze the data from each detector.

5.3.1 Selection and preparation of radioactive Tracer

When selecting the radioactive tracer, the following measures shall be considered:

Half-life: Which is defined as the time after which the activity of the radioactive source is halved naturally. The half-life of different radioisotopes varies from a few seconds to many years. This can be viewed from two perspectives:

On one hand, the half-life should not be too short to give the experimenter enough time to conduct an adequate number of experiments with a single tracer. Besides one should consider the time and money spent on tracer preparation, shipping of the activated source (the closest nuclear reactor was in McMaster Nuclear Reactor-Hamilton), the cost of the radiation, etc. A radioactive candidate with a long half-life allows for multiple uses reduces costs and saves time.

On the other hand, radioisotopes with very long half-life, are associated with more responsibilities and liabilities for the user for its protection handling and storing.

Gold has a half-life 2.697 days; based on the above argument the radioactive gold (^{198}Au) was preferred and it decays into stable isotope of mercury (^{198}Hg) which is very desirable for health concerns (Sanchez Careaga, 2013).γ-rays emission peak for Au^{198} is 412 KeV.

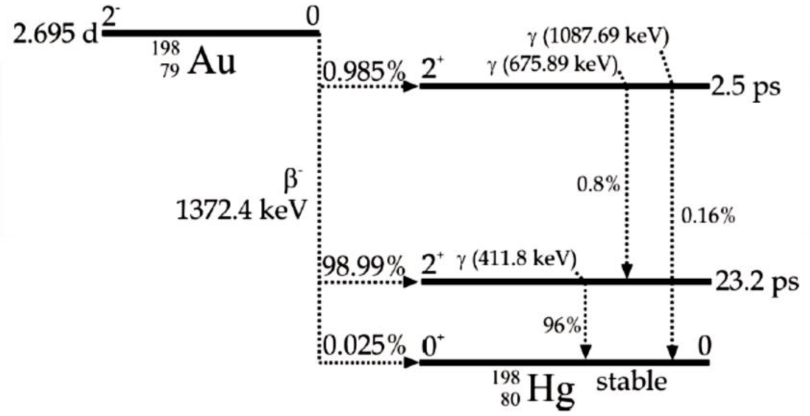

Figure 5-1. Decay scheme of the ^{198}Au nucleus (Konefal, 2011)

5.3.2 Preparing the tracer

In all the experiments, the original tracer which was primarily made by Sanchez Careaga at ICFAR by mixing gold powder and epoxy resins were used, and the preparation process can be found in Sanchez Careaga (2013).

To send the tracer to the nuclear reactor, a small piece of the gold-prepared agglomerate is removed and weight of the gold, based on the percentage of the gold in agglomerate, is calculated. The weight of the gold is necessary to be known as it defines the time of the radiation in the nuclear reactor. This time was calculated by the employees of McMaster Nuclear Reactor and only the final required activity was set by us. This activity was ranging from 300 to 500 μCi.

Also, before sending the tracer to the nuclear reactor, the tracer was submerged in a mixture of epoxy resin and a hardener and then removed to let it dry for one day. This further step is done to ensure the tracer will not break due to attrition or breakage and avoid health problems due to radioactive dust.

5.3.3 Hardware

Twelve NaI cylindrical scintillation detectors model 2M2/2 (Saint-Gobain Crystals, USA) were used to obtain the γ ray intensities. The size of the crystal in these detectors are 2"×2". NaI detectors are known to have a relatively low resolution, but are preferable in some applications due to their high efficiency and their operation at room temperature (unlike Germanium detectors which requires liquid Nitrogen to operate). The 0.2% thallium (TI) impurity (activator) in the crystal structure of NaI detector converts the energy absorbed in the crystal to light. Each of these detectors is equipped with an integrally mounted Photomultiplier Tube (PMT) which convert the light into an electrical signal and then amplifies that signal to a useful level.

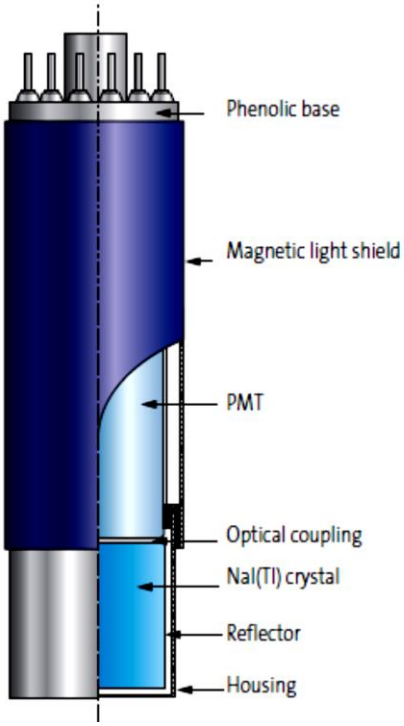

Figure 5-2. Scintillation detector (Saint-Gobain Crystals Inc.)

Each of these detectors is externally coupled with ORTEC digiBASE (Advance Measurement Technology, Inc., Ridge, TN) that combines a preamplifier with a powerful digital Multichannel Buffer (MCB) and special features for fine time-resolution measurements. This base is used for data acquisition and processing through CONNECTION-32 and MAESTRO®-32 programs.

Each detector communicates through a USB cable to one laptop (Client laptop). A USB hub (StarTech.com Ltd.) was placed between each detector and laptop to speed up the data transmission from the digiBASE to each client computer. The client computer collects the detectors signal every six milliseconds by using a program created on the LabWindows CVI (National Instruments, Austin, TX)) platform by Sanchez Careaga (2013). All the twelve laptops communicate through an Ethernet hub to a Server computer (Server PC) which has the responsibility of synchronizing the client laptops as well as timestamping the DAQ data. This ensures that all the detectors acquire data (through scanning the tracer) at the same time and that the time of the scanning is known.

5.3.4 Software

The program used for RPT in this study was originally developed by Sanchez Careaga in 2012. Details and explanation can be found in his work (Sanchez Careaga, 2013)

Maintaining the principal structure of the program, slight modification were done on the software by Sanchez Careaga in 2014: The original program handled four slave computers (one computer for three detectors) and the average sampling time was varying from 9 ms to 31 ms depending on the tracer radioactivity. In the modified software, each laptop handles one detector. Doing this, the sampling time was improved and dropped down to 7 ms for a strongly radioactive tracer and 6 ms for a weakly radioactive tracer.

The other modification was that the program uses the absolute counts to obtain the position of the tracer; while in the original program normalized counts (relative counts) were used to do so. Relative counts were calculated using the formula below:

$$C_{i,relative} = \frac{C_{i,absolute}}{\sum_{i=1}^{12} C_{i,absolute}} \qquad \textbf{5-1}$$

For analysis of the raw data acquired (Counts vs. time or position vs. time), new programs in MATLAB or MS Excel were developed; they will be described below.

5.3.5 Calibration

Basically, three effects affect the intensity of radiation received by a detector from the radioactive source:

1- Attenuation of the radiant flux (in W) due to radiation interaction with the medium.

2- Decrease with distance from the point source of the irradiance, or radiant flux received per unit area (in W/m^2) of a sphere whose center is at the point source.

3- Interaction of the detector with the irradiance, described with calibration constants in our experiments, as shown in section 5.3.6.

Attenuation of the radiant flux (in W) due to radiation interaction with the medium. For a given source strength, the radiant flux through a given medium, reduces exponentially with distance between the detector and the source as shown by the Beer–Lambert law. The exact and more complex function form of this relationship depends on many factors such as attenuation of gamma photons directly reaching the detector by the traversed medium, buildup of the photons caused by the interaction of primary photons with the medium causing the photons to get deflected from their original path, the solid angle between the particle and the detector, the efficiency of the detector, the column geometry etc. Due to the attenuation in the medium being passed over, the gas and solid holdup may need to be considered during the calibration (Degaleesan, 1997) when working with dense materials. Thus, to estimate the location of the tracer accurately, calibration is recommended under the given operating conditions. However, in our case, the effect of media being traversed is negligible based on the following argument.

For absorption of radiation in a series of different media, we have (generalized Beer–Lambert law):

$$\Phi_s = \Phi_0 \times \exp(-\sum_i \alpha_i \rho_i L_i) \tag{5-2}$$

In this equation, Φ_0 incident flux, Φ_s sub-incident flux, L_i absorber thickness, ρ_i absorber density and α_i is the mass absorption coefficient of the medium (Bartholomew and Casagrande, 1957).

Considering an in situ calibration, the gamma-rays shall pass through the coke (bed material), air and Plexiglas (column wall) media while during an ex situ (out of column) calibration only the air is present, and coke and Plexiglas wall are not present. As a result, the effect of attenuation in the air will be included in both in situ and ex situ calibrations, and there is no need to be further investigated.

Now, the effect of attenuation in the other two media will be examined separately. It should be noted that all the mass attenuation coefficients for carbon, air and Plexiglas (for gold as the radioactive source with γ-rays emission peak at 0.4 MeV) and other physical properties are obtained from National Institute of Standards and Technology:

In Plexiglas wall when the tracer is right in front of the detector:

$$\frac{\Phi_{s,1}}{\Phi_0} = \exp(-\alpha_1 \rho_1 L_1) = \exp\left(-1.031 \times 10^{-2}\ \left[\frac{m^2}{kg}\right] \times 1190\ [\frac{kg}{m^3}] \times 0.0064\ [m]\right)$$

$$= 0.92$$

In fluidized bed, consider that the tracer is located at the furthest position from the detector (L_2 = 2R):

$$\frac{\Phi_{s,2}}{\Phi_0} = \exp(-\alpha_2 \rho_2 (1-\varepsilon_s) L_2)$$

$$= \exp\left(-9.54 \times 10^{-3}\ \left[\frac{m^2}{kg}\right] \times 1470\ [\frac{kg}{m^3}] \times (1-\varepsilon_s) \times 0.1905\ [m]\right)$$

$$= \exp\big(-0.2635 \times (1-\varepsilon_s)\big)$$

In the above calculation, it was estimated that the coke has the same mass attenuation coefficient as carbon, as according to Furimsky (2000) coke is mostly made of carbon. The $\frac{\Phi_{s,2}}{\Phi_0}$ in a bed of coke is plotted as a function of the solid holdup (ε_s):

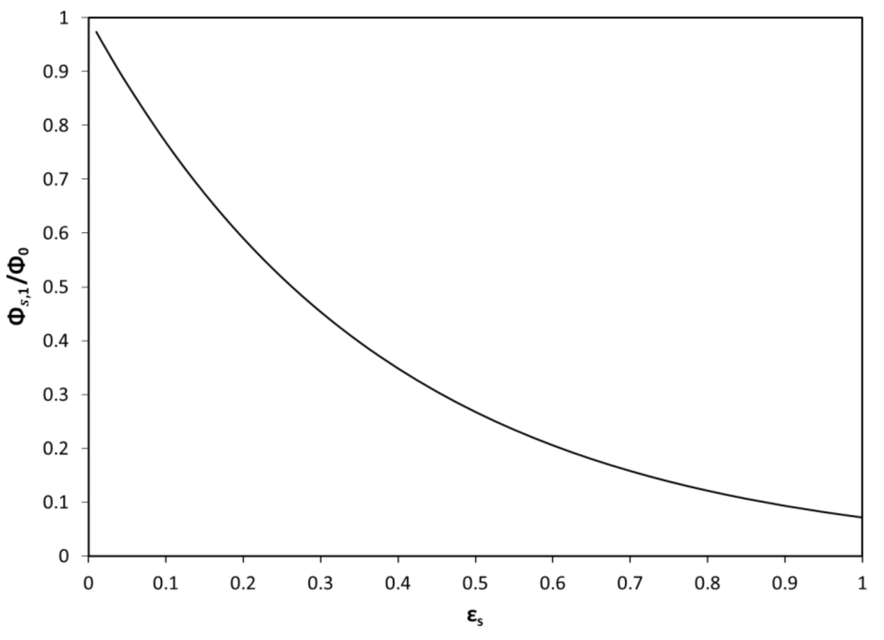

Figure 5-3. Ratio of the gamma-rays penetrating the Plexiglas wall: α_1 = 0.01031 m^2/kg, ρ_1 = 1190 kg/m^3, L_1 = 0.0064 m

Assuming a homogenous mixture and plotting the attenuation for two media at the same time using Equation 5-2 results in:

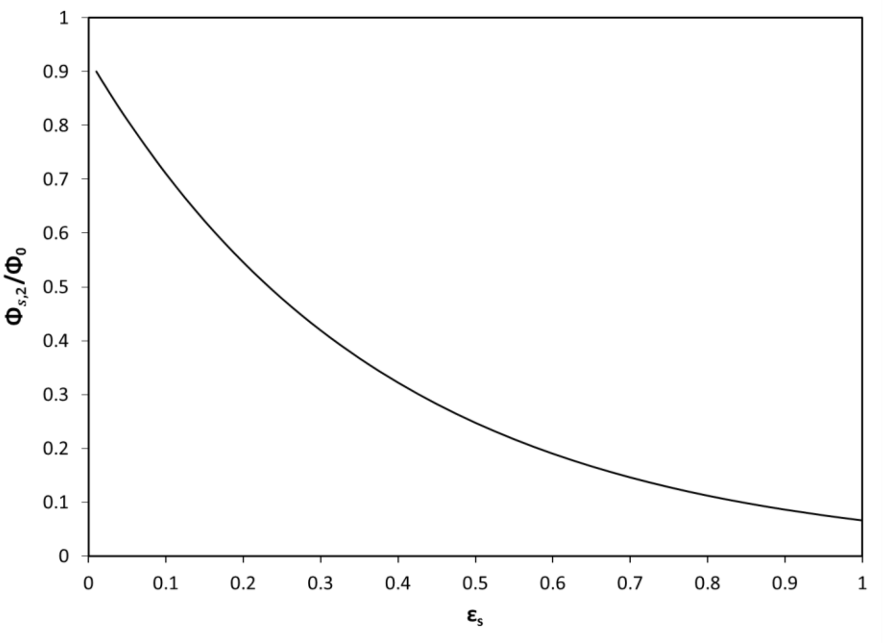

Figure 5-4. Ratio of the gamma-rays penetrating both the Plexiglas wall (α_1 = 0.01031 m^2/kg, ρ_1 = 1190 kg/m^3, L_1 = 0.0064 m) and bed of solids (α_2 = 0.00954 m^2/kg, ρ_2 = 1470*(1-ε_s) kg/m^3, L_2 = 0.1905 m)

In the freeboard, the solid holdup ε_s is estimated to be less than 0.1 right above the bed surface when the gas velocity is 1 m/s. The solid holdup decreases with freeboard height and increases with gas velocity (Morooka et al., 1980). According to Figure 5-4, the attenuation is then negligible and an in situ calibration is not necessary in our case. This is fortunate as an in-situ calibration would present the following issues:

1- An in situ calibration may modify the hydrodynamics of fluidized bed during the calibration;

2- For the tracer at an arbitrary position during the calibration experiment, the solid holdup may fluctuate in the fluidized bed, between the source and the bed wall. As a result, during a dynamic experiment, the solid holdup profiles might be significantly different from the time-averaged holdup experienced during the calibration.

3- The fact that solid holdup profiles change with velocity would require the experimenter to conduct calibration experiment for every velocity being studied which would make the CARPT a time-consuming method.

The ratio of the irradiance I at a distance r from the source to the irradiance I_0 for the detector as close as possible to the source can be obtained from:

$$\frac{I}{I_0} = \frac{\mathrm{r}_0^2 \Phi_s}{r^2 \Phi_0} \tag{5-3}$$

In which:

I: Radiation received at distance r from the tracer, J/s/m^2

I_0: Radiation received at distance r_0 from the tracer, J/s/m^2

r: distance from the source, m

r_0: minimum distance between source and detector (it cannot be 0 because the source is within a simulated agglomerate and the detector occupies a finite volume), m

The above equation is also known as Inverse Square Law.

Considering that the diameter of the spherical plastic housing in which the tracer is located inside is 0.01 m, and the thickness of aluminum shield is 0.00508 m (Saint-Gobain Ceramics & Plastics, Inc.), the r_0 can be estimated to be 0.01458 m.

Now by combining the Inverse Square Law (5-3) and the Beer-Lambert Law (5-2):

$$\frac{I}{I_0} = \frac{\mathrm{r}_0^2}{r^2} \times \exp\left(\sum -\alpha_i \rho_i L_i\right) \tag{5-4}$$

Considering the worst case in which the radiation passes through the air, Plexiglas wall and the bed of particles when the solid hold up is 0.1, we can plot the $\frac{I}{I_0}$ as a function of the tracer distance to the detector, using the above equation:

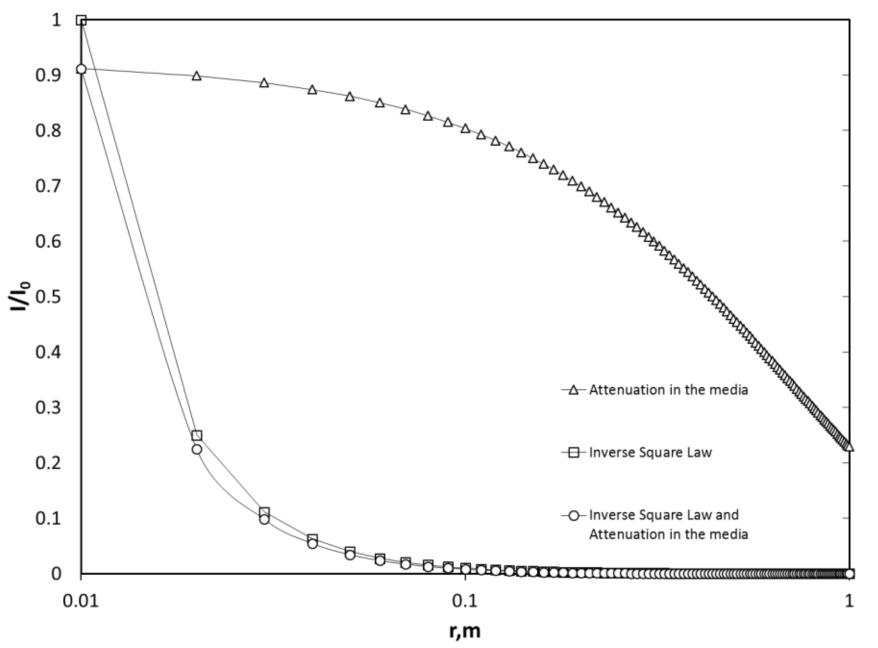

Figure 5-5. Effect of attenuation in media and Inverse Square Law on radiation received by detector at different distances

It is evident that the radiation received by the detector is primarily affected by the Inverse Square Law. This will be also proven to be true experimentally in the next section.

To sum up, the error due to attenuation of radiation in the media is small and its effect cannot be controlled or be eliminated due to the chaotic nature of solid holdup profiles around each instantaneous tracer position during the experiment. This error cannot be eliminated even by an in situ calibration as this effect is present there too. Thus, a better understanding of this source of error is required and novel ways to eliminate it can be of interest. Fortunately, in our experiments, it was shown that the radiation flux that reaches a detector is mostly affected by the Inverse Square Law rather than the attenuation in the media; as a result, an ex situ calibration would suffice and be accurate enough.

5.3.6 Calibration Procedure

Typically, once the geometry of the detectors has been selected, the radioactive tracer is positioned at several hundreds of known positions throughout the column and the intensity counts received by each detector are measured. As the position of the detectors and the position of the tracer is known, the distance between the tracer and each detector can be easily calculated. For a given position, detectors scan and register the counts for a few seconds at a known frequency, and as a result, hundreds or thousands of intensity counts are acquired. These counts for a certain period (herein and after known as sampling time, which is set based on the data acquisition speed) are averaged to obtain the mean counts (or count rate) for each detector.

The outcome of calibration experiments is a map between intensity counts and tracer position and it includes all the factors that affect the count rate registered by the detector such as distance, solid angle and medium composition as well as other complex-to-monitor variables.

This procedure is followed here in this study; except that the tracer was positioned in 13 arbitrary known positions.

Using the raw data obtained, an equation can be fitted that relates the intensity counts (or count rate) to the distance between the detector and tracer, for each available detector. The equation fitted here is:

$$d = k * I^{-\frac{1}{2}} - c \tag{5-5}$$

where *d* is the distance of tracer from the detector and *I* is the intensity (count rate) received by the detector. *k* and c are equation parameters and are derived from the curve fitting. The above equation is based on the Inverse Square Law. A calibration curve for detector 1 is shown below. It confirms that the interaction of the detector with the radiant flux can be described with the calibration constants k and c.

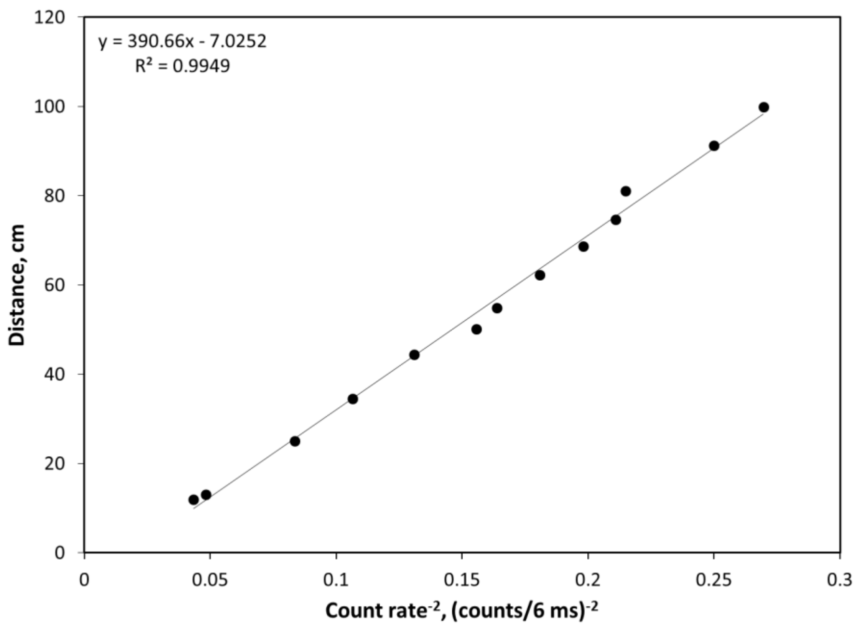

Figure 5-6. Calibration curve for detector 1(S.N # 638) - Configuration F

5.3.7 Effect of solid angle

The effective of solid angle, as well as other factors, are discussed extensively in Degaleesan (1997).

The present study assumes that the contributions of solid angle, column composition, and the wall path as well as other mentioned factors are either negligible or are following the same trend as the contribution of distance, the calibration curve will be a fairly defined line.

An assumption with the similar concept was used by Lin et al. (1985) and (Sanchez Careaga, 2013) who eliminated or neglected the effect of solid angle respectively. Devanathan (1991) assumes that intensity is a monotonic function of distance. This assumption is more reliable when using a collimated detector such as in CT (Kumar, 1994).

5.3.8 Reconstruction of data (Algorithm)

Tracer particle location reconstruction is a procedure in which instantaneous counts recorded by all the detectors during an experiment are converted to tracer positions using the calibration curve obtained in previous steps.

The accuracy of the reconstructed tracer particle location using the mapping method depends on the level of refinement of the calibration mesh (Rados, 2003). In order to obtain a resolution that is much better than the calibration mesh resolution, one would need a model to interpolate accurately the contribution of all the variables that affect the number of counts between the calibration locations. This is a complicated task, and it requires depth modeling of the gamma radiation and its interaction with the medium and detector. This task can be done using Monte-Carlo simulation (Gupta, 2002; Larachi et al., 1997; Roy et al., 2002).

In this work, a weighted least square regression approach which was originally formulated by Lin et al. (1985) was used to estimate the position of the particle. As this method of weighted least square regression was used by Devanathan (1991) and Sanchez Creaga (2013) and many others, the details involving the calculation is omitted. This method has gone through some refinement and improvement in order to increase the speed of calculation and to diminish the error in positioning the tracer. Significant improvements were added to this method by Degaleesan (1997) and Rados (2003)

5.3.9 Error associated with system

Sources of error in CARPT can be categorized in the followings:

- Statistical nature of the gamma radiation (Randomness of radionuclide disintegration): The emission of gamma-rays from a radioactive source is a statistical process which follows a Gaussian distribution with the mean n_c which is the number of counts emitted per unit time, and standard deviation of $\sqrt{n_c}$ .As a result, the standard error which is the standard deviation/mean has the magnitude of $1 / \sqrt{n_c}$ (Knoll, 2010). In simplified words, if a detector registers more intensity counts, less error is associated with the registered values and vice versa.

- Variation of sampling time (Inconsistency of duration of scan between two instantaneous positions): It was found that the sampling time is not consistent and may vary a few milliseconds in one scan relative to the average sampling time. Even though this variation is not significant, but the error accompanied with that exists. The source of this error is unknown to us, but we guess this might be due to the limitation of data transfer rate from digiBase to computers or a simple software or hardware glitch.

- Electrical Noise: This error is caused by any electrical signal acquisition or signal processing equipment used in the system.
- Experimental error: This error is caused by the experimenter's mistakes generally, for example poor detector alignment or imprecise tracer positioning during the calibration experiment.
- Tracer movement during the sampling time: No matter how fast the sampling time is, the tracer moves over a finite distance during the scanning time. This change in distance between the tracer and detector will consequently result in the change of counts received by a detector during one single scan.
- Fluctuations in gas and solid holdup in the column: In short, the gamma-rays received by the detectors are affected by the attenuation in the media being traversed. Fluctuation in gas-solids hold up affects the length of the media being passed over by the gamma-rays and as a result of that, affects the intensity counts registered by detectors. In our case, this error is proven to be negligible. This error is discussed in the "calibration section" thoroughly.

5.4 Trajectory of cluster flux above the bed surface

The primary objective of using RPT was to find and simulate the entrainment of particles and clusters in the freeboard. To achieve this, first we needed to distribute the twelve detectors in a strategic way along the bed with the following constraints:

1- Twelve detectors shall cover 1 m of the column along the Z-axis.

2- Detectors shall be as close as possible to the column. This will allow the detectors to register as many counts as possible. Registering more counts reduces the error associated with the randomness of radionuclide disintegration.

3- The sampling time shall be as short as possible to allow us to track the fast movements of particles in the freeboard. This was achieved by assigning one laptop to each detector. One should take a note that reducing the sampling time results in registering fewer counts by each detector and this will eventually increase the error.

4- Increasing the activity of the radionuclide: we were limited by the health and regulatory issues. We worked with the maximum allowable activity of 300 μCi.

Considering these constraints, the only option for us to reduce the error in the RPT was to find the best configuration of distributing the twelve detectors, around the 0.2 m O.D column, in a way they cover 1 m of the column height.

A literature review was performed, and the suggested configurations were extracted. Then, the four applicable configurations have been tested which the descriptions are available in the table below. Exact positions of the detectors are available in Appendix D.

Table 5-1. Details of detector configurations tested

Configuration	Total number of detectors	Total height of coverage, m	Number of detectors per plane	Number of planes	Distance between adjacent planes, m	Angle of stagger between adjacent planes
A	12	1	3	4	0.305	60°
B	12	1	1	12	0.0826	60°
E	12	1	1	12	0.0826	120°
F	12	1	1	12	0.0826	In order:180°-60°-180°-120°-180°-60°-180°-120°-180°-60°-180°

In Table 5-1, details of four different configurations are listed. One should notice that we were limited by the followings:

- Only twelve detectors were available
- The twelve detectors shall cover 1 m of the freeboard.
- The tracks which the detectors are mounted (mentioned in chapter 2) on are located at every 60° around the column.

Configuration A uses three detectors per plane. On each plane, three detectors are arranged every 120° in an equilateral triangle. Adjacent planes are separated by 0.0826 m, and the detector planes are staggered so that the vertices of the equilateral triangles of two adjacent planes are directed opposite to each other. Also, the twelve detectors cover 1 m of the freeboard. This arrangement was proposed and tested by Roy et al. (2002) and was proved that it will improve the detection resolution, but at the cost of additional detectors. Here, we did not plan to increase the number of detectors.

Configurations B, E and F use only one detector per plane, and adjacent layers are separated by 0.0826 m so that the twelve detectors can cover the 1 m of the freeboard. The only difference between these configurations is in their stagger angle.

Then error associated with each configuration was evaluated. First, a separate calibration curve was developed for each configuration to eliminate the effect of set-up geometry on the number of counts received by each detector. Then, the tracer was placed on the tip of a rotating rod which forced the tracer to a known prescribed path (Sanchez Careaga, 2013). Meanwhile, the RPT system started registering counts from each detector. Afterward, the instantaneous positions derived from RPT were compared to the real positions. By comparing the distance between each calculated position from CARPT with the corresponding actual position, the average error for each configuration can be obtained. For this purpose, we will look at the average distance between the actual and predicted position (Equation 5-6); less average distance represents a better prediction of the true tracer position.

$$d = \sqrt{(x_{true} - x_{predicted})^2 + (y_{true} - y_{predicted})^2 + (z_{true} - z_{predicted})^2} \quad \textbf{5-6}$$

Table 5-2. Error on each tested configuration

Configuration	Overall Coverage, m	Average distance between true positions and predicted positions, mm
Configuration A	1	33.0
Configuration B	1	30.1
Configuration E	1	23.8
Configuration F	1	21.7

Looking at the results in Table 5-2, it is clear that the F is the best among the four configurations as it gives a better prediction of true tracer position.

5.5 Suitability of RPT for tracking the clusters motion in the freeboard

In order to check whether with the current RPT system is suitable to track the tracer, the following argument is proposed:

Consider the tracer is in a cluster which is ejected with the velocity of V [m/s] to the freeboard. During a time interval of Δt, the tracer travels from the position 1 to position 2, and the distance between these two positions can be calculated by:

$$d_{1\ to\ 2} = V \times \Delta t \quad \textbf{5-7}$$

The current RPT system records the counts received by each detector in Δt intervals. This interval is called sampling time, and it has the average value of 5 to 6 ms.

Based on the model proposed by Baron et al. (1988), the ejection velocity of a cluster to the freeboard can be calculated using the following equation:

$$U_{cluster\ ejection} = 2.1 \times U_{bubble,bed\ surface} \qquad \textbf{5-8}$$

In the above equation, the bubble velocity at the bed surface can be found using the equation, which was originally proposed by Davidson and Harrison (1963) and modified by Hilligardt and Werther (1987):

$$U_b = \varphi\left(V_g - U_{mf}\right) + 0.711\theta(g\ d_b)^{0.5} \qquad \textbf{5-9}$$

In this equation, V_g [m/s] the gas velocity, U_{mf} [m/s] minimum fluidization velocity and d_b [m] is the bubble diameter. φ and θ are dimensionless factors and have the value of 0.8 and 1.39 respectively, in our case. Finally, the bubble size can be calculated using Darton's (1979) equation. By inserting the variables into the above equations, it was found that the ejection velocities of the cluster are 4.2 m/s and 6.35 m/s for fluidization gas velocities of 0.3 m/s and 1 m/s respectively.

A cluster which includes the tracer and is ejected with a velocity of 4.2 m/s, will move 21 mm during the 5 ms sampling time period. If the cluster is ejected at 6.35 m/s, the tracer will move 31.75 mm. Consequently, the spatial resolution of the measurements cannot be better than 21 or 31.75 mm, depending the operating conditions. This amount of error is not suitable for tracking the motions and trajectories of particles in the freeboard.

5.6 Model Development for Application of Radioactive Tracer Technique to Entrainment Measurements

5.6.1 Introduction

In the last part, it was shown that the RPT is not applicable for tracking the fast movements of clusters in the freeboard. This made us come up with a new idea to use radioactive tracers to measure the decrease with height of the clusters concentration in the freeboard. As shown in Chapters 3 and 4, this provides useful information such as the TDH. Our goal was to use the tracer measurements to obtain information in the lower regions of the freeboard, where the flux is too high for the isokinetic probes.

In this part, we propose a model to measure the entrainment of clusters which are ejected from fluidized bed using a modified radioactive tracer technique in which the detectors are collimated. First, the feasibility of this modeling will be evaluated using a program developed in MS Excel. Then, it will be followed by one experiment to validate the model.

5.6.2 Theory

Clusters are agglomerates of particles which are portions of the bed projected into the freeboard by the bubbles which are erupting at the bed surface. Thus the composition of clusters is the same as the bed composition (Baron et al., 1988). Based on the model proposed by Large et al. (1976) which was later verified by Baron et al., (1988), one can write:

$$F_c = F_0 \exp(-A_c z) \qquad \textbf{5-10}$$

In the above equation, F_c is the cluster flux at height z above the bed surface, F_0 is the total flux of particles ejected from the bed surface, A_c is a constant for given operating conditions. Assuming that the cluster flux at height of z is a function of radial position as well and not dependent on the angular position, one can write:

$$F_c = F_{00} \exp(-A_c z) \times \left|(1 - \frac{r}{R})\right|^n \qquad \textbf{5-11}$$

In Equation 5-11, R is the inner diameter of the column in meter, r is the radial position of the cluster in the freeboard in meter. n is an unknown exponent which can have any value depending on the behavior of the clusters at different radial positions. F_{00} is the total flux of particles ejected from the center of bed surface. F_C is the cluster flux at a certain location (r and z). Note that Equation 5-11 assumes that the exponent n is independent of the height z.

Now, assuming that the drag force exerted on the cluster is negligible comparing to the kinetic energy and the gravity one can write the force balance as:

$$m_c \frac{du_c}{dt} = -m_c g \qquad \textbf{5-12}$$

By integration of the above equation we have:

$$u_c = -gt + u_{ej} \tag{5-13}$$

In the above equation, it is considered that the cluster is ejected from the bed surface (Z=0 and t = 0) with the velocity of $U_c = U_{c,ej}$.

$$\frac{du_c}{dt} = \frac{d^2z}{dt^2} \tag{5-14}$$

By substituting the Equation 5-14 in 5-12, and integrating, we will have:

$$z = \frac{-gt^2}{2} + u_{c,ej}t \tag{5-15}$$

By solving the Equation 5-14 for *t*, and substituting the answer in 5-13 we have:

$$u_c = u_{c,ej} + \left[-u_{c,ej} + \sqrt{u_{c,ej} - 2gz}\right] \tag{5-16}$$

Which can be simplified to:

$$u_c = \sqrt{u_{c,ej} - 2gz} \tag{5-17}$$

Knowing that:

$$when\ \ u_c = 0, z = TDH \tag{5-18}$$

We can conclude that:

$$u_c = \sqrt{2g(TDH - z)} \tag{5-19}$$

Now by dividing the Equation 5-11 by 5-16 we have:

$$\varphi(r,z) = F_{00}\frac{\exp(-A_c z) \times \left|(1 - \frac{r}{R})\right|^n}{\sqrt{2g(TDH - z)}} \tag{5-20}$$

Where:

φ(r,z): Mass concentration of cluster in the freeboard at r and z, $\frac{kg_{cluster\ solids}}{m^3{}_{freeboard}}$

It is clear that at r = 0 and z = 0:

$$\varphi_{00} = \frac{F_{00}}{\sqrt{2g(TDH)}} \qquad \textbf{5-21}$$

In fact, φ_{00} is the mass concentration of cluster ejected the from the center of the bed surface to the freeboard, $\frac{kg_{cluster\ solids}}{m^3{}_{freeboard}}$

Therefore one can write:

$$\varphi(r,z) = \varphi_{00} \times \sqrt{\frac{TDH}{TDH - z}} \times \exp(-A_c z) \times \left|(1 - \frac{r}{R})\right|^n \qquad \textbf{5-22}$$

Assuming that the cluster is a piece of emulsion phase and considering the fact that the coke powder used in our experiments is at the boundary between Geldart's group A and B, the voidage of the emulsion phase is the same as the voidage at minimum fluidization velocity, we can write:

$$\rho_{mf} = \frac{kg_{cluster\ solids}}{m^3{}_{cluster}} \qquad \textbf{5-23}$$

Therefore, the probability that, at a given time, a given location in the freeboard is occupied by a cluster is:

$$p(z,r) = \varphi(r,z)/\rho_{mf} \qquad \textbf{5-24}$$

Assuming that the tracer represents a portion of the bed of a corresponding mass, the probability *f* that the tracer is at location (r,z) is given by:

$$f = p(r,z)\frac{m_{tracer}}{M_{bed}} = f_{0,0} \times \sqrt{\frac{TDH}{TDH - z}} \times \exp(-A_c z) \times \left|(1 - \frac{r}{R})\right|^n \qquad \textbf{5-25}$$

The relation between f_{00} and φ_{00} can be defined as:

$$f_{00} = \varphi_{00} \times \frac{1}{\rho_{mf}} \times \frac{m_{tracer}}{M_{bed}} \qquad \textbf{5-26}$$

5.6.3 Assumptions for simulation and analysis

In this section, a program is developed to simulate the presence of tracer at different heights using the proposed model. Then, through various analyses and virtual experiments, we will be able to understand if the unknown parameters (f_{00}, a, n) can be obtained using a set of experiments.

To make the analysis more realistic, it was assumed that the current bed is being studied. Thus, we have (Figure 5-7):

1- 1 m of the freeboard above the fluidized bed surface is selected for this study. It is assumed that the bed surface is Z = 0, and the height available above the bed surface is 1 m only. So the tracer can be in any axial location between Z = 0 and Z = 1.

2- The center of the column is assumed to have the value of X = 0, and the detectors have negative X values.

3- It is assumed that the X axis is passing through the center of the detectors. As a result, the detectors will have zero Y values.

4- The detectors are considered as point detectors. This assumption is also true for the tracer.

5- An Iron sheet with the thickness of 20 mm was introduced between the column and the detectors. This metal sheet is located tangent to the column flange (O.D. = 266.7 mm). As a result, the Iron sheet has an X value of -133.35 mm.

The Iron sheet (from now on known as the shield) can have an arbitrary number of openings (Max 12) with different sizes and configurations. It is assumed that the shield can block 100% of the radiation from the radioactive tracer unless the radiation passes through the opening. This assumption is relatively true as the 20 mm thick Iron can attenuate the gamma radiation more than 80% according to the Beer–Lambert law. This sheet covers the column height and width entirely. So the dimensions of the sheet are as follow:

Height = 1 m, Length = 203.2 mm (8 in), Width = 20 mm

6. To greatly simplify the calculations the detection volume was calculated assuming a very thin plate. This increases the vertical span of the detection volume of each detector, maximizing any error caused by the vertical span.

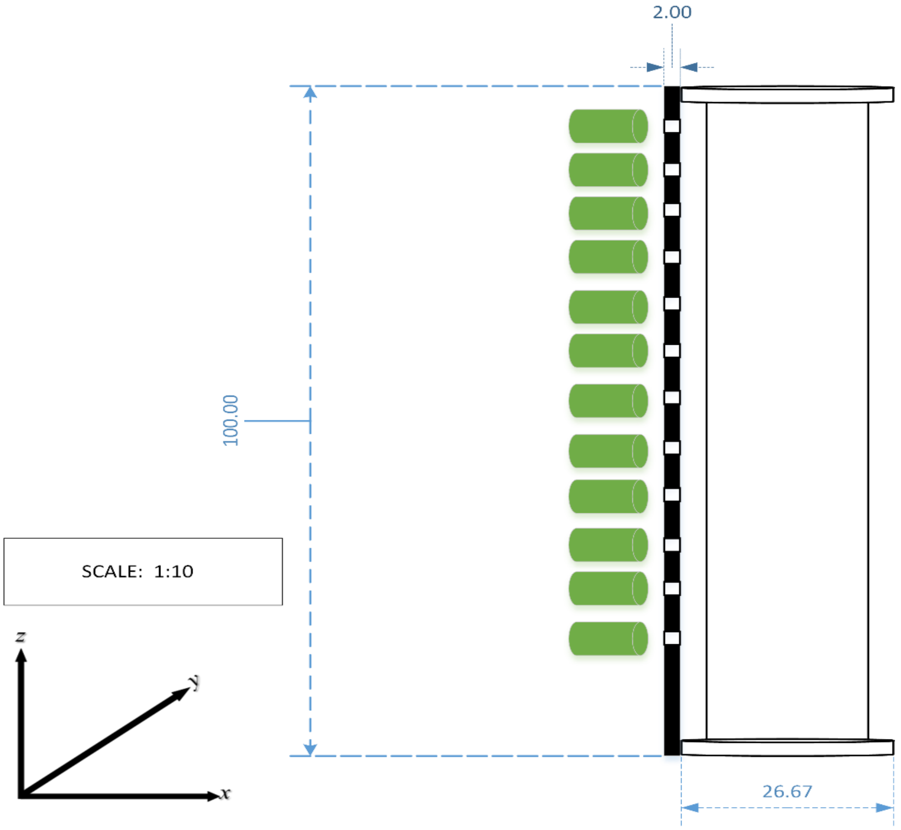

Figure 5-7. Sketch of column, shield and detectors

5.6.4 Geometry of the openings

The sheet has twelve openings, each at a certain height. The first opening is at Z = 0.1905 m. The next opening is located 0.07 m above this detector. This pattern continues for the rest of the detectors. As a result, the last detector is located at Z = 0.9605 m. It was assumed that the centers of the openings were aligned with the centers of the detectors.

Two different shapes of openings will be considered, and the corresponding results will be individually discussed.

- Narrow opening (Slit): There is no restriction along the Y-axis, and the opening has the same length as the shield. The opening is restricted along the Z-axis, and the size of restriction may vary (Figure 5-8).

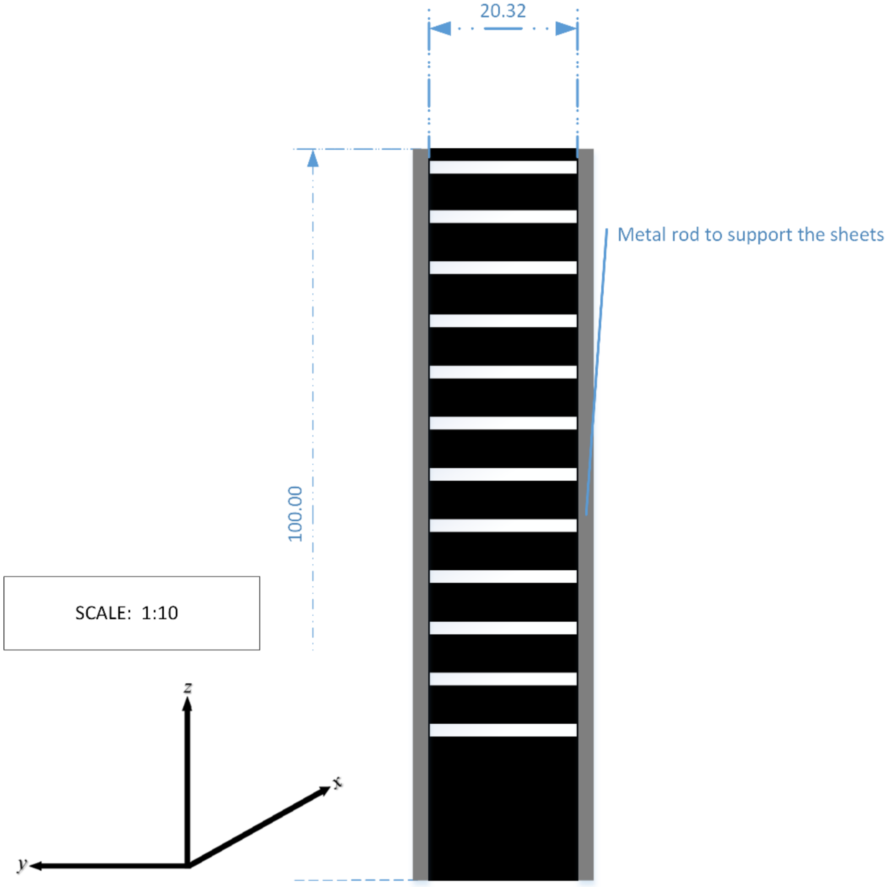

Figure 5-8. Slit opening

- Rectangular/Square opening: There is restriction along the Y-axis as well as Z-axis. If the length of opening on Y-axis is equal to the length of opening on Z-axis, it is called “square” opening (Figure 5-9); otherwise, it is a “rectangular” opening.

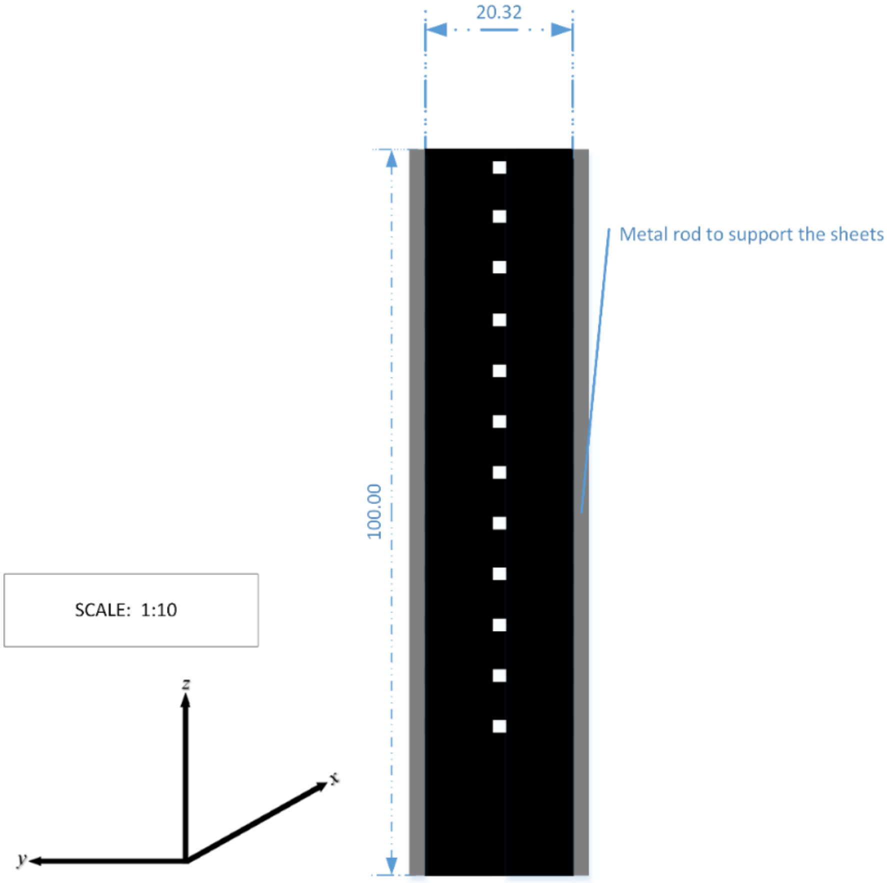

Figure 5-9. Square opening

5.6.5 Methodology (Analysis Procedure)

As mentioned before, a program has been developed in MS Excel, to study different possibilities of the shield opening and detector distance from the shield.

As described earlier, to have a more realistic case, the dimensions of the current column is used in this analysis.

The procedure that the program follows:

1- Generating 10000 lines, where each line represents the presence of a tracer at a specific point and includes the following:

  - Z value, which varies between 0 and 1, and represents the height in which the tracer is located.

- r/R value, which is between -1 and 1, and represents the radial location of the tracer.
- Theta (Θ) which represents the angle between the tracer and the center of the coordinates. This value is between 0 and 2π.

This step actually creates the location of the tracer in 10000 different positions in cylindrical coordinates, considering that this tracer is within the freeboard of the fluidized bed. Each position is selected randomly, using the MS Excel random number generator, such that any point in the freeboard volume has an equal probability of being selected.

2- After this, these values which are in cylindrical coordinates will be transferred to Cartesian coordinates using the following correlation:

$$X = R \times \frac{r}{R} \times \cos\theta$$

$$Y = R \times \frac{r}{R} \times \sin\theta \qquad \textbf{5-27}$$

$$Z = Z$$

It will be further explained why this step is necessary.

3- These data are inserted in the Equation 5-25 to get the fraction of time the tracer spends in a certain position (f). The value of f is calculated for each line.

4- The location of the shield is introduced to the program. In all cases, the shield is tangent to the column flanges and thus, the column side of the shield has an X value of -133.35 mm. The location of the openings, openings width and shield thickness are introduced as well.

5- The positions of the each twelve detectors are introduced to the program. These positions are shown by X_d, Y_d and Z_d. It is worth noting that the center of the detector is aligned with the center of the shield opening.

6- Once the characteristics of the shield and detectors been determined, the program will use a simple equation to determine the value of γ, a parameter which will be later used to determine whether the tracer is within the detection range of view (or range of detection) of a detector. See Figure 5-10 for clarification.

$$\gamma = \tan\alpha = \frac{h_s}{X_d - X_{shield}} \qquad \textbf{5-28}$$

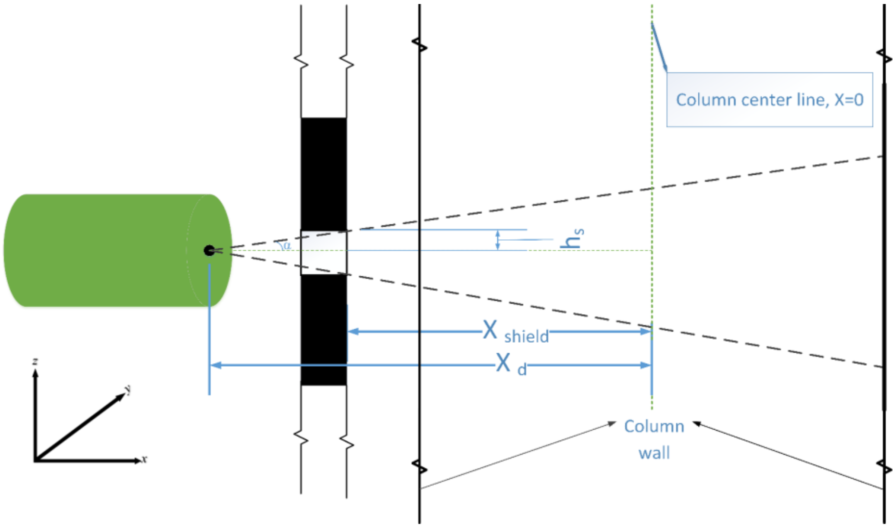

Figure 5-10. Geometry of the radiation reaching the tracer

7- At this stage, first the program calculates the distance of the tracer from each detector. Then by using the calibration data available for each detector, the value of C_1 which is the counts per s received by a detector for each tracer position will be calculated:

$$distance = \sqrt{(X - X_d)^2 + (Y - Y_d)^2 + (Z - Z_d)^2} \qquad \textbf{5-29}$$

$$C_1 = a \times (\frac{1}{distance})^2 + b \qquad \textbf{5-30}$$

a and b are defined from the calibration data, for each detector.

8- Then the program checks if this tracer is within the detection range of the detector or not using the followings:

For slit opening the tracer is within the range if:

$$|Z - Z_d| \leq \gamma \times (X - X_d) \qquad \textbf{5-31}$$

For square or rectangular opening the tracer is within the range if:

$$|Z - Z_d| \leq \gamma_1 \times (X - X_d) \text{ and } |Y - Y_d| \leq \gamma_2 \times (X - X_d) \qquad \textbf{5-32}$$

When the tracer at a certain position is within the range of that detector the program calculates the value of *C,* which is the corrected measured number of counts per second registered by a detector. In fact, the number of counts is corrected according to the fraction of time the tracer was actually in that certain position, using the following equation:

$$C = C_1 * f \qquad \textbf{5-33}$$

For the tracer which is not within the range of the detector, the program set 0 for the value of *C*. This procedure will be done for each tracer position and all the twelve detectors.

9- At this stage, the sum of all *C* values for each detector is calculated and then is divided by the total number of positions. This value is shown by *S* and should be equal to the time-averaged detector signal.

$$S_{detector\ i} = \frac{\sum_{detector\ i} C}{Number\ of\ positions} \qquad \textbf{5-34}$$

The program applies the same procedure to all detectors.

10- From the average signal of all the detectors, one can obtain the values of f_{00}, *a* and *n* by trial and error, using, for example, the MS Excel Equation Solver.

5.6.6 Results from analysis

To check if the model is dependent on the radial position and independent of angular position, we do the following analysis:

1- Detectors are set at positions A.

2- Estimate the value of f_{00}, a and n. (In all the analysis performed, the values of f_{00} and a were 0.01 and 4 respectively.)

3- Change the value of n up to a range and register the value of S_x for each detector.

4- Move the detectors to next position (along the X axis only), which is further from the column and repeat the steps 2.

5- Compare the values of S_x/S_A for each detector over the range of n.

If the value of S_x/S_A is changing with changing the n, it shows that the value of n can be obtained through the two sets of experiments.

The analysis has been done for three aforementioned configurations of opening. This analysis is done by virtually pulling back each detector along their X axis and placing them in 4 different locations.

Table 5-3. Virtual location of the detectors in the analysis

Position	X(m)	Y(m)
A	-0.17	0
B	-0.22	0
C	-0.26	0
D	-0.31	0

The result is shown below for bottom (Z = 0.1905 m), middle (Z = 0.4705 m) and top (Z = 0.9605 m) detectors only.

5.6.6.1 Results in a slit opening

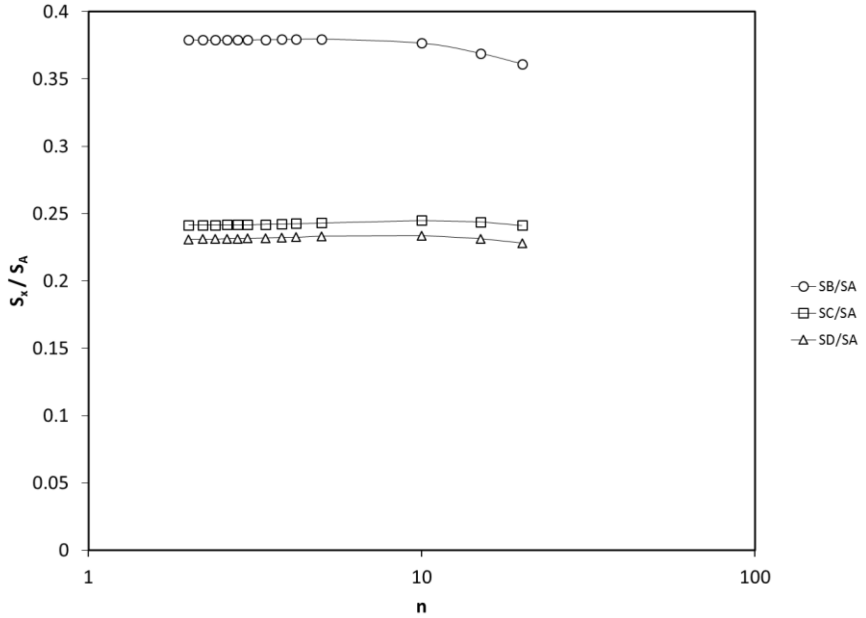

Figure 5-11. Detector 2 (Z = 0.1905m), shield opening: ∆z = 0.01 m, ∆y = 0.203 m

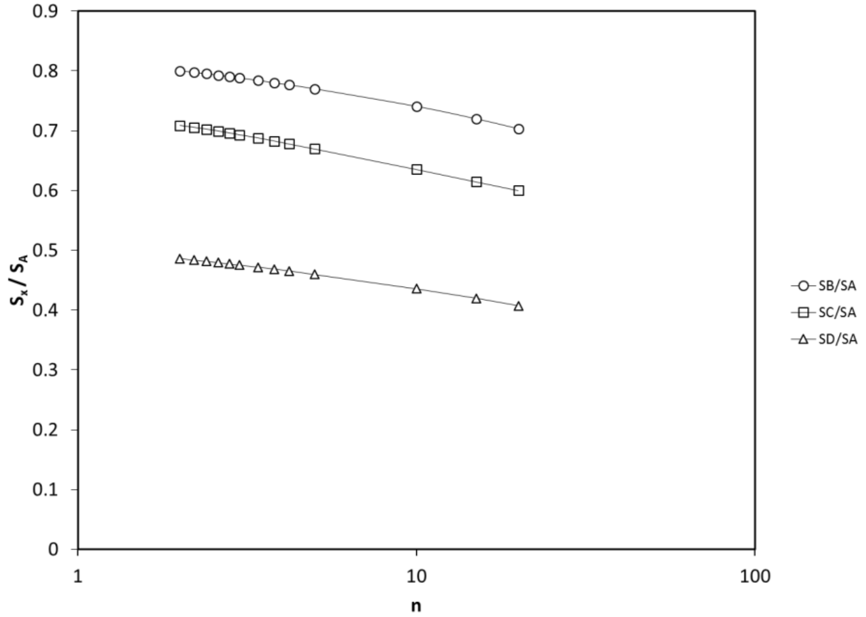

Figure 5-12. Detector 2 (Z = 0.4705m), shield opening: ∆z = 0.01 m, ∆y = 0.203 m

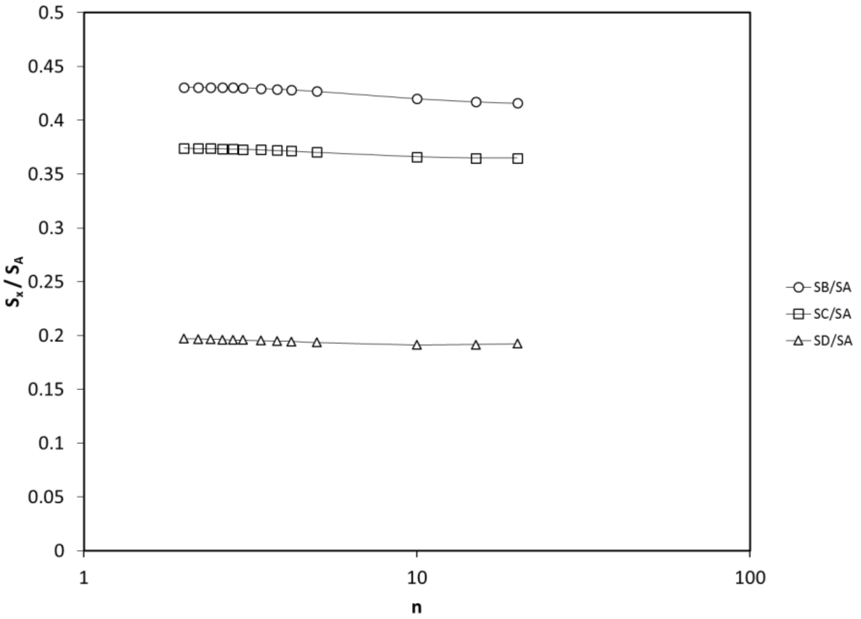

Figure 5-13. Detector 2 (Z = 0.9605m), shield opening: ∆z = 0.01 m, ∆y = 0.203 m

5.6.6.2 Result in a rectangular shape opening

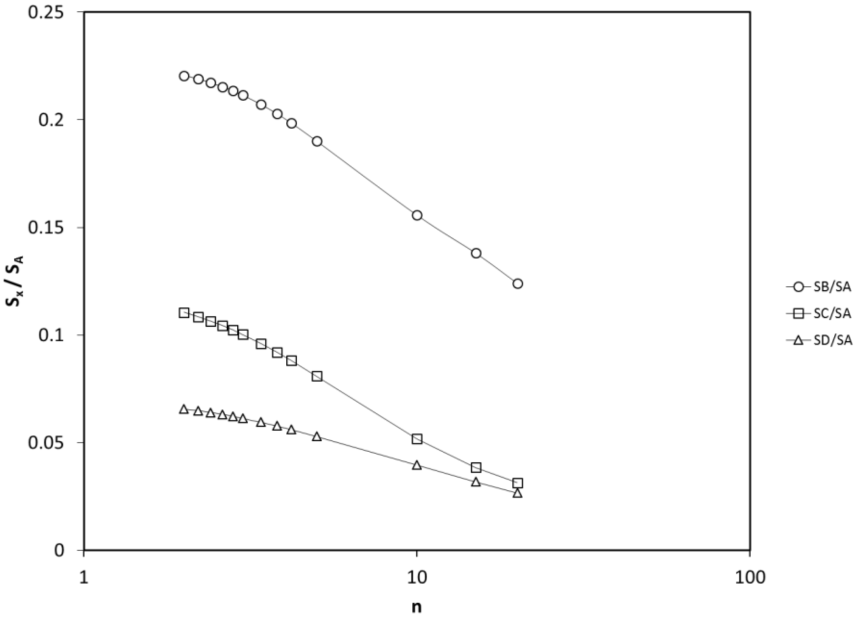

Figure 5-14. Detector 1 (Z = 0.1905m), shield opening: shield opening: ∆z = 0.01 m, ∆y = 0.02 m

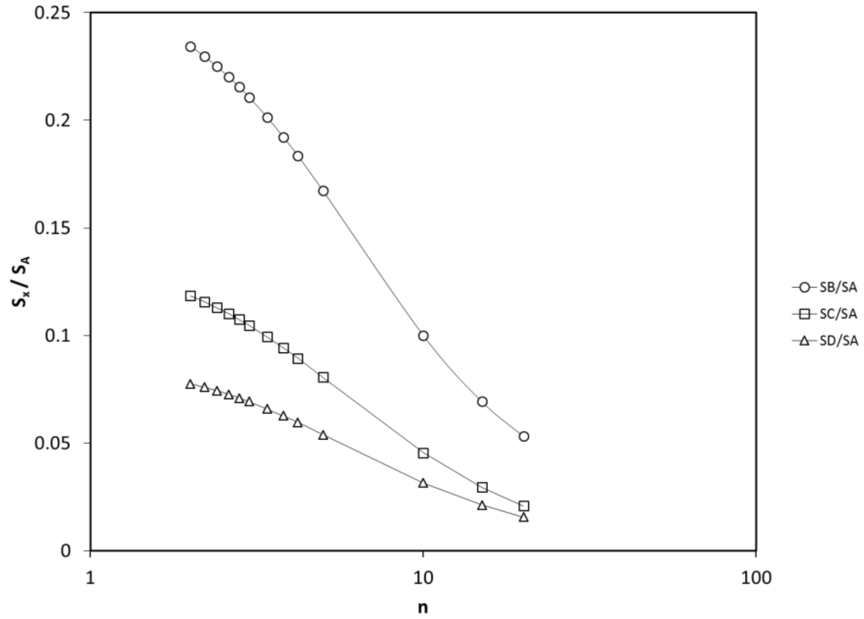

Figure 5-15. Detector 2 (Z = 0.4705m), shield opening: ∆z = 0.01 m, ∆y = 0.02 m

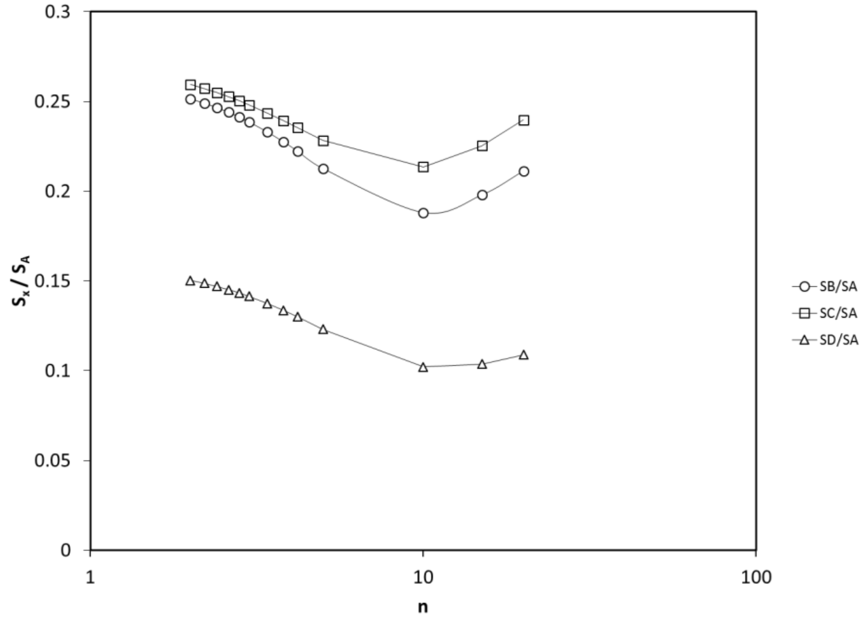

Figure 5-16. Detector 3(Z = 0.9605m), shield opening: ∆z = 0.01 m, ∆y = 0.02 m

5.6.6.3 Result in a square shape opening

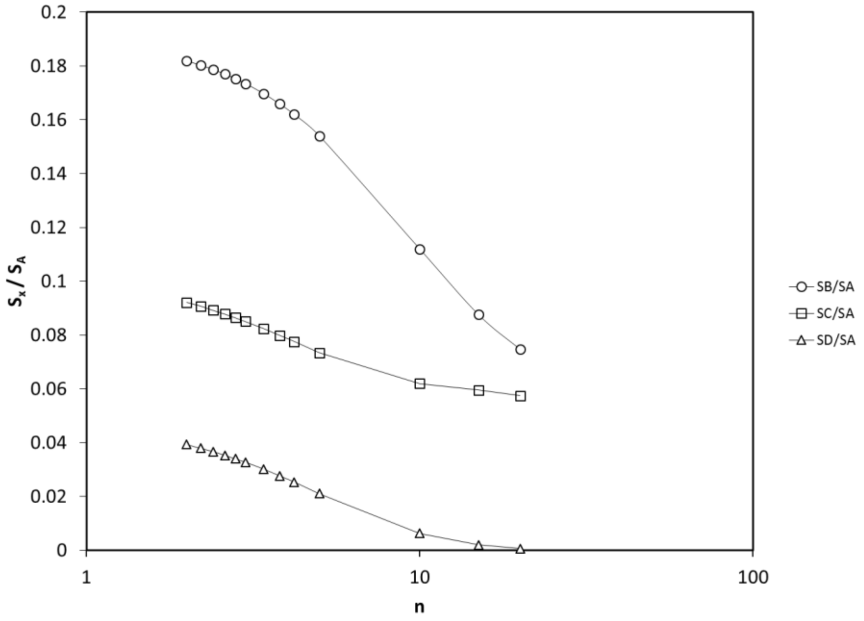

Figure 5-17. Detector 1 (Z = 0.1905m), shield opening: ∆z = 0.01 m, ∆y = 0.01 m

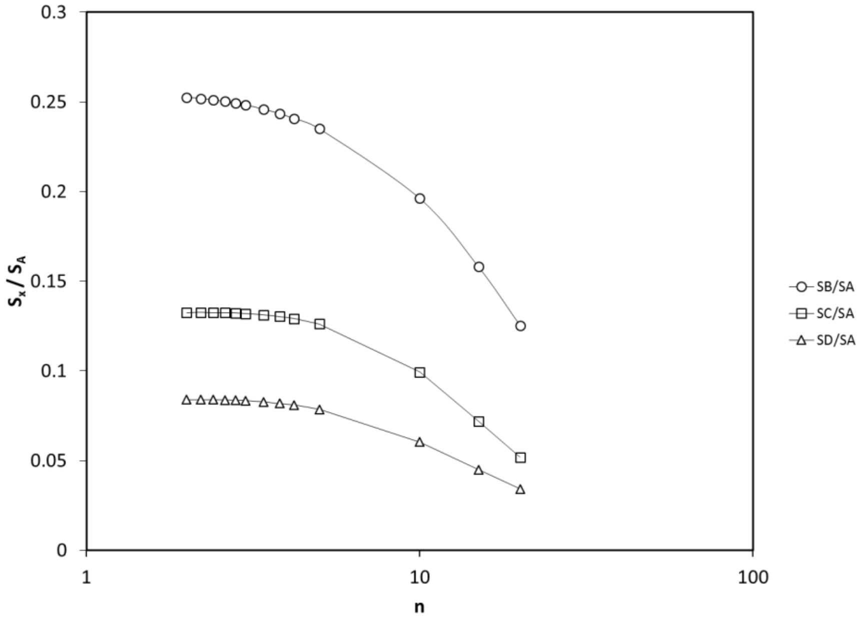

Figure 5-18. Detector 2 (Z = 0.4705m), shield opening: ∆z = 0.01 m, ∆y = 0.01 m

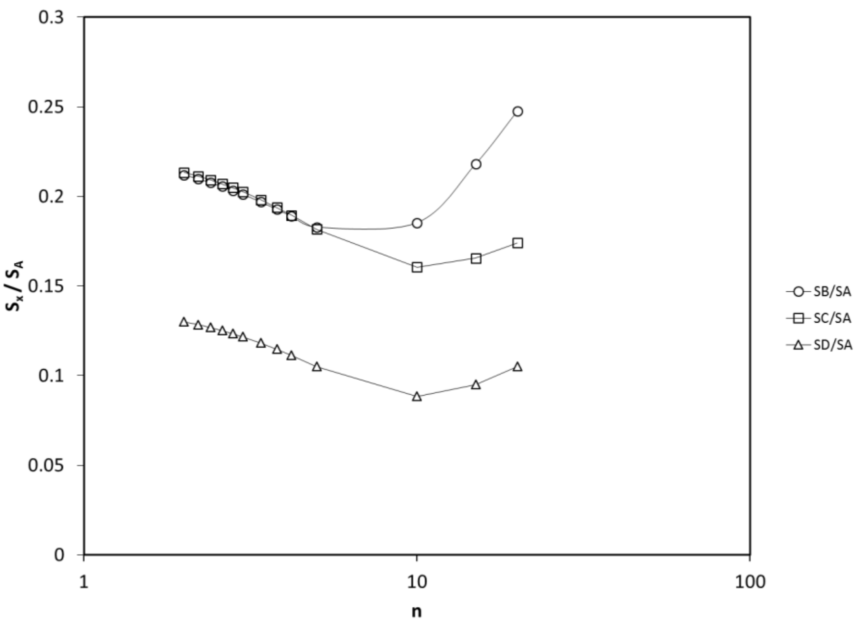

Figure 5-19. Detector 3 (Z = 0.9605m), shield opening: ∆z = 0.01 m, ∆y = 0.01 m

5.6.7 Discussion on results from analysis

The slit opening, the S_x/S_A does not change significantly with changes in *n* especially for the very top and very bottom detectors. However, in both square and rectangular openings, sensitivity of the S_x/S_A with *n* is observed. When *n* is changing from 2 to 5, for all the selected detectors, the ratio of S_B/S_A is changing by more than 10% except for the square opening and the middle height detector, which this ratio is about 7%. Therefore, and based on this analysis, it is best to use the rectangular opening (∆z = 0.01 m, ∆y = 0.02 m) to ensure there is enough sensitivity to *n* for all the detectors. With enough sensitivity to *n*, and repeating the same set of experiments that were conducted virtually (pulling the detector back from position 1 to position 2) the three equation unknowns, f_{00}, *a* and *n* can be expected to be easily obtained. This means that the developed configuration could be applied to measure the decrease of the clusters concentration in the freeboard, even if this decrease does not exactly confirm to the exponential decrease that was assumed for the analysis.

5.6.8 Experimental results and discussions

To test the model in real conditions, sets of experiments were conducted in the current fluidized bed. The experimental conditions are as follows:

1- Eleven detectors were placed at the vertical distance of 0.14605 m (5.75 inches) right on top of each other (Same X and Y value, different Z). However, due to technical limitations, the distance between the detector 6 and 7 was 0.2922 m. As a result, 1.6 m of the column was monitored. The first detector (most bottom detector) was found to be monitoring the region slightly below the bed surface and the other ten detectors were above the bed surface.

2- An Iron sheet with the thickness of 19 mm (3/4 inches) was introduced between the column and the detectors. This metal sheet is located at the distance of 57.17 mm from column wall and as a result, the column side of the iron sheet has an X value of -158.8 mm (Reference: Center of the column).

3- One opening on the shield with the following dimensions was introduced in front of each detector: $\Delta z = 9.53$ mm, $\Delta y = 19$ mm (i.e. very close to 10 mm by 20 mm assumed in the previous analysis). Effort was made to ensure the center of the openings are aligned with the center of the detectors.

4- The radioactive tracer was enclosed in a plastic sphere with the diameter of 19 mm. However, due to material limitations, we were unable to exactly match the density of this sphere with the estimated density of emulsion phase (870 kg/m^3). The final density of plastic sphere was 1037 kg/m^3. As a result, segregation would be expected at low fluidization gas velocities. We therefore performed experiments at the highest fluidization gas velocity used in the previous chapters, $V_g = 0.9$ m/s, where no or least segregation can be expected due to high agitation and turbulence in the bed. Above all, in the previous chapters, it was found that the TDH and the resulting ejection velocity of the clusters from the bed surface is the highest at this fluidization velocity. Based on this fact, experiments at this fluidization velocity are tougher tests for the new radioactive method.

The tracer was introduced to the bed and the radioactive experiments were conducted for one gas superficial velocities and the three different bed wetnesses as well as for the dry bed. All the experimental conditions were matching the conditions of experiments conducted in Chapters 3 and 4. For these experiments the sampling probes were pulled all the way up to the column lid.

For each experimental condition (bed wetness), two sets of data were obtained:

Set A: The surface of the detectors are tangent to the detector side of the shield, and thus have a distance of 76 mm from the column wall. For the sake of brevity, in the context of this thesis, these experiments are referred as “Regular experiment” and parameters related to this experiments are shown with the subscript of A.

Set B: The detectors are pulled back 50.8 mm away from the column, resulting in a distance of 127.05 mm between the detectors surface and the column. In the context, these experiments are referred as “pulled-back experiment” and parameters related to this experiments are shown with the subscript of B.

For each set of experiment (or run), data from the eleven detectors were obtained for about 30 minutes and the average bed height was obtained by monitoring the pressure gradient during the run.

In each set of data, the sum of counts for each detector was obtained and pre-treatments and corrections were performed on them:

1- Considering that the tracer activity decays with time, the first experiment was chosen as a (time) reference, and the sum of the counts were corrected accordingly.

2- Considering the slight variation in sampling time for each set of experiments, the sum of counts were corrected for the sampling time.

The corrected sum of counts were then divided by the number of events, and the value of S_i [Counts/ (number of events. Second)] was obtained for each detector.

The ratio of the S_B/S_A are plotted in Figure 5-20 below.

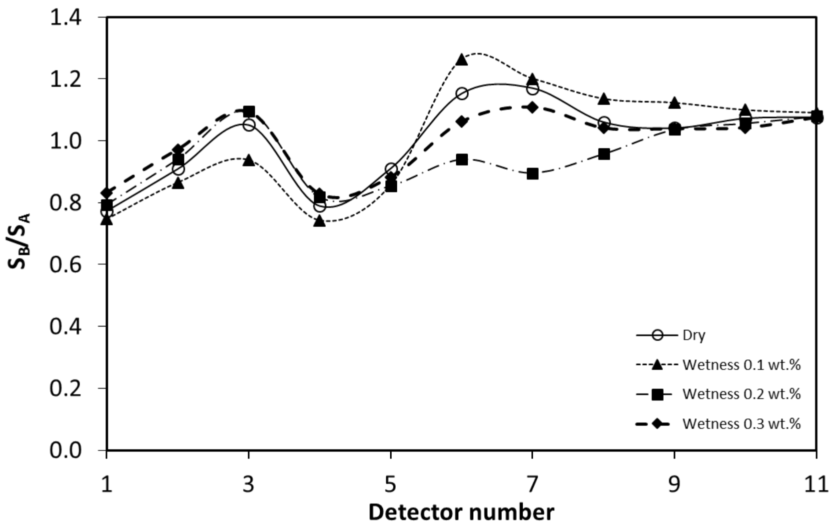

Figure 5-20. Comparison of S_B/S_A, V_g = 0.9 m/s

In the absence of any collimation effect, when we pull back the detectors, the distance is increasing thus we should register less counts. Considering that the counts registered by a detector are related to the distance from the tracer by the inverse square law, and assuming that the tracer is in three different locations most of the time: the expected S_B/S_A would be 0.37 for the tracer at the near wall, 0.6 for the tracer at the center of the column and 0.72 for the tracer at the far wall.

A significant decrease is also expected to result from the decrease of the detection volume when the detectors are pulled back (as shown in the analysis that assumed a thin plate as the collimator), because the tracer has less chance to be in the detection volume of a detector, thus spending less time in that detection volume.

However, from the graphs above, the ratio S_B/S_A is always higher than 0.7 and its average value is 0.98, i.e. much near to 1 than predicted. This suggests that the gamma rays emitted by the tracer are nearly perfectly collimated by the plate openings that we used.

Looking at the original equation we developed earlier:

$$f = p(r,z)\frac{m_{tracer}}{M_{bed}} = f_{0,0} \times \sqrt{\frac{TDH}{TDH - z}} \times \exp(-A_c z) \times \left|(1 - \frac{r}{R})\right|^n \qquad \textbf{5-25}$$

Assuming the radial independency of f from the radial position (which was proven to be true, see Chapter 2), one can write:

$$\frac{f}{f_0} = \sqrt{\frac{TDH}{TDH - z}} \times \exp(-A_c z) \qquad \textbf{5-35}$$

In the current experimental condition, it can be shown that the $\exp(-A_c z)$ term is dominating the $\sqrt{\frac{TDH}{TDH-z}}$ term:

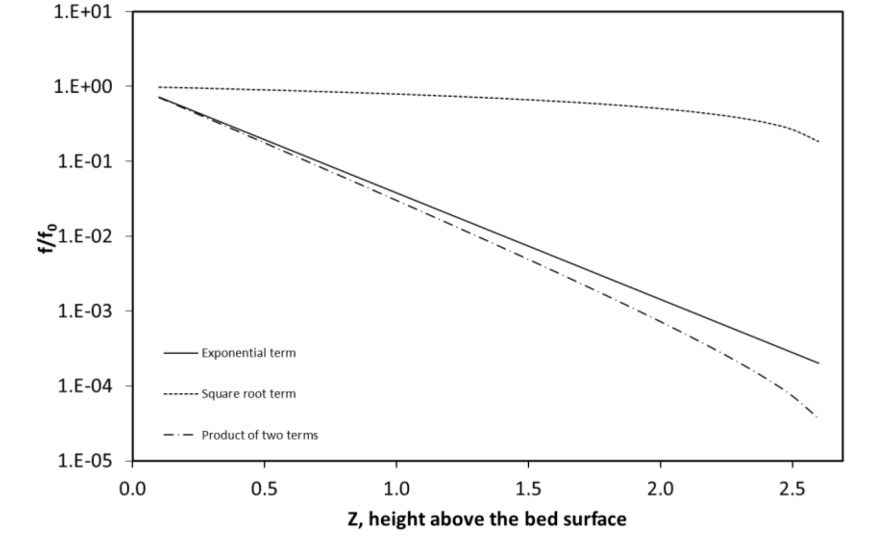

Figure 5-21. Comparison of the effect of two terms in Equation 5-35, TDH = 2.69 m and A_c = 3.275 1/m adopted from Chapter 3

In the Equation 5-35, f_0 is the probability of the tracer being present at the bed surface. Considering the first detector is monitoring the bed surface, S_1 is proportional to f_0. As a result, by normalizing the data using equation below:

$$\Psi_i = \frac{S_i}{S_1} \qquad \textbf{5-36}$$

By plotting Ψ_i versus height above the bed surface for the dry bed at V_g = 0.9 m/s:

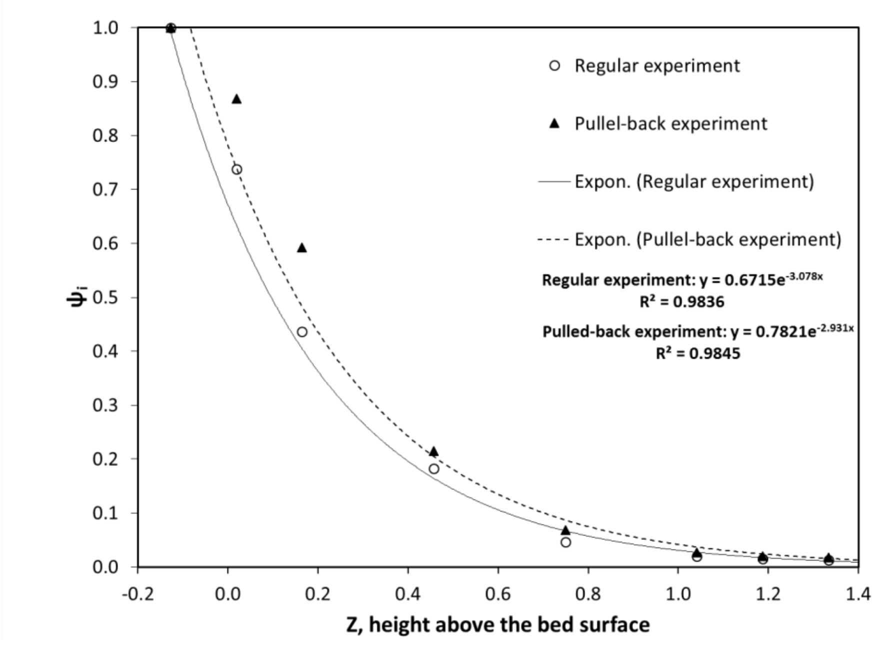

Figure 5-22. ψ_i vs. Height, Dry bed, $V_g = 0.9$ m/s

As can be seen in the Figure 5-22, the data follow an exponential pattern as expected from Equation 5-35. The same exponential pattern will be observed if one plots Ψ_i versus height above the bed surface for other bed wetnesses. This also, proves that exponential term is dominating the square root term in Equation 5-35 for the current experimental condition. Also, the variation between two sets of data (Regular and Pulled-back) is negligible: thus one set can be considered as a replicate set for the other one.

Based on the above findings, linear regression analysis of the raw data as well as data corrected for $\sqrt{\frac{TDH}{TDH-z}}$, for each experimental condition, was performed. The results are shown in the Table 5-4 through Table 5-7. It is worth noting that in these tables, the relative margin of error is the percentage of deviation possible around the point estimate at a specific confidence interval. Here, the point estimate is A_c and deviation around this estimate is calculated at a 95 percent confidence interval. The relative margin of error is calculated by dividing the absolute margin of error (“radius" or half the width of a confidence interval) by the point estimate.

Table 5-4. A_c obtained from linear regression of the logarithm of the ψ_i vs. height, V_g = 0.9 m/s, Dry bed

Type of experiment	A_c obtained with no correction for TDH, 1/m	Relative margin of error on A_c	A_c obtained by correcting for TDH = 1.4 m, 1/m	Relative margin of error on A_c	A_c obtained by correcting for TDH = 3.98 m, 1/m	Relative margin of error on A_c
Regular	3.08	12%	4.13	8%	3.23	10%
Pulled-back	2.93	12%	3.96	8%	3.08	11%
Joined* (Regular and Pulled-back)	3.01	8%	4.05	4%	3.16	7%

***The two sets of data simultaneously were used in the linear regression analysis**

Table 5-5. A_c obtained from linear regression of the logarithm of the ψ_i vs. height, V_g = 0.9 m/s, Wetness of 0.1 wt.%

Type of experiment	A_c obtained with no correction for TDH, 1/m	Relative margin of error on A_c	A_c obtained by correcting for TDH = 1.4 m, 1/m	Relative margin of error on A_c	A_c obtained by correcting for TDH = 3.98 m, 1/m	Relative margin of error on A_c
Regular	3.19	13%	4.18	7%	3.44	12%
Pulled-back	2.89	11%	3.92	7%	3.17	10%
Joined (Regular and Pulled-back)	3.01	8%	3.77	10%	3.16	8%

Table 5-6. A_c obtained from linear regression of the logarithm of the ψ_i vs. height, V_g = 0.9 m/s, Wetness of 0.2 wt.%

Type of experiment	A_c obtained with no correction for TDH, 1/m	Relative margin of error on A_c	A_c obtained by correcting for TDH = 1.4 m, 1/m	Relative margin of error on A_c	A_c obtained by correcting for TDH = 3.98 m, 1/m	Relative margin of error on A_c
Regular	3.03	12%	4.07	4%	3.18	11%
Pulled-back	2.92	14%	3.97	7%	3.07	13%
Joined (Regular and Pulled-back)	2.97	8%	4.02	4%	3.12	7%

Table 5-7. A_c obtained from linear regression of the logarithm of the ψ_i vs. height, V_g = 0.9 m/s, Wetness of 0.3 wt.%

Type of experiment	A_c obtained with no correction for TDH, 1/m	Relative margin of error on A_c	A_c obtained by correcting for TDH = 1.4 m, 1/m	Relative margin of error on A_c	A_c obtained by correcting for TDH = 3.98 m, 1/m	Relative margin of error on A_c
Regular	3.013	13%	4.07	5%	3.16	13%
Pulled-back	2.92	14%	3.97	6%	3.07	13%
Joined (Regular and Pulled-back)	2.97	8%	3.75	10%	3.12	8%

By looking at the values of values of A_c, it can be seen that there is only a slight difference between the values obtained using the two different set of experiments (Regular and pulled-back). Also, in all cases, the error is reduced when one uses the data from both sets at the same time. This is because one uses more points to obtain the value of A_c.

The values of A_c are also obtained by correcting the raw data for $\sqrt{\frac{TDH}{TDH-z}}$, using the extreme values of TDH obtained in Chapter 3. There is a slight difference between the A_c values obtained by correcting for TDH = 3.98 m and with no correction. However, this difference would be significant if one uses TDH =1.4 m. This suggests that the method works best when the detectors monitor regions of freeboard away from TDH (i.e. closer to the bed surface).

By looking at the values obtained using pseudo-isokinetic sampling probes in Chapter 3 and Chapter 4:

Table 5-8. Comparison of A_c from the radioactive measurements and from cluster analysis with pseudo-isokinetic probes for V_g = 0.9 m/s

Method	**Values at V_g = 0.9 m/s, Dry**	**Values at V_g = 0.9 m/s, 0.1 wt.% wetness**	**Values at V_g = 0.9 m/s, 0.2 wt.% wetness**	**Values at V_g = 0.9 m/s, 0.3 wt.% wetness**
A_c Average from radioactive measurements, 1/m	3.16	3.16	3.12	3.12
A_c Average from pseudo-isokinetic probes, 1/m	3.27	3.30	3.22	3.23

It can be seen that the values of A_c obtained using the two sets of experiment and when corrected with TDH = 3.98 m are very close to what is obtained by pseudo-isokinetic sampling probes, suggesting that the radioactive tracer method can reliably measures the decay coefficient (A_c) of cluster flux. This also proves the presence of clusters in the freeboard.

Also, the values of A_c obtained with no corrections for both sets of experiments, shows a close value to what is being obtained by pseudo-isokinetic sampling probes suggesting that the radioactive tracer method can be independently be employed to obtain the decay coefficient (A_c) of cluster flux.

5.7 Conclusions

The motion of ejected clusters in the freeboard could not be tracked with RPT because the clusters move too fast for the strength of radioactive source that was used.

The decrease in concentration of the clusters with height in the freeboard could be measured by using radioactive tracer technique in which the detectors are collimated. Also, this method proves that the particles are ejected as clusters to the freeboard. It was found that this method can reliably and independently measure the exponent term (A_c) of the cluster flux decay. This method becomes more accurate if the measurements are performed at distances far from TDH and close to the bed surface, unlike pseudo-isokinetic technique where it is best to perform measurements far from the bed surface. If the value of TDH is known, by correcting the raw data obtained, one can get a decent value of A_c. Considering the findings in Chapter 3 and Chapter 4 where pseudo-isokinetic sampling method was employed, these two methods cross-validate each other.

To sum up, it was found that the current radioactive tracer method only provides the decay coefficient A_c of the clusters flux decay. It could also likely provide the absolute concentration of clusters at any height and, in particular, at the bed surface. However, more investigations, analysis, and modifications are needed for this purpose.

5.8 References

Baron, T., Briens, C.L., Bergougnou, M.A., 1988. Study of the transport disengaging height. Can. J. Chem. Eng. 66, 749–760.

Baron, T., Briens, C.L., Bergougnou, M.A., 1988. Measurement of the Flux of Clusters Ejected from a Fluidized Bed. Powder Technol. 55, 115–125.

Bartholomew, R.N., Casagrande, R.M., 1957. Measuring Solids Concentration in Fluidized Systems by Gamma-Ray Absorption. Ind. Eng. Chem. 49, 428–431.

Bhusarapu, S., Al-Dahhan, M., Dudukovic, M.P., 2004. Quantification of solids flow in a gas–solid riser: single radioactive particle tracking. Chem. Eng. Sci. 59, 5381–5386. doi:10.1016/j.ces.2004.07.052

Bhusarapu, S., Cassanello, M., Al-Dahhan, M.H., Dudukovic, M.P., Trujillo, S., O'Hern, T.J., 2007. Dynamical features of the solid motion in gas–solid risers. Int. J. Multiph. Flow 33, 164–181. doi:10.1016/j.ijmultiphaseflow.2006.08.006

Darton, R.C., 1979. A Bubble Growth Theory of Fluidized Bed Reactors. Trans IChemE. 57, 134–138.

Davidson, J.F., Harrison, D., 1963. Fluidized Particles. Cambridge University Press. Cambridge.

Degaleesan, S., 1997. Fluid dynamic measurements and modeling of liquid mixing in bubble columns. PhD Thesis. Washington University, Saint Louis, Missouri, USA.

Degaleesan, S., Dudukovic, M.P., Pan, Y., 2002. Application of wavelet filtering to the radioactive particle tracking technique. Flow Meas. Instrum. 13, 31–43. doi:10.1016/S0955-5986(02)00010-9

Devanathan, N., 1991. Investigation of liquid hydrodynamics in bubble columns via a computer automated radioactive particle tracking (CARPT) Facility. Washington University, Saint Louis, Missouri, USA.

Furimsky, E., 2000. Characterization of cokes from fluid/flexi-coking of heavy feeds. Fuel Process. Technol. 67, 205–230.

Gupta, P., 2002. Churn-turbulent bubble columns: experiments and modeling. Washington University, St. Louis, Missouri, USA.

Hilligardt, K., Werther, J., 1987. Influence of Temperature and Properties of Solids on the Size and Growth of Bubbles in Gas Fluidized Beds. Chem. Eng. Techno. 10, 272–280.

Knoll, G.F., 2010. Radiation Detection and Measurement. John Wiley & Sons.

Kondukov, N., Kornilae, A., Akhromen, A., 1965. Investigation of parameters of particle motion in a fluidized bed by radioisotopic method. Int. Chem. Eng. 5, 83–86.

Konefal, A., 2011. Undesirable Radioisotopes Induced by Therapeutic Beams from Medical Linear Accelerators. Radioisot. - Appl. Bio-Medical Sci. 127–150.

Kumar, S.B., 1994. Computed tomographic measurements of void fraction and modeling of the flow in bubble columns. Florida Atlantic University.

Larachi, F., Chaouki, J., Kennedy, G., Dudukovic, M.P., 1997. Non-Invasive Monitoring of Multiphase Flows, Non-Invasive Monitoring of Multiphase Flows. Elsevier.

Large, J.F., Martinie, Y., Bergougnou, M.A., 1976. Interpretive model for entrainment in a large gas-fluidized bed. J. Powders Bulk Solids Technol.

Limtrakul, S., Chen, J., Ramachandran, P.A., Duduković, M.P., 2005. Solids motion and holdup profiles in liquid fluidized beds. Chem. Eng. Sci. 60, 1889–1900. doi:10.1016/j.ces.2004.11.026

Lin, J.S., Chen, M.M., Chao, B.T., 1985. A novel radioactive particle tracking facility for measurement of solids motion in gas fluidized beds. AIChE J. 31, 465–473.

Morooka, S., Kawazuishi, K., Kato, Y., 1980. Holdup and flow pattern of solid particles in freeboard of gas—solid fluidized bed with fine particles. Powder Technol. 26, 75–82.

Moslemian, D., Devanathan, N., Dudukovic, M.P., 1992. Radioactive particle tracking technique for investigation of phase recirculation and turbulence in multiphase systems. Rev. Sci. Instrum. 63, 4361.

Rados, N., 2003. Slurry bubble column hydrodynamics. PhD Thesis. Washington University, Saint Louis, Missouri, USA.

Rammohan, A.., Kemoun, A., Al-Dahhan, M.., Dudukovic, M.., 2001. A Lagrangian description of flows in stirred tanks via computer-automated radioactive particle tracking (CARPT). Chem. Eng. Sci. 56, 2629–2639. doi:10.1016/S0009-2509(00)00537-6

Rammohan, A.R., Kemoun, A., Al-Dahhan, M.H., Dudukovic, M.P., 2001. Characterization of Single Phase Flows in Stirred Tanks via Computer Automated Radioactive Particle Tracking (CARPT). Chem. Eng. Res. Des. 79, 831–844. doi:10.1205/02638760152721343

Roy, S., Larachi, F., Al-Dahhan, M.H., Dudukovic, M.P., 2001. Resolution and sensitivity in computer-automated radioactive particle tracking (CARPT). Intelligent Systems and Smart Manufacturing. International Society for Optics and Photonics, pp. 122–133. doi:10.1117/12.417157

Roy, S., Larachi, F., Al-Dahhan, M.H., Duduković, M.P., 2002. Optimal design of radioactive particle tracking experiments for flow mapping in opaque multiphase reactors. Appl. Radiat. Isot. 56, 485–503.

Sanchez Careaga, F.J., 2013. Hydrodynamics in Recirculating Fluidized Bed Mimicking the Stripper Section of the Fluid Coker. Electron. Thesis Diss. Repos. Western Ontario, London, ON, Canada.

Shehata, A.H., Aljohani, M.S., Arabia, S., 2007. A Review of Nuclear Non-Intrusive Visualization Methods in Industry : Computed Tomography and Particle Tracking. 4th Middle East NDT Conf. Exhib. Kingdom Bahrain.

Chapter 6

6 Conclusions and recommendations

6.1 Conclusions

- A new fluidized bed has been designed and constructed to fluidize a bed of coke particles. This bed is designed in a way to enable us to study the entrainment of solids specifically.

- Five pseudo-isokinetic sampling systems were developed and tested which collect the entrained solids at different heights. Preliminary tests show that these sampling systems work in pseudo-isokinetic condition or close to it and the results from them can be trusted.

- It was found that the solids flux increase as the probes get closer to the bed surface, but no radial dependency has been observed at any axial location in the freeboard region.

- Different correlations were used and shown that are not reliable in predicting entrainment-related parameters and thus, experimental data are in demand.

- There are few models which one can use to fit the experimental data into to get the parameters needed in the design stage. The best results however, came from the model proposed by Baron et al. 1988b which takes into account of the cluster flux.

- With only a few measurements in the freeboard of the fluidized bed, and using the cluster model, one can predict the particle flux any height as well as above the TDH which provides enough information for an engineer at the design stage.

- In the presence of liquid, the total entrainment was reduced by increasing the liquid content, particularly at heights far from the bed surface. This was due to agglomeration of fines and their adherence to the larger particles.

- In the bubbling regime, increase in the liquid content first resulted in a decrease in the flux of solids ejected to the bed surface. This was explained by presence of larger but less frequent bubbles initiated from transition to Group A and decrease in the minimum fluidization velocity. By further increasing the liquid, the flux at the bed surface increased due to formation of larger bubbles suggesting a further decrease in the minimum fluidization velocity. By further increasing the liquid content, the inter-particle forces became dominant and the powder behaved as Group C, resulting in a significant increase in the U_{mf} and causing formation of small bubbles and significant reduction in the flux of ejected solids at the bed surface.

- When the bed operates in the turbulent regime, the increase in the liquid content did not change the powder behavior and bed hydrodynamics significantly, thus no significant changes were observed in the flux of solids ejected from the bed surface or the value of TDH. This was due to the fact that changes in the U_{mf} due to the presence of slight amount of liquid was negligible comparing to the gas superficial velocity.

- The motion of ejected clusters in the freeboard could not be tracked with RPT because the clusters move too fast for the strength of radioactive that was used.

- It was found that the radioactive tracer method with collimated detectors only provides the decay coefficient A_c of the clusters flux decay. It could also likely provide the absolute concentration of clusters at any height and, in particular, at the bed surface. However, more investigations, analysis, and modifications are needed for this purpose.

6.2 Recommendations

- One should use a bank of sonic nozzles to ensure a constant gas velocity in the column. This will reduce the pressure disturbance in the bed that affects the gas flowrate in the upstream of flow. Thus, one can expect a lower standard deviation of gas velocity. In this way, the variations observed between the flux measured and the dipleg flux resulted from this will be reduced. Also, this will improve the quality of cluster flux analysis as one can more reliably predict the largest entrainable particle size.

- In our pseudo-isokinetic sampling system, we used flowmeters which had 4% of full-scale accuracy. Besides, human error was involved as one was required to set the flowrate at a specific value to adjust the suction velocity at the probe tip. As a result, the actual pseudo-isokinetic condition might not be obtained. Besides fluctuations during the experiments in the flowmeters were observed which suggest that the probes, sometimes, were deviating from pseudo-isokinetic conditions. It is best to use a set of restriction and a pressure transducer and to monitor the flowrate in each sampling line.

- It is recommended that one increases the volume of the sampling jars to allow more solids to be collected. More ability in the collection of solids lead to a higher sampling time and thus, less error in the solids flux measured. The reduction in the error can be expected to be significant in the measurement close to the bed surface. Also, this can allow the user to be consistent on the sampling time in all axial locations. However, care should be taken as the high sampling time and collecting a larger amount of solids may change the bed size distribution and consequently change the rate of solids collected over the period of sampling time. This is expected for measurements far from the bed surface where mostly the fines are present.

- Due to the large number of data generated in entrainment study experiments, handling and analyzing data manually is very time-consuming and increase the chance of inadvertent mistakes. It is highly recommended to one to develop a software/program that reads the size distribution automatically from the files generated by Particle Size Analyzer. In this way, one can create a database of size distributions, which can later be integrated with a separate database of solids fluxes. These databases, will be extremely useful and time-saving when one is performing the cluster analysis. One can also perform various and deeper analysis of data in a short period of time.

- To better understand the effect of liquid content on solids entrainment in a turbulent fluidized bed, one should increase the liquid content beyond the 0.3 wt.% which was the maximum value tested in our experiments, ensuring that changes in the U_{mf} due to the presence of liquid is not negligible comparing to the gas superficial velocity.

- Due to the availability, previous experience and works in our lab, gold was chosen as a radioactive isotope. However, due to its relatively short half-life, it prevents the experimenter to perform longer tests. Also, due to the short amount of time available to perform a few sets of experiments, the user need to prioritize experimenting and postpone analyzing the data to a later time. Thus possible flaws/issues in the system will not be detected at early stages of experiments. A radioactive candidate with a long half-life allows for multiple uses can address these issues and also, reduces costs and saves time.

- Due to material and technical limitation, we were unable to match the tracer density with the estimated density of the emulsion phase. One, should address this issue for next experiments. However, it would be interesting to investigate the entrainment of different tracer sizes and densities which can be attributed to the agglomerate sizes and densities respectively.

- As mentioned in the text, some odd behaviors observed in the radioactive tracer technique. One should find the origin of the problem and find a proper solution for it. One good solution, in our opinion, is to perform a prior calibration experiment for the collimated detectors.

- As the drag force on the tracer is negligible (comparing to weight) and considering that the tracer have the same rise and fall velocity, by performing cross-correlation on the raw data from the detectors, one can get the velocity of the tracer across the freeboard as well as its ejection velocity. The ejection velocity gives an insight of the bubble velocity and sheds light on the hydrodynamics of the fluidized bed.

Appendices

Appendix A: Position of ports in each configuration

For the center of the column, X = 0 and Y = 0 were considered.

R is the radius of the column and it is equal to 95.25 mm.

Table A-1. Position of the ports: Black configuration

Port number in configuration	Universal Port number	X(mm)	Y(mm)	r/R	Theta(degree)
1	1	77.57	0.00	0.81	0.00
2	6	0.00	-77.57	0.81	270.00
3	4	-54.85	54.85	0.81	135.00
4	3	0.00	77.57	0.81	90.00
5	2	54.85	54.85	0.81	45.00

Table A-2. Position of the ports: Green configuration

Port number in configuration	Universal Port number	X(mm)	Y(mm)	r/R	Theta(degree)
1	1	77.57	0.00	0.81	0.00
2	7	54.85	-54.85	0.81	315.00
3	5	-54.85	-54.85	0.81	225.00
4	4	-54.85	54.85	0.81	135.00
5	3	0.00	77.57	0.81	90.00

Table A-3. Position of the ports: Blue configuration

Port number in configuration	Universal Port number	X(mm)	Y(mm)	r/R	Theta(degree)
1	1	77.57	0.00	0.81	0.00
2	8	34.93	0.00	0.37	0.00
3	11	-7.95	0.00	0.08	180.00
4	10	-13.97	-39.69	0.44	250.61
5	9	-13.97	39.69	0.44	109.39

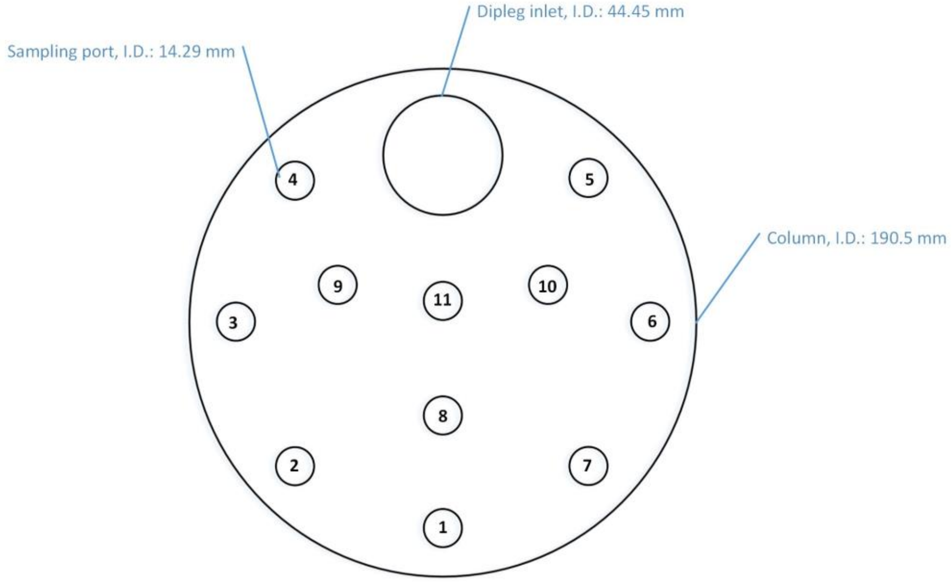

Figure A-1. Dipleg, Sampling ports and Universal Port number (Drawing to scale)

Table A-4. Universal position of the sampling ports

Universal Port number	X(mm)	Y(mm)	r/R	Theta(degree)
1	77.57	0.00	0.81	0.00
2	54.85	54.85	0.81	45.00
3	0.00	77.57	0.81	90.00
4	-54.85	54.85	0.81	135.00
5	-54.85	-54.85	0.81	225.00
6	0.00	-77.57	0.81	270.00
7	54.85	-54.85	0.81	315.00
8	34.93	0.00	0.37	0.00
9	-13.97	39.69	0.44	109.39
10	-13.97	-39.69	0.44	250.61
11	-7.95	0.00	0.08	180.00

Appendix B: Data and results for Dry bed

Table B-1. Data and results for V_g = 0.3 m/s

Average Height, m	st.dev of Average Height, m	Average measured flux, kg/(m^2.s)	St.dev of Average measured flux, kg/(m^2.s)	Average Sauter mean diameter of the sample, micron	st.dev of Average Sauter mean diameter of the sample, micron	Average cluster flux, kg/(m^2.s)	Average non-cluster flux, kg/(m^2.s)
1.386	0.007	3.57E-02	5.2E-03	59.6	1.7	6E-04	3.51E-02
1.310	0.004	3.57E-02	3.3E-03	61.1	2.1	7E-04	3.50E-02
1.234	0.008	3.62E-02	2.9E-03	62.0	1.5	1.1E-03	3.50E-02
1.158	0.006	3.73E-02	4.2E-03	62.3	0.5	1.3E-03	3.60E-02
1.082	0.007	3.80E-02	5.1E-03	63.4	1.1	1.9E-03	3.61E-02
1.006	0.008	3.84E-02	3.5E-03	65.1	0.1	2.8E-03	3.55E-02
0.930	0.007	4.03E-02	5.7E-03	67.5	0.1	4.2E-03	3.61E-02
0.854	0.007	4.19E-02	4.7E-03	69.5	1.7	5.5E-03	3.64E-02
0.778	0.005	4.42E-02	3.5E-03	73.3	0.9	8.1E-03	3.61E-02
0.702	0.007	4.97E-02	6.6E-03	78.5	0.3	1.25E-02	3.72E-02
0.626	0.005	5.43E-02	6.2E-03	83.3	1.9	1.71E-02	3.71E-02
0.550	0.009	6.42E-02	9.1E-03	90.4	1.3	2.63E-02	3.79E-02

Table B-2. Data and results for V_g = 0.6 m/s

Average Height, m	st.dev of Average Height, m	Average measured flux, kg/(m^2.s)	St.dev of Average measured flux, kg/(m^2.s)	Average Sauter mean diameter of the sample, micron	st.dev of Average Sauter mean diameter of the sample, micron	Average cluster flux, kg/(m^2.s)	Average non-cluster flux, kg/(m^2.s)
2.460	0.007	8.36E-02	9.1E-03	70.5	1.5	9E-04	8.26E-02
2.290	0.007	8.60E-02	1.27E-02	71.7	0.6	1.7E-03	8.43E-02
2.152	0.007	9.23E-02	9.8E-03	72.7	1.6	3.2E-03	8.90E-02
1.988	0.005	9.51E-02	1.29E-02	74.4	0.5	5.8E-03	8.92E-02
1.841	0.007	1.056E-01	8.5E-03	76.6	1.3	1.02E-02	9.53E-02
1.685	0.004	1.188E-01	1.41E-02	81.5	0.2	2.06E-02	9.82E-02
1.528	0.005	1.356E-01	1.70E-02	87.5	1.5	3.64E-02	9.92E-02

Table B-3. Data and results for V_g = 0.9 m/s

Average Height, m	st.dev of Average Height, m	Average measured flux, kg/(m^2.s)	St.dev of Average measured flux, kg/(m^2.s)	Average Sauter mean diameter of the sample, micron	st.dev of Average Sauter mean diameter of the sample, micron	Average cluster flux, kg/(m^2.s)	Average non-cluster flux, kg/(m^2.s)
2.455	0.004	8.447E-01	8.86E-02	85.0	0.9	1.54E-02	8.292E-01
2.29	0.007	8.750E-01	9.09E-02	86.4	0.5	2.55E-02	8.495E-01
2.144	0.005	8.978E-01	1.005E-01	87.3	0.3	4.29E-02	8.549E-01
1.989	0.005	9.322E-01	9.97E-02	88.4	1.6	6.51E-02	8.671E-01
1.849	0.006	1.0242E+00	1.048E-01	90.1	1.4	1.078E-01	9.161E-01
1.684	0.008	1.1012E+00	1.354E-01	93.3	2.1	1.858E-01	9.147E-01
1.542	0.008	1.2354E+00	1.281E-01	97.5	0.3	3.158E-01	9.197E-01

Appendix C: Data and results for Wet bed

Table C-1. Data and results for V_g = 0.3 m/s, Wetness of 0.1 wt. %

Average Height, m	st.dev of Average Height, m	Average measured flux, kg/(m^2.s)	St.dev of Average measured flux, kg/(m^2.s)	Average Sauter mean diameter of the sample, micron	st.dev of Average Sauter mean diameter of the sample, micron	Average cluster flux, kg/(m^2.s)	Average non-cluster flux, kg/(m^2.s)
1.382	0.008	2.95E-02	2.7E-03	63.3	0.2	1.4E-03	2.80E-02
1.315	0.009	3.03E-02	3.7E-03	64.6	1.7	2.0E-03	2.83E-02
1.236	0.006	3.09E-02	3.7E-03	65.2	0.3	2.3E-03	2.86E-02
1.162	0.005	3.23E-02	2.9E-03	67.8	0.3	3.5E-03	2.87E-02
1.088	0.009	3.33E-02	3.5E-03	70.2	1.4	4.7E-03	2.86E-02
1.005	0.004	3.41E-02	3.9E-03	71.5	1.9	5.4E-03	2.86E-02
0.922	0.009	3.66E-02	3.0E-03	75.1	0.6	7.6E-03	2.90E-02
0.846	0.006	3.79E-02	5.3E-03	76.5	1.7	8.5E-03	2.93E-02
0.777	0.006	4.04E-02	3.3E-03	80.2	2.1	1.11E-02	2.93E-02
0.700	0.006	4.36E-02	3.7E-03	83.7	1.6	1.40E-02	2.95E-02
0.635	0.009	4.93E-02	4.6E-03	88.8	2.1	1.93E-02	3.00E-02
0.551	0.005	5.41E-02	4.9E-03	92.5	0.8	2.38E-02	3.03E-02

Table C-2. Data and results for V_g = 0.3 m/s, Wetness of 0.2 wt. %

Average Height, m	st.dev of Average Height, m	Average measured flux, kg/(m^2.s)	St.dev of Average measured flux, kg/(m^2.s)	Average Sauter mean diameter of the sample, micron	st.dev of Average Sauter mean diameter of the sample, micron	Average cluster flux, kg/(m^2.s)	Average non-cluster flux, kg/(m^2.s)
1.386	0.008	2.88E-02	4.0E-03	70.4	0.2	4.1E-03	2.46E-02
1.312	0.005	3.13E-02	4.0E-03	75.2	0.6	6.5E-03	2.48E-02
1.240	0.007	3.21E-02	3.9E-03	76.6	1.7	7.3E-03	2.48E-02
1.151	0.006	3.46E-02	2.8E-03	80.1	1.7	9.5E-03	2.51E-02
1.072	0.004	3.54E-02	2.8E-03	81.3	1.9	1.02E-02	2.51E-02
1.003	0.006	3.85E-02	3.4E-03	85.0	0.7	1.31E-02	2.53E-02
0.935	0.006	4.20E-02	5.1E-03	89.1	0.7	1.65E-02	2.54E-02
0.848	0.007	4.74E-02	5.6E-03	93.7	0.3	2.16E-02	2.57E-02
0.785	0.006	5.25E-02	7.8E-03	97.3	1.0	2.64E-02	2.60E-02
0.698	0.005	6.12E-02	7.6E-03	102.3	0.6	3.50E-02	2.61E-02
0.621	0.009	6.85E-02	8.7E-03	105.3	1.3	4.19E-02	2.66E-02
0.549	0.004	8.23E-02	8.9E-03	109.9	1.2	5.54E-02	2.68E-02

Table C-3. Data and results for V_g = 0.3 m/s, Wetness of 0.3 wt. %

Average Height, m	st.dev of Average Height, m	Average measured flux, kg/(m^2.s)	St.dev of Average measured flux, kg/(m^2.s)	Average Sauter mean diameter of the sample, micron	st.dev of Average Sauter mean diameter of the sample, micron	Average cluster flux, kg/(m^2.s)	Average non-cluster flux, kg/(m^2.s)
1.380	0.004	1.24E-02	1.7E-03	59.8	1.5	1E-04	1.23E-02
1.309	0.004	1.24E-02	1.7E-03	59.9	2.0	1E-04	1.24E-02
1.235	0.008	1.25E-02	1.6E-03	60.2	2.0	1E-04	1.24E-02
1.159	0.007	1.26E-02	1.3E-03	60.3	1.6	1E-04	1.24E-02
1.079	0.006	1.32E-02	1.7E-03	60.8	2.0	2E-04	1.30E-02
1.011	0.005	1.36E-02	1.6E-03	61.5	0.3	3E-04	1.32E-02
0.933	0.009	1.40E-02	1.1E-03	62.3	0.8	5E-04	1.35E-02
0.859	0.006	1.38E-02	1.6E-03	63.8	1.3	7E-04	1.31E-02
0.773	0.005	1.50E-02	1.5E-03	65.4	1.0	1.1E-03	1.38E-02
0.702	0.006	1.56E-02	1.3E-03	67.4	2.0	1.6E-03	1.39E-02
0.617	0.006	1.63E-02	1.7E-03	70.8	1.1	2.4E-03	1.38E-02
0.555	0.008	1.85E-02	1.7E-03	75.8	1.6	4.0E-03	1.45E-02

Table C-4. Data and results for V_g = 0.6 m/s, Wetness of 0.1 wt. %

Average Height, m	st.dev of Average Height, m	Average measured flux, kg/(m^2.s)	St.dev of Average measured flux, kg/(m^2.s)	Average Sauter mean diameter of the sample, micron	st.dev of Average Sauter mean diameter of the sample, micron	Average cluster flux, kg/(m^2.s)	Average non-cluster flux, kg/(m^2.s)
2.451	0.007	6.67E-02	9.3E-03	71.5	1.5	1.0E-03	6.57E-02
2.296	0.007	6.88E-02	8.7E-03	72.4	1.3	2.1E-03	6.67E-02
2.154	0.007	7.29E-02	7.8E-03	73.8	2.0	3.8E-03	6.90E-02
2.000	0.008	7.83E-02	7.6E-03	75.7	1.5	6.4E-03	7.19E-02
1.832	0.008	8.36E-02	8.5E-03	79.5	0.5	1.19E-02	7.17E-02
1.693	0.006	9.87E-02	1.28E-02	85.1	1.9	2.28E-02	7.58E-02
1.546	0.009	1.173E-01	1.61E-02	92.0	0.3	3.99E-02	7.73E-02

Table C-5. Data and results for V_g = 0.6 m/s, Wetness of 0.2 wt. %

Average Height, m	st.dev of Average Height, m	Average measured flux, kg/(m^2.s)	St.dev of Average measured flux, kg/(m^2.s)	Average Sauter mean diameter of the sample, micron	st.dev of Average Sauter mean diameter of the sample, micron	Average cluster flux, kg/(m^2.s)	Average non-cluster flux, kg/(m^2.s)
2.449	0.009	6.54E-02	8.2E-03	71.5	1.0	1.1E-03	6.45E-02
2.295	0.008	6.78E-02	9.0E-03	72.2	1.7	1.8E-03	6.59E-02
2.155	0.008	6.99E-02	6.3E-03	73.8	1.5	3.7E-03	6.62E-02
1.987	0.008	7.49E-02	8.5E-03	75.7	0.5	6.2E-03	6.87E-02
1.843	0.008	8.06E-02	8.2E-03	79.4	0.5	1.14E-02	6.92E-02
1.687	0.007	9.38E-02	1.29E-02	85.6	1.9	2.23E-02	7.14E-02
1.535	0.006	1.142E-01	1.57E-02	92.1	1.4	3.91E-02	7.51E-02

Table C-6. Data and results for V_g = 0.6 m/s, Wetness of 0.3 wt. %

Average Height, m	st.dev of Average Height, m	Average measured flux, kg/(m^2.s)	St.dev of Average measured flux, kg/(m^2.s)	Average Sauter mean diameter of the sample, micron	st.dev of Average Sauter mean diameter of the sample, micron	Average cluster flux, kg/(m^2.s)	Average non-cluster flux, kg/(m^2.s)
2.458	0.005	6.17E-02	7.7E-03	71.3	1.2	7E-04	6.09E-02
2.307	0.007	6.07E-02	7.1E-03	72.0	1.2	1.5E-03	5.92E-02
2.145	0.007	6.37E-02	8.9E-03	73.3	0.5	2.8E-03	6.08E-02
1.997	0.005	6.86E-02	8.8E-03	75.6	1.6	5.5E-03	6.31E-02
1.839	0.006	7.53E-02	6.3E-03	79.2	1.8	1.03E-02	6.49E-02
1.696	0.007	8.14E-02	8.9E-03	83.2	0.4	1.63E-02	6.51E-02
1.535	0.007	1.025E-01	9.9E-03	91.6	1.9	3.42E-02	6.81E-02

Table C-7. Data and results for V_g = 0.9 m/s, Wetness of 0.1 wt. %

Average Height, m	st.dev of Average Height, m	Average measured flux, kg/(m^2.s)	St.dev of Average measured flux, kg/(m^2.s)	Average Sauter mean diameter of the sample, micron	st.dev of Average Sauter mean diameter of the sample, micron	Average cluster flux, kg/(m^2.s)	Average non-cluster flux, kg/(m^2.s)
2.449	0.008	7.653E-01	8.73E-02	85.8	0.7	1.52E-02	7.501E-01
2.298	0.008	7.757E-01	1.158E-01	86.2	1.0	2.52E-02	7.505E-01
2.150	0.005	7.848E-01	9.66E-02	87.1	0.2	4.28E-02	7.420E-01
1.988	0.009	8.255E-01	6.96E-02	88.1	1.8	6.39E-02	7.615E-01
1.837	0.007	8.807E-01	1.194E-01	90.2	1.1	1.066E-01	7.741E-01
1.694	0.006	9.451E-01	9.49E-02	92.9	1.4	1.861E-01	7.590E-01
1.530	0.005	1.0812E+00	1.510E-01	96.8	1.2	3.194E-01	7.617E-01

Table C-8. Data and results for V_g = 0.9 m/s, Wetness of 0.2 wt. %

Average Height, m	st.dev of Average Height, m	Average measured flux, kg/(m^2.s)	St.dev of Average measured flux, kg/(m^2.s)	Average Sauter mean diameter of the sample, micron	st.dev of Average Sauter mean diameter of the sample, micron	Average cluster flux, kg/(m^2.s)	Average non-cluster flux, kg/(m^2.s)
2.459	0.004	7.303E-01	8.50E-02	86.23	1.7	1.84E-02	7.119E-01
2.300	0.004	7.249E-01	9.20E-02	86.87	1.8	2.77E-02	6.971E-01
2.145	0.005	7.629E-01	1.032E-01	88.25	0.2	5.06E-02	7.122E-01
1.987	0.006	7.860E-01	8.46E-02	89.61	1.4	7.41E-02	7.118E-01
1.851	0.006	8.500E-01	1.040E-01	92.23	0.3	1.256E-01	7.243E-01
1.699	0.007	9.743E-01	7.93E-02	95.84	1.3	2.160E-01	7.582E-01
1.535	0.006	1.0900E+00	9.80E-02	99.99	0.1	3.341E-01	7.558E-01

Table C-9. Data and results for V_g = 0.9 m/s, Wetness of 0.3 wt. %

Average Height, m	st.dev of Average Height, m	Average measured flux, kg/(m^2.s)	St.dev of Average measured flux, kg/(m^2.s)	Average Sauter mean diameter of the sample, micron	st.dev of Average Sauter mean diameter of the sample, micron	Average cluster flux, kg/(m^2.s)	Average non-cluster flux, kg/(m^2.s)
2.447	0.007	6.625E-01	9.37E-02	86.3	1.7	1.76E-02	6.449E-01
2.307	0.006	6.505E-01	7.37E-02	86.9	1.8	2.56E-02	6.248E-01
2.139	0.006	6.934E-01	5.68E-02	88.5	0.2	4.91E-02	6.442E-01
2.002	0.007	7.116E-01	7.90E-02	89.7	1.4	6.89E-02	6.427E-01
1.834	0.004	7.766E-01	6.74E-02	92.5	0.3	1.188E-01	6.578E-01
1.689	0.009	9.096E-01	8.85E-02	96.2	1.3	2.088E-01	7.008E-01
1.530	0.009	1.0112E+00	1.368E-01	100.3	0.1	3.166E-01	6.945E-01

Appendix D: Detectors position in tested detector configurations

Table D-1. Configuration A

Detector	Serial	X(mm)	Y(mm)	Z(mm)
1	638	0	-140	190
2	639	120	-70	500
3	656	120	70	190
4	657	0	140	500
5	658	-120	70	190
6	659	-120	-70	500
7	660	0	-140	800
8	661	120	-70	1100
9	665	120	70	800
10	668	0	140	1100
11	669	-120	70	800
12	670	-120	-70	1100

Table D-2. Configuration B

Detector	Serial	X(mm)	Y(mm)	Z(mm)
1	638	0	-140	190
2	639	120	-70	270
3	656	120	70	360
4	657	0	140	440
5	658	-120	70	520
6	659	-120	-70	600
7	660	0	-140	690
8	661	120	-70	770
9	665	120	70	850
10	668	0	140	930
11	669	-120	70	1020
12	670	-120	-70	1100

Table D-3. Configuration E

Detector	Serial	X(mm)	Y(mm)	Z(mm)
1	638	0	-140	190
2	639	120	70	270
3	656	-120	70	360
4	657	0	-140	440
5	658	120	70	520
6	659	-120	70	600
7	660	0	-140	690
8	661	120	70	770
9	665	-120	70	850
10	668	0	-140	930
11	669	120	70	1020
12	670	-120	70	1100

Table D-4. Configuration F

Detector	Serial	X(mm)	Y(mm)	Z(mm)
1	638	0	-140	190
2	639	0	140	270
3	656	-120	70	360
4	657	120	-70	440
5	658	0	140	520
6	659	0	-140	600
7	660	120	-70	690
8	661	-120	70	770
9	665	0	-140	850
10	668	0	140	930
11	669	-120	70	1020
12	670	120	-70	1100

Appendix E: Statistical analysis of the fluxes from sampling probes in three different probes configuration (Refer to Section 2.4.4)

- **Null hypothesis (*H_0*):** The average difference between two groups is not significant and the difference is due to random chance. In our case, the average flux measured by 5 probes in one configuration is not different from the average flux measured by 5 probes in a different configuration. Also, the difference between the average flux measured probes in the three configurations is not significant from the average flux measured by dipleg (or cyclone catch).

- From the t-test, the p- value is obtained and if p-value is greater than 0.05 (or 5 percent), it can be concluded that there is no difference between the means.

Table E-1. Solid flux data, Dry bed, V_g = 0.3 m/s, Above the TDH

	Flux, kg/(m^2.s)		
	Black	**Green**	**Blue**
Probe 1	3.63E-02	3.37E-02	3.64E-02
Probe 2	3.69E-02	3.54E-02	3.47E-02
Probe 3	3.40E-02	3.73E-02	3.36E-02
Probe 4	3.64E-02	3.54E-02	3.63E-02
Probe 5	3.68E-02	3.43E-02	3.47E-02
Dipleg	3.66E-02	3.40E-02	3.68E-02

Table E-2. Results of the Two-Sample T-Test using Minitab, Dry bed, V_g = 0.3 m/s, Above the TDH

	Comparison of Black and Green	**Comparison of Black and Blue**	**Comparison of Green and Blue**	**Comparison of the average of each configuration and dipleg**
P-value	0.325	0.316	0.987	0.767
Estimate for difference between two means	0.000860	0.000875	0.000015	-0.000317

Table E-3. Solid flux data, Dry bed, V_g = 0.3 m/s, Distance from bed surface = 1 m

	Flux, kg/(m^2.s)		
	Black	**Green**	**Blue**
Probe 1	3.63E-02	3.99E-02	3.62E-02
Probe 2	3.83E-02	3.90E-02	3.94E-02
Probe 3	4.02E-02	3.91E-02	3.80E-02
Probe 4	3.82E-02	4.03E-02	3.94E-02
Probe 5	3.70E-02	3.70E-02	3.64E-02

Table E-4. Results of the Two-Sample T-Test using Minitab, Dry bed, V_g = 0.3 m/s, Distance from bed surface = 1 m

	Comparison of Black and Green	Comparison of Black and Blue	Comparison of Green and Blue
P-value	0.266	0.904	0.230
Estimate for difference between two means	-0.001060	0.000120	0.001180

Table E-5. Solid flux data, Dry bed, V_g = 0.3 m/s, Distance from bed surface = 0.7 m

	Flux, kg/(m^2.s)		
	Black	**Green**	**Blue**
Probe 1	4.87E-02	4.65E-02	4.64E-02
Probe 2	4.95E-02	4.68E-02	4.60E-02
Probe 3	5.20E-02	4.71E-02	5.31E-02
Probe 4	5.09E-02	4.70E-02	4.89E-02
Probe 5	5.18E-02	5.27E-02	4.84E-02

Table E-6. Results of the Two-Sample T-Test using Minitab, Dry bed, V_g = 0.3 m/s, Distance from bed surface = 0.7 m

	Comparison of Black and Green	Comparison of Black and Blue	Comparison of Green and Blue
P-value	0.105	0.214	0.763
Estimate for difference between two means	0.00256	0.00202	-0.00054

Table E-7. Solid flux data, Dry bed, V_g = 0.3 m/s, Distance from bed surface = 0.55 m

	Flux, kg/(m^2.s)		
	Black	**Green**	**Blue**
Probe 1	6.31E-02	6.64E-02	6.77E-02
Probe 2	5.81E-02	6.96E-02	6.24E-02
Probe 3	6.49E-02	6.76E-02	6.75E-02
Probe 4	6.65E-02	6.00E-02	5.80E-02
Probe 5	5.94E-02	6.65E-02	6.92E-02

Table E-8. Results of the Two-Sample T-Test using Minitab, Dry bed, V_g = 0.3 m/s, Distance from bed surface = 0.55 m

	Comparison of Black and Green	Comparison of Black and Blue	Comparison of Green and Blue
P-value	0.155	0.362	0.699
Estimate for difference between two means	-0.00362	-0.00256	0.00106

Table E-9. Solid flux data, Wetness = 0.1 wt. %, Vg = 0.3 m/s, Above the TDH

	Flux, kg/(m^2.s)		
	Black	**Green**	**Blue**
Probe 1	3.30E-02	3.37E-02	3.34E-02
Probe 2	3.21E-02	3.13E-02	3.10E-02
Probe 3	3.05E-02	3.21E-02	3.39E-02
Probe 4	3.21E-02	3.27E-02	3.18E-02
Probe 5	3.07E-02	3.16E-02	3.24E-02
Dipleg	3.13E-02	3.04E-02	3.06E-02

Table E-10. Results of the Two-Sample T-Test using Minitab, Wetness = 0.1 wt. %, V_g = 0.3 m/s, Above the TDH

	Comparison of Black and Green	**Comparison of Black and Blue**	**Comparison of Green and Blue**	**Comparison of the average of each configuration and dipleg**
P-value	0.377	0.284	0.755	0.034
Estimate for difference between two means	-0.000600	-0.000820	-0.000220	0.001368

Table E-11. Solid flux data, Wetness = 0.1 wt. %, V_g = 0.3 m/s, Distance from bed surface = 1 m

	Flux, kg/(m^2.s)		
	Black	**Green**	**Blue**
Probe 1	3.58E-02	3.21E-02	3.45E-02
Probe 2	3.24E-02	3.21E-02	3.35E-02
Probe 3	3.35E-02	3.28E-02	3.57E-02
Probe 4	3.44E-02	3.23E-02	3.56E-02
Probe 5	3.28E-02	3.31E-02	3.33E-02

Table E-12. Results of the Two-Sample T-Test using Minitab, Wetness = 0.1 wt. %, V_g = 0.3 m/s, Distance from bed surface = 1 m

	Comparison of Black and Green	Comparison of Black and Blue	Comparison of Green and Blue
P-value	0.112	0.380	0.213
Estimate for difference between two means	0.001300	-0.000740	-0.0002040

Table E-13. Solid flux data, Wetness = 0.1 wt. %, V_g = 0.3 m/s, Distance from bed surface = 0.7 m

	Flux, kg/(m^2.s)		
	Black	**Green**	**Blue**
Probe 1	4.45E-02	4.66E-02	4.36E-02
Probe 2	4.11E-02	4.09E-02	4.46E-02
Probe 3	4.62E-02	4.62E-02	4.12E-02
Probe 4	4.18E-02	4.10E-02	4.37E-02
Probe 5	4.69E-02	4.13E-02	4.37E-02

Table E-14. Results of the Two-Sample T-Test using Minitab, Wetness = 0.1 wt. %, V_g = 0.3 m/s, Distance from bed surface = 0.7 m

	Comparison of Black and Green	**Comparison of Black and Blue**	**Comparison of Green and Blue**
P-value	0.622	0.591	0.915
Estimate for difference between two means	0.00090	00.00074	-0.00016

Table E-15. Solid flux data, Wetness = 0.1 wt. %, V_g = 0.3 m/s, Distance from bed surface = 0.55 m

	Flux, kg/(m^2.s)		
	Black	**Green**	**Blue**
Probe 1	5.71E-02	5.65E-02	4.96E-02
Probe 2	5.64E-02	5.38E-02	5.89E-02
Probe 3	5.59E-02	5.71E-02	5.32E-02
Probe 4	5.73E-02	4.92E-02	5.48E-02
Probe 5	5.04E-02	5.13E-02	5.60E-02

Table E-16. Results of the Two-Sample T-Test using Minitab, Wetness = 0.1 wt. %, V_g = 0.3 m/s, Distance from bed surface = 0.55 m

	Comparison of Black and Green	Comparison of Black and Blue	Comparison of Green and Blue
P-value	0.383	0.660	0.682
Estimate for difference between two means	0.00184	0.00092	-0.00092

Curriculum Vitae

Name:	Saber Ayatollahi
Post-secondary Education and Degrees:	The University of Western Ontario London, Ontario, Canada 2014-2016 M.E.Sc.
	University of Tehran Tehran, Iran 2009-2014 B.Sc.
Honours and Awards:	Western Engineering Scholarship 2014-2016
Related Work Experience	Research and Teaching Assistant The University of Western Ontario 2014-2016